

Transmission Electron Microscopy on Memristive Devices

DISSERTATION

by

Julian Strobel

submitted to obtain the degree of
DOCTOR OF ENGINEERING (DR.-ING.)

at the

FACULTY OF ENGINEERING - CAU KIEL
INSTITUTE FOR MATERIAL SCIENCE

First supervisor: Prof. Dr. Lorenz KIENLE
Faculty of Engineering - CAU Kiel

Second supervisor: Prof Dr. Franz FAUPEL
Faculty of Engineering - CAU Kiel

Kiel, January 2019

Date of oral examination: 17th April 2019

Contact details: Julian STROBEL
Jahnstr. 12
24116 Kiel
just@tf.uni-kiel.de

Prof. Dr. Lorenz Kienle
Faculty of Engineering - CAU Kiel
Synthesis and Real Structure
Kaiserstraße 2
24143 Kiel
lk@tf.uni-kiel.de

Prof. Dr. Franz Faupel
Faculty of Engineering - CAU Kiel
Chair for Multicomponent Materials
Kaiserstraße 2
24143 Kiel
ff@tf.uni-kiel.de

Abstract

The aim of the research unit Memristive Devices for Neuronal Systems is to develop, manufacture and understand microelectronic devices that can change their electrical resistance repeatedly and reversibly dependent on their history of operation, commonly called memristors. In the framework of this research unit this work was conducted and encompasses the complete procedure of micro- and nanostructural analysis starting with the sample preparation for transmission electron microscopy (TEM), the methods of analysis and concludes with the results and their interpretation. Besides conceptualization, fabrication and functional probing, the analysis described in this study is essential for understanding the mode of action and validation of expected results. Out of the various concepts for memristors, the most promising ones pursued within this research unit are a combined aluminum oxide tunnel barrier and a niobium oxide Schottky barrier – in short called double barrier device – and a bimetallic nanoparticle based electrochemical metallization cell (EMC) approach. Other concepts such as the MemFlash cell – a modified p-n-p transistor - are also touched upon but are not the focus of this thesis.

The double barrier memristor was fabricated by collaborators in the research unit as a wafer-scale device with about 33.000 individual devices on a 4-inch wafer, with a single device ranging from 10 μm to 50 μm square side length. Each device is a vertical stack of electrodes and electrically active materials in between. The TEM sample preparation was therefore conducted by focused ion beam (FIB) milling. Extensive care was taken to avoid or minimize any preparation artifacts. In particular, samples were prepared both by front side as well as back side thinning as to exclude any artifacts related to the beam direction. Furthermore, the ubiquitous amorphization layer induced by FIB milling was removed by post-treatment with low energy Argon ions to improve sample quality. As the oxidation state and electronic defects in the two barriers is decisive for the functionality of these devices they were analysed by electron energy-loss spectroscopy (EELS) revealing various electronic defects in these amorphous oxides. In an attempt to push this technology to CMOS compatibility the Schottky barrier has also been fabricated from hafnium oxide, revealing similar morphology with differences in electronic structure.

Investigation of nanoparticle based devices allowed exact characterization of a modified cluster source developed within the research unit which was used for sputtering the particles which in turn enables custom-tailored size distributions, compositions and even particle gradients achieved by co-sputtering a matrix material. The determined nanoparticle parameters have also been used to accurately simulate the behaviour of these devices upon application of electric fields. The resulting particle-matrix composites have been integrated into memristive devices.

Besides all-electronic memristors other approaches utilize non-linear sensor devices – e.g. gas or pressure sensors – to combine memristors and sensors into memsensors. The devices allow a sensor to "acclimatize" to baseline stimuli but still react to

changes from this baseline input to report deviations. First concepts for these devices based on highly porous CdTe or InP microstructures have been investigated for the crystallinity and chemical impurities under different growth conditions.

The investigations led to a deeper understanding of the fabrication process and the mechanisms of memristive switching ultimately enabling improvement of device design and fabrication.

Kurzfassung

Das Ziel der Forschergruppe „Memristive Bauelemente für neuronale Systeme“ ist es, mikroelektronische Bauelemente zu entwickeln und produzieren, welche ihren elektrischen Widerstand wiederholt und reversibel - in Abhängigkeit eines vorangegangenen Stromflusses - ändern können; im Sprachgebrauch werden diese Bauelemente Memristoren genannt. Im Rahmen dieser Forschergruppe entstand diese Arbeit, welche das komplette Vorgehen der mikro- und nano-strukturellen Analyse umreißt, von der Probenpräparation für das Transmissionselektronenmikroskop (TEM) über die analytischen Methoden bis hin zu den Ergebnisse und ihrer Interpretation. Neben der konzeptionellen Entwicklung, der Herstellung und der funktionellen Untersuchung der Memristoren sind die hier beschriebenen Forschungsergebnisse essentiell, um deren Wirkweise zu verstehen und die nach der Herstellung erwarteten Ergebnisse zu validieren. Von den vielen verschiedenen Konzepten, welche es für Memristoren gibt, stechen zwei als besonders vielversprechend hervor, welche in der Forschergruppe fokussiert untersucht wurden. Zum einen handelt es sich dabei um ein sogenanntes „Doppelbarrieren“-Bauelement, welches eine Aluminiumoxid-Tunnelbarriere mit einer Nioboxid-Schottkybarriere kombiniert, zum anderen ein auf bimetallic Nanopartikeln basierte elektrochemische Metallisierungszelle. Andere Ausführungen wie die MemFlash-Zelle – ein modifizierter p-n-p Transistor – werden auch in dieser Thesis erwähnt, stehen aber nicht in deren Fokus. Der Doppelbarrierenmemristor wurde im Wafermaßstab produziert, mit etwa 33.000 individuellen Bauelementen auf einem 4-Zoll-Wafer. Ein einzelnes Bauelement hat dabei Abmessungen von 10 μm bis 50 μm im Quadrat. Die TEM-Probenpräparation erfolgte durch die fokussierte Ionenstrahl-Methode. Umfassende Maßnahmen wurden ergriffen, um jegliche Präparationsartefakte zu vermeiden oder zu minimieren. Insbesondere wurden Proben sowohl von der Vorder- als auch der Rückseite gedünnt, um Artefakte aufgrund der Ionenstrahlrichtung auszuschließen. Ferner wurde die allumfassende, durch den fokussierten Ionenstrahl induzierte, amorphe Schicht durch niederenergetische Argonionen entfernt, um die Probenqualität zu maximieren. Da der Oxidationszustand und elektronische Defekte in den beiden Barrieren als entscheidend für die Funktionalität dieser Bauelemente gilt, wurden sie durch Elektronenenergieverlustspektroskopie untersucht, welche verschiedene elektronische

Defekte in diesen amorphen Oxiden offenlegte. Im Versuch, diese Technologie kompatibel zu CMOS-Prozessen zu machen, wurde das Nioboxid auch durch Hafniumoxid ersetzt. Diese Proben besaßen eine vergleichbare Morphologie, aber eine im Detail veränderte elektronische Struktur.

Untersuchungen der nanopartikulären Elemente erlaubte es die modifizierte Clusterquelle, welche für das Sputtern ebendieser Partikel verwendet wurde, exakt zu charakterisieren. Dies wiederum ermöglichte es, maßgeschneiderte Größenverteilungen, Zusammensetzungen und Partikelgradienten herzustellen, wobei letztere durch gleichzeitige Ko-Kathodenerstäubung eines Matrixmaterials erreicht wurden. Die so bestimmten Parameter erlaubten es ebenfalls das Verhalten dieser Bauelemente bei Anlegen eines elektrischen Feldes genau zu simulieren und deren Verhalten so vorherzusagen. Die resultierenden Partikel-Matrix-Komposite wurden anschließend in einzelne Bauelementen integriert.

Neben den rein elektrischen Memristoren gibt es auch Ansätze, welche Sensoren und Memristoren miteinander zu verheiraten versuchen. Hierzu zählen zum Beispiel Gas- und Drucksensoren, welche sich an ein Grundniveau „gewöhnen“ können, und trotzdem auf Veränderungen von diesem Niveau anspringen. Erste Konzepte für diese Bauelemente bestehen aus hochporösen CdTe- oder InP-Mikrostrukturen und wurden auf ihre Kristallinität und Zusammensetzung unter verschiedenen Herstellungsbedingungen untersucht.

Die Ergebnisse führten insgesamt zu einem tieferen Verständnis der Herstellungsprozesse und der zugrundeliegenden memristiven Schaltmechanismen. Ultimativ ebnet dies den Weg, sowohl Design als auch Herstellung der Bauelemente zu verbessern.

Danksagung

Am entstehen dieser Arbeit haben unzählige Menschen kleinen oder großen Anteil. Zu allererst sei hier natürlich mein Betreuer Prof. Lorenz Kienle genannt, ohne dessen Vertrauen in mich ich gar nicht erst die Möglichkeit gehabt hätte, diese Arbeit zu verfassen. Ohne seine Erfahrung, Anleitung und Unterstützung ständen hier nur leere Seiten. In kaum geringeren Maße gilt dies für Dr. Ulrich Schürmann, welcher stets ein offenes Ohr für Fragen hatte und genauso oft auch die richtige Antwort parat hatte. Natürlich gilt mein Dank auch allen Kollegen, welche mich im Laufe der Promotion begleitet haben: Viktor, Burak, Kiran, Andriy, Mao, Gero, Torben, Marius und Hendrik.

Ohne das Engagement von Prof. Hermann Kohlstedt gäbe es keine Forschergruppe 2093, und ohne Forschergruppe hätte ich nichts erforschen können. Danke Hermann, Thomas, Mirko, Finn, Henning, Maik, Martin, Sven, Nick, Karl-Heinz und noch vielen mehr! Ole war mein erster Masterand mit durchschlagendem Erfolg. Danke dafür und weiter so! Ohne Katrin und Beate wäre ich wahrscheinlich mehr als einmal an der Bürokratie gescheitert, danke für euren Durchblick.

Niklas begleitet mich nicht erst seit dem Doktorat und nach so vielen gemeinsamen Protokollen, Meetings, Konferenzen und Urlaub kann ich nur Danke sagen. Dass ich überhaupt an einer Promotion arbeiten konnte, haben auch meine Kommilitonen zu verantworten: Alex, Cai, Felix, Anneke, Vincent, Lia, Anne, Justin, Hanna, Christian. Danke für die tolle Zeit und den Spaß, den wir hatten! Genauso kann ich mich natürlich nur bei einigen Professoren bedanken, die zum einen großartige Vorlesungen kreiert haben, und mit denen ich später gemeinsam forschen durfte. Vielen Dank Prof. Föll, Prof. Quandt, Franz, Rainer und alle anderen!

Danke, Sören, für die Mittagspausen und den gelegentlichen Gruß aus der praktischen Welt. Danke, Christin, für die Proben und die gemeinsame Zeit im Reinraum und den ein oder anderen derben Spruch! Danke an alle, die dafür sorgten, dass es stets Spaß gemacht hat, zur Arbeit zu kommen: Jörg, Fabian, Florian, Leo, Matze, Iris, Yogendra, Jürgen und viele andere.

Für die konstante Unterstützung möchte ich mich natürlich auch bei meiner Familie, meinen Freunden und bei Janine bedanken. Ohne euch wäre ich nicht da, wo ich jetzt stehe. Danke.

Contents

Abstract	iii
Acknowledgements	vii
List of Figures	xii
1 Introduction	1
2 Types of Memristors	7
2.1 Valence change memory (VCM) cells	7
2.1.1 Double barrier memristor	8
2.2 Electrochemical metallization (ECM) memory	9
2.2.1 Nanoparticle gradient based memristor	9
2.3 Memensors	10
2.4 Other memristor concepts	11
3 Methods	13
3.1 Sample preparation	13
3.2 Elemental quantification, EELS and ELNES fingerprinting	14
3.3 Defects in EEL spectra	16
3.4 Spectroscopic selection rules	16
3.5 Tomography and tomographic reconstructions	17
3.6 Instrumentation	19
3.7 Conventions within this study	20
4 Investigations on Double Barrier Memristors	21
4.1 Preparation	21
4.2 First generation DBM	24
4.2.1 Preliminary analysis	25
4.2.2 In depth spectroscopic analysis of DBM	28
4.3 Second generation DBM	38
4.4 Comparative analysis	48
5 Investigations of Nanoparticulate Memristor Prototypes	57
5.1 Monometallic (Ag, Au) particles on carbon films	58
5.2 Silver particles on and in a Si matrix	60
5.3 Bimetallic AgX particles (X = Au, Pt)	63

6 Investigations on Memsensors	71
6.1 InP-Aerographite strain sensor	71
6.1.1 InP deposition on tetrapodal ZnO	71
6.1.2 InP deposition on carbon nanotube frameworks	74
6.1.3 InP deposition on Aerographite	75
6.1.4 InP deposition of Aerographite decorated with Au nanoparticles	78
6.2 CdS-aerogel pressure sensor and CdS-Aerographite gas sensor	83
6.3 CdTe-Aerographite gas sensor	88
7 Conclusion and Outlook	93
A Publications	97
Bibliography	99
Declaration of Authorship	107

List of Figures

1.1	Schematic representation of a neural network.	2
1.2	Schematic representation of a crossbar array.	3
1.3	Exemplary I-V curve of a memristor.	5
2.1	General design of the double barrier memristor.	8
3.1	Fluorescence yield as a function of atomic number.	15
3.2	Geometric sketch of goniometer and sample holder.	18
4.1	Comparison of the identical sample prepared by FIB and PIPS.	22
4.2	Comparison of DBMs prepared by front and back side thinning.	23
4.3	Schematic of the expected layer sequence in first generation DBMs.	24
4.4	HR micrograph of the first generation DBM.	25
4.5	EFTEM analysis of the DBM and correlation with HRTEM and STEM.	26
4.6	Distribution of chemical elements across the DBM.	26
4.7	Lower magnification STEM-HAADF image of the DBM.	27
4.8	Spatial elemental distribution of Nb-1-sw-HRS.	29
4.9	Spatial elemental distribution of Nb-1-sw-LRS.	30
4.10	Spatial elemental distribution of Nb-1b-sw-LRS.	31
4.11	Nb-M ₄₅ ELNES of the first generation DBM	33
4.12	O-K ELNES from the SB of the first generation DBMs.	34
4.13	O-K spectrum of AlO _x of Nb-1-sw-LRS.	36
4.14	High resolution micrographs of second generation DBMs.	39
4.15	Spatial elemental distribution of Nb-2-sw-LRS.	40
4.16	Intensity distribution of elements across the layers of Nb-2-sw-LRS.	41
4.17	Spatial elemental distribution of Nb-2-no.	42
4.18	Lateral distribution of the O-K pre-peak in Nb-2-no.	42
4.19	Spatial elemental distribution of Hf-2-sw-LRS with delamination.	43
4.20	Spatial elemental distribution of Hf-2-sw-LRS with no delamination.	43
4.21	Spatial elemental distribution of Hf-2-no.	44
4.22	Spatial elemental distribution of Nb-2-no-anodic.	44
4.23	Spatially resolved energy shift of the O-K edge.	45
4.24	Spatial elemental distribution of Nb-2-no-thermal.	46
4.25	O-K edge from the AlO _x layer of second generation DBMs.	47
4.26	O-K edge with strong pre-peak from the AlO _x layer of second generation DBMs.	48

4.27	Al–L ₂₃ edge from the AlO _x layer of second generation DBMs.	49
4.28	O-K edge from the NbO _y layer of second generation DBMs.	50
4.29	Exposure time series investigation on the O-K edge of AlO _x	51
4.30	Comparison of the spatial elemental distribution between devices.	52
4.31	Comparison of oxide layer thicknesses in DBM devices.	53
4.32	Analysis of the Al–L ₂₃ between second generation DBMs.	54
4.33	O-K spectra with a strong pre-peak and hydroxide references.	56
5.1	TEM investigations of monometallic particles on a carbon film.	59
5.2	Influence of the sputter time on particles size and density	61
5.3	Azimuthal average of a diffraction pattern intensity of Ag particles in Si matrix.	62
5.4	Particle size distribution with respect to sputtering pressure of the GAS.	64
5.5	Composition of bimetallic particles produced by the GAS	66
5.6	Overview image of the area analyzed by tomography.	66
5.7	Tomographic reconstruction of particles embedded in a Si matrix.	67
5.8	Particle analysis of AgPt samples.	68
6.1	I-V curve and electrical response to applied strain of an InP hybrid material.	72
6.2	TEM analysis of InPO ₄ needle.	73
6.3	TEM analysis of Zn ₃ (PO ₄) ₂ needle.	74
6.4	TEM analysis of InP on CNTTs.	75
6.5	Electron microscopy analysis of InP-AG compounds.	76
6.6	TEM analysis of InP microwires with lenticular defects.	77
6.7	TEM analysis of InP microstructures.	79
6.8	STEM imaging of In ₂ O ₃ particles with Au cores on Aerographite.	80
6.9	SAED pattern of In ₂ O ₃ particles with Au cores on Aerographite.	80
6.10	HRTEM micrograph of an In ₂ O ₃ particle with Au core.	81
6.11	TEM investigation on In ₂ O ₃ nanowires on Aerographite.	82
6.12	Diffraction pattern of the aerogel support	84
6.13	SEM investigations of the CdS-aerogel pressure sensor.	84
6.14	TEM investigations of the CdS-aerogel pressure sensor.	85
6.15	Overview image and SAED pattern of CdS on Aerographite.	86
6.16	Edge of CdS covered Aerographite and EDX maps.	87
6.17	Sensor properties of CdS-aerogel compound.	88
6.18	Initial attempts of CdTe deposition.	89
6.19	CdTe-Aerographite <i>micro-cactus</i>	89
6.20	Various CdTe structures on Aerographite.	90
6.21	SEM and TEM investigations of CdTe on Aerographite.	91

List of Abbreviations

ADF	Annular Dark Field
BE	Bottom Electrode
CNT(T)	Carbon Nano Tube (Tubes)
DBM	Double Barrier Memristor
CMOS	Complementary Metal Oxide Semiconductor
EDXS	Energy Dispersive X-ray Spectroscopy
EELS	Electron Energy-Loss Spectroscopy
EEPROM	Electrically Erasable and Programmable Read Only Memory
EFTEM	Energy Filtered Transmission Electron Microscopy
ELNES	Energy-Loss Near Edge Structure
EMC	Electrochemical Metallization Cell
FFT	Fast Fourier Transform
FIB	Focussed Ion Beam
FWHM	Full Width at Half Maximum
GAS	Gas Aggregation Source
HAADF	High Angle Annular Dark Field
HRS	High Resistance State
HR/HRTEM	High Resolution (TEM)
HVPE	Hydride Vapor Phase Epitaxy
ITO	Indium Tin Oxide
LDOS	Local Density Of States
LRS	Low Resistance State
PCM	Phase Change Memory
PIPS	Precision Ion Polishing System
PVD	Physical Vapor Deposition
SAED	Selected Area Electron Diffraction
SB	Schottky Barrier
SEM	Scanning Electron Microscopy/Microscope
STEM	Scanning Transmission Electron Microscopy/Microscope
TCM	Thermo Chemical Memory
TEM	Transmission Electron Microscopy/Microscope
XPS	X-ray Photoelectron Spectroscopy
ZA	Zone Axis

Chapter 1

Introduction

Recently, the requirement for signal processing and computing has become increasingly driven by pattern recognition instead of the classical arithmetic and logic operations performed by past processors. Pattern recognition – oftentimes based on unsupervised learning of neural networks – has profoundly different demands than arithmetic operations.[1]–[4] A neural network is a layered mathematical structure, Figure 1.1 shows a representation of how such a network could look like.[5]–[7] The first layer of neurons represents some input, e.g. if the aim of the network is recognizing a certain image such as a handwritten number, the input neurons would contain the brightness values of the individual pixels of that handwritten number. The last layer is the output so in this case a list of the numbers zero to nine representing the number that the network recognized in the analyzed image. In between the two there are multiple hidden layers that “convert” the input into the output and each of them represents a degree of abstraction. Figuratively speaking, each layer could for example try to recognize certain parts of the number, e.g. a line or an arc. Each neuron is connected to each neuron in the adjacent layers by a connection of a certain weight. For example a neuron representing a circle in the upper part of the image would be strongly connected to the output neurons of “8” and “9” but only weakly connected to others. The activation strength of the output neurons is dependent on the activation of the previous neurons and the weight of the connection in between. The same in turn holds for each of the previous neurons, which is dependent on the neurons in layer above, and so on, until the first layer is reached.

While this only scratches the surface of neural networks it does showcase that even simple neural networks with mundane tasks like recognizing a pixel pattern representing a hand written number require an enormous amount of computing power. Due to the all-to-all connection of neurons between adjacent layers, an exemplary neural network with an input of 28 by 28 pixels, with five hidden layers (50-100-500-1000-10 neurons each) and an output of just ten neurons has over 600.000 weights and activations to store; This network reaches one of the lowest error rates when identifying the MNIST numbers.[8] While this can be accomplished with regular arithmetic-optimized computers, it would be vastly more efficient if such a network would be implemented into hardware. Instead of a single processor attempting to

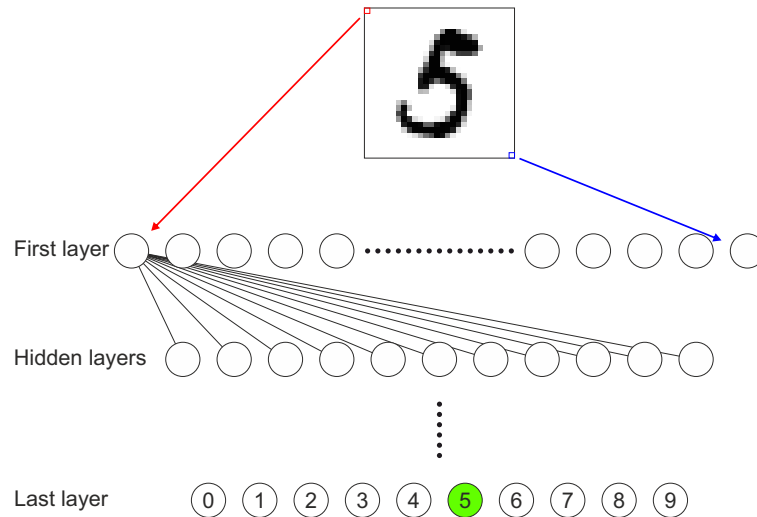


FIGURE 1.1: Schematic representation of a neural network. Each pixel of the input image at the top corresponds to exactly one input neuron in the first layer. The hidden layers in between connect the first to the last layer typically in an all-to-all fashion in between adjacent layers. Each neuron in each layer is assigned a certain value. While the neurons' values in the first layer correspond to the intensity of the pixel in the input image, the value of the neuron in the last layer represents the likelihood of the input matching the given number of the respective neuron. Input image is taken from the MNIST database. [8]

calculate each weight and activation sequentially during the learning phase the entire network could be trained in parallel. The same holds for the implementation and application, where a hardwired neural network without the need for centralized computing would be able to solve this task faster.[9]

In essence, a cross-bar array as depicted in Figure 1.2 is the physical representation of such a neural network. Every input on the bitline is connected to every output of the wordline. At every crossing a memristor can hold value thus realizing the connection strength on bitline and wordline much like the weights in the neural network connect input and output neurons.

The biological paradigm, the human brain, yields even more inspiration. Not only does it make use of massive parallelization, it also has an astonishingly low power consumption of merely around 20 W[10] while having about 10^{11} neurons[11] and 10^{15} synapses,[12] the latter being the connections between neurons in the brain, therefore being represented by the weights in between neurons in the neural network or the connections between top and bottom electrode in a crossbar array. Furthermore, the comparison illustrates the need for non-binary based computing, as the weights and activations in the neural network should certainly lie in a continuous range to express a likelihood of matching instead of just being zero and one. Sticking to the above example, this is necessary as every handwritten "5" is slightly different. On top of that, neurons and synapses in the human brain are able to store information for years and decades, have the ability to learn new things and also forget. The demand for hardware implementation of a neural network is therefore

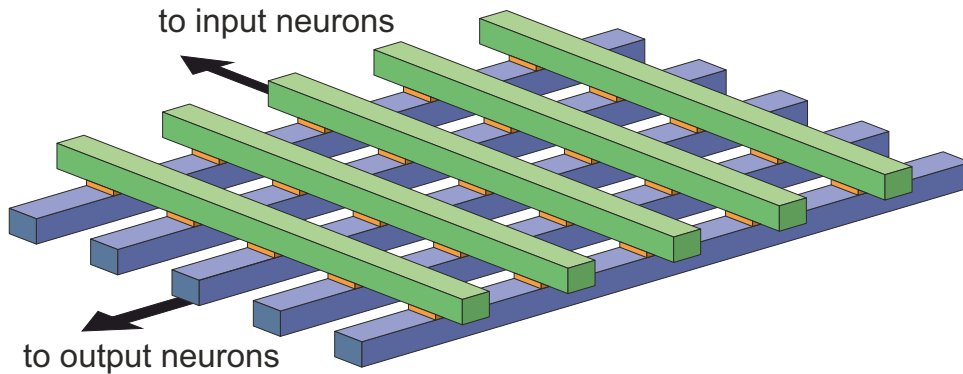


FIGURE 1.2: Schematic representation of a crossbar array. Green bars represent the top electrode of the sandwiched orange device, blue bars represent the bottom electrode. Each crossing of the two electrode harbors a two-terminal device, i.e. a connection between the input and output analogous to the weights of the connections between neurons in one layer of a neural network. Also, just as in neural networks, crossbar arrays feature an all-to-all connection between input and output.

manifold. The prototypical element to represent both neurons as well as the weights in between shall

1. be able to store a non-binary value,
2. change it in a defined range,
3. be stable for extended time periods,
4. be erasable and rewritable for several cycles and
5. have low energy consumption,
6. suitable for parallelized computation,

to name just a few. While the first five demands are straight forward the latter seems meaningless. However, it implies that the ubiquitous von Neumann architecture[13] has to be foregone to establish an architecture embracing parallel computing.[14], [15] Ideally, this device builds upon technology being readily available, i.e. silicon based wafer-technology. Another demand, at least when considering mass-market applicability, hence is CMOS compatibility meaning that there is certain limitation for the materials and processes – particularly a limitation of high temperature – used during fabrication. Astonishingly, the listed demands are met by memristors[16], a circuit element with a variable electrical resistance. Originally, the memristor was postulated by Chua in 1971 [17] as the fourth passive circuit element next to resistors, capacitors and inductors, though this definition has since been updated. Other keywords describing the same or related phenomenon are memristive device or resistive switching device, all essentially referring to a circuit element with a highly non-linear, history dependent I-V characteristic and at least two distinct resistance states. Occasionally, the term negative differential resistance can also apply to these types of devices but generally refers to volatile devices while memristors are by definition non-volatile.

Many categories aiming to differentiate various types of memristors have been established in literature. Among these categories are the switching characteristic (analog, binary, multilevel), the symmetry of electrical switching (unipolar or bipolar) or - most common in literature - the fundamental mechanism of switching, as presented in the following chapter.[16] Analog, binary and multilevel switching refer to the number of resistance states the memristor can take. A typical example of binary switching is found in memristors that rely on the formation and dissolution of conducting filaments. A memristor with a fully formed filament corresponds to a low resistance state, if no filament is formed the memristor is in the high resistance state. Analog or multilevel devices on the other hand might rely on continuous processes such as diffusion or drift of ions or multiple subsequent phase transitions. Devices switching point-symmetrically at positive and negative voltages alike are called bipolar, as they function with both polarities. Even though they are point-symmetric in their electrical characteristic, their design is often asymmetric as they might exhibit different metal electrodes. Unipolar memristors on the other hand generally operate at different magnitudes but same polarity of applied voltage.

As the previous (shallow) explanations demonstrate, the different categories are often times overlapping and closely related. Filamentary memristors are generally bipolar and binary, devices relying on the migration of oxygen ions on the other hand - and thus on a valence change - generally exhibit analog and bipolar switching. Occasionally, the very same device might exhibit bipolar, analog switching at low voltages and unipolar, binary switching at higher voltages [18]. As such, the categories of defining memristors are somewhat arbitrary and can only give a broad sense of orientation in this complex field.

In the context of this thesis a memristor shall be very broadly defined as a two-terminal circuit element, with a hysteretic I-V curve. (cf. Figure 1.3) Even though this definition differs significantly from Chua's original definition it simplifies communication of ideas and actually represents the etymology of the word memristor – a portmanteau of memory and resistor – quite well as it does represent a device which can memorize its resistance.

Accordingly, the aim of the research unit FOR2093 in whose framework this thesis was created was to develop and fabricate memristors and apply them to emulate processes in the human brain, specifically the trisynaptic circuit in the hippocampus. Imitation of this particular part of the brain was set as the long term goal, as it is one of the most studied and therefore one of the most well understood areas of the human brain. The presented work was part of the subproject "Nanostructure of materials for memristive switching". To that effect, devices produced in other subprojects have been analyzed by various microscopy techniques to unveil the nanoscopic makeup of memristors conceived in other subprojects. In particular, a focus on nanoscale spectroscopic methods was set, which allowed determination of oxidation states and elemental distribution in the produced devices. These two

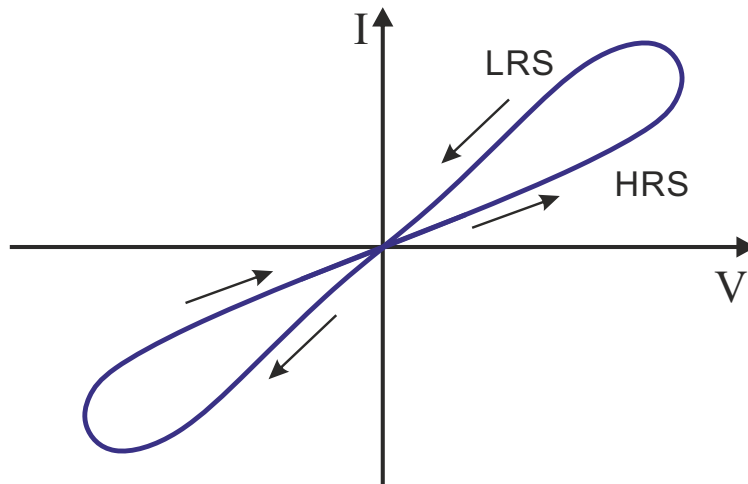


FIGURE 1.3: Exemplary I-V curve of a memristor. Low and high resistance states (LRS and HRS) are indicated as well as its direction. Important features are the pinched characteristic, the zero transition and the existence of at least two distinct resistance states. The presented I-V curve is bipolar and analog.

parameters are authoritative for the function of the produced devices. Other factors, such as crystallinity, determination of phases or orientation of these are only marginally touched upon. Before the actual investigations, sample preparation presented a huge challenge and was extensively put to the test. Further work in the research unit focused on the electrical characterization, modelling memristive learning, designing neuronal circuits, as well as simulating memristive devices and systems.

The different types of memristors, with a focus on the ones that were produced within the research unit are discussed in chapter 2. Select applied analytical techniques are described in chapter 3. The chapters 4 to 6 display the results of various microscopic investigations on different memristors. Finally, the conclusion and outlook in chapter 7 complete this thesis.

Chapter 2

Types of Memristors

After Chua's first actual of the memristor in 1971, Strukov *et al.* presented the first realization in 2008 in the form of a nanoscale device utilizing ionic transport.[19] Since then multiple different ideas for memristors have been conceptualized and accomplished as also demonstrated through the various different definitions of memristors discussed above. The most common types of memristors shall be introduced to give a context for the devices analyzed within this work.

All types of memristors discussed in this work are two-terminal devices, implying that each consists of two metal electrodes in between which the electrical resistance change occurs when a voltage is applied. Also common between memristors is the difference between a read and a write voltage. While the read voltage and its corresponding current does not alter the resistance state of the memristor, the write voltage triggers some form of state change in the memristor.

2.1 Valence change memory (VCM) cells

The general idea and name sake of VCM cells is that the cation sublattice of transition metal oxides locally changes their valence by movement of charged defects, such as oxygen ions or vacancies. Different oxides of the same transition metal exhibit different electrical conductivities thus providing for the resistance change. Accordingly, VCM cells essentially exploit a conductor-insulator transition to facilitate the resistance change. The valence change may occur locally in the form of filaments or homogeneously in between the electrodes. The latter is generally favorable over filamentary switching because of its non-binary character. Unlike homogeneous bulk switching, filamentary switching generally resembles a binary on - a filaments connects the two electrodes - or off - no complete filamentary connection - mode. An example which gathered much attention is an amorphous 50 to 90 nm thick GaO_x layer in between Pt and ITO electrodes presented by Aoki et al in 2014.[20] They showed that it is possible to change the gradient of oxygen content of this oxide by application of an electric field reversibly between two resistance states. Through spectroscopic means they found that the Ga cation exists in oxidation states of 3+ and 1+ and its ratio changes such that the average Ga valence varies from +2 to +2.7 corresponding to the low and high resistance state, respectively.

2.1.1 Double barrier memristor

A subset of VCM cells is the double barrier memristor conceived during preliminary research for the research unit FOR2093. It is an analog and unipolar device exploiting the combination of a Schottky barrier and a tunnel barrier in between two metal electrodes. The resistance change is supposed to occur not through a change in conductivity of the oxides making up the barriers, but instead changing the barrier height of the Schottky barrier. The thermionic current j_S over the barrier is dependent on the barrier height ΔE_F as well as the applied voltage U_{ex} . [21]

$$j_S(\Delta E_F, U_{ex}) = j_0 \cdot \exp - \frac{\Delta E_F - eU_{ex}}{kT} \quad (2.1)$$

Thus, changing the barrier height by modifying the Fermi energies on either side will affect the current flow therefore modifying the electrical resistance of the memristor. As both Schottky barriers as well as tunnel barriers need to be thin to allow for electrons jumping over or tunnelling through them respectively, these devices are only a few nanometers thick in between the electrodes.

The generalized design and layout of a finished wafer of DBMs is shown in Figure 2.1 next to an exemplary I-V curve. The design of the DBM originally emanates from superconducting Josephson tunnel junctions which have been expanded by an additional Schottky barrier. Naturally, these barriers are extremely thin, such that state-of-the-art transmission electron microscopy is the only reliable analytical method able resolve these layers both spatially as well as allow for nanoscopic elemental and electronic investigations. In the I-V curve in Figure 2.1 c) the different resistance states are visible through the hysteretic shape of the graph.

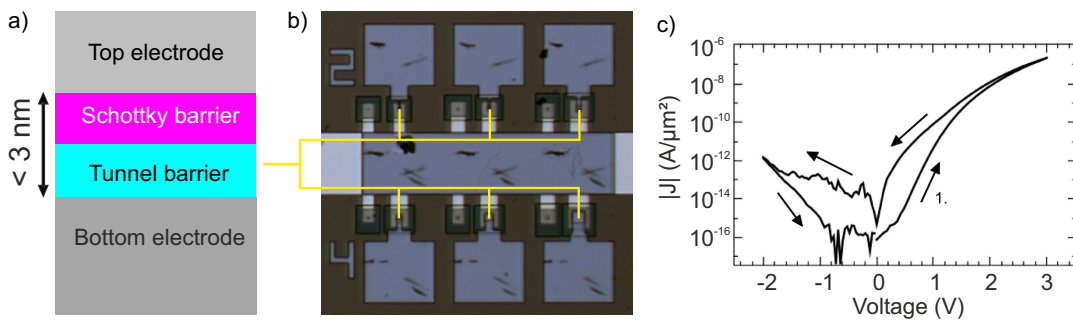


FIGURE 2.1: General design of the double barrier memristor. a) layer sequence of the DBM. The relevant Schottky and tunnel barrier are expected to be below 3 nm thick. The electrodes do not partake in the memristive switching. b) Top view of a finished wafer of memristors. Each position marked by the yellow line indicates one DBM. The large greyish rectangles are the external contact pads, black lines are scratch marks from needle contacts used for electrical characterization. Side length of the shown micrograph is about 1 mm. The dimensions of the six DBMs in the image range from 5 to 35 μm side length. c) Exemplary I-V curve of the DBM as presented by Hansen et al. [22]

2.2 Electrochemical metallization (ECM) memory

In these types of memristors metal cations originating from one of the electrodes (“active electrode”) migrate through a solid electrolyte sandwiched in between the two metal electrodes and form conducting paths called filaments. The mechanism of resistance change is the formation and dissolution of these filaments. During the formation of the filament metal ions drift towards the inert cathode where they become electrically neutral and *crystallize* to form the filament. As the distance between a growing filament - now electrically part of the cathode - and the anode becomes smaller, the field strength increases and thus a) active metal ions preferentially migrate to already partially formed filaments and b) the current density increases because of the enhanced field strength over the solid electrolyte in proximity of the filament. Eventually the filament reaches the anode. At this point the device is in its low resistance state. Also, typically no additional filaments grow because the entire voltage drops over the fully formed filament and the local field strength in the rest of the solid electrolyte film is small. Upon reversal of the voltage the filament dissolves again through the antithetic process until the device is in its high resistance state again.

Active electrodes are typically made from metals that easily ionize in electrical fields such as Ag, Cu or Ni. The opposite electrode is made from inert metals like Au or Pt. An extensive rundown of ECM cells is given in a review by Valov *et al.*[23] Unlike the demands for the ideal memristor as formulated above state, this resistance change has generally more of a binary character, because either there is a fully formed conducting filament from one electrode to the other or there is not, i.e. there are exactly two resistance states. Another typical drawback of these devices is the electroforming step, an initialization which requires a comparatively large amount of power during which the filaments are incipiently formed. The exact details of this electroforming step are not fully disclosed yet but it might be linked to forming channels in the solid electrolyte which generates large amounts of mechanical stress.[23] The typical thickness of the solid electrolyte layer between the two electrodes ranges from ten to hundreds of nanometers.

2.2.1 Nanoparticle gradient based memristor

Related to ECM memories while trying to avoid their drawbacks are nanoparticle based memristor loosely based on a concept first presented by Jo *et al.*[24] These devices utilize a particle gradient of non-inert metal, such as silver, nanoparticles (NPs) in a matrix which allows migration of ions upon application of an electrical bias. Depending on the particle gradient the device is supposed to exhibit an electrical resistance adjustable by a previously applied write voltage during which the gradient changes. In essence, the device represents two (or several) serial resistances of varying strength, where Ag-rich regions exhibit a low resistivity and Ag-depleted

regions exhibit a high resistivity. Investigations in the subproject “Vertical and horizontal memristive nanocomposites with filament formation” quickly showed that this concept would not work as intended as clusters or metal cations would eventually reach the inert metal cathode where they would not be subjected to any driving force any more effectively immobilizing them. To circumvent this problem, bimetallic NPs from one inert and one non-inert metal could prove promising in which the inert metal – e.g. gold – would stay stationary in an electrical field, while the non-inert metal can migrate. Not in the form of entire clusters, though, but instead in form of single ions. The application of bimetallic particles prevents the agglomeration of the non-inert metal - after which no resistance change is possible anymore - because the inert metal particles are supposed to act as a reservoir for the metal cations.

2.3 Memensors

Related to memristors is the class of memensors which act similar to memristor but do not necessarily change their electrical resistance depending on their history of current flow but instead dependent on their history of exposure to an external stimulus. For example, a gas sensor aiming to detect a certain gas species might adapt to a prolonged baseline exposure to that gas species and still react strongly to minute changes from that baseline concentration in the environment. The great benefit of such sensors is detecting sudden changes in the environment. The role model for such a memensors is again biological, namely the human nose. It can adapt to even high concentrations of gas species to be detected, but is still able to reliably detect small changes in the environment without being overwhelmed by a strong baseline concentration of the gas to be detected. Similar to sensors with a classical linear response, the memensors analyzed in the research unit are based on highly porous networks of semiconductors. These networks exhibit a large surface-to-volume ratio ideal for absorbing large amounts of gas species. Typical mechanisms of gas detection include Schottky barrier modification at a metal (electrode)-semiconductor interface or charge transfer from adsorbed molecules into the network which influences its conductivity.

Memensors analyzed in this study are based on CdTe-Aerographite for gas sensing and CdS-Aerographite as well as InP-Aerographite composites for pressure and strain sensing. In the case of gas sensing, the hollow aerographite CdTe composite can be considered as a conducting scaffold (aerographite) with CdTe functionalization on its outside. Gas species existing in the surrounding environment are adsorbed on the scaffold and decoration. The current theory explaining the resulting gas response - i.e. the change of electrical resistance by a factor of up to 100 % - postulates that a charge transfer occurs from adsorbed gas species to the conducting scaffold, therefore changing the electrical conductivity. The functionalization layer serves as a catalyst supporting the charge transfer. It has been proposed by

several authors, that gaseous ammonia reduces the sensor surface thereby reducing the majority carrier concentration of the conductor and thus increasing the electrical resistance.[25], [26] Whether the reduction is of the actual CdTe or of an ultrathin oxide layer formed through adsorbed oxygen remains unsolved so far.

The CdS- and InP-Aerographite pressure and strain sensor are based on the piezoresistive response of CdS and InP when subjected to an external force. Unlike bulk piezoelectric materials, such highly porous structures are completely subjected to the pressure of a surrounding gas. In bulk materials, on the other hand, only areas proximate to surfaces are subjected to external pressures.

2.4 Other memristor concepts

Other memristor concepts commonly at the center of research activities are phase change memory (PCM) and thermochemical memory (TCM). PCM cells rely either on a reversible phase change or local, filamentary crystallization of an amorphous matrix upon application of an electric field. TCM cells are a subset of VCM cells where a Joule heating induced temperature gradient makes for the resistance change and local chemical changes are secondary.

A unique concept pursued in the research unit is the MemFlash, or electrically erasable and programmable read only memory (EEPROM), cell. As the name suggests, these are based on flash memory transistors. When wiring together the transistor's source and gate vias the transistor becomes conducting whenever a voltage is applied between source and drain. Because of an added tunnel window in the floating gate dielectric some of the charges flowing from source to drain can tunnel into the floating gate and are stored there. The more charge is stored in the floating gate the more conductive the channel from source to drain becomes, similar to a permanently applied gate voltage in classical transistor. Such cells have fabricated in the research unit, the only application of electron microscopy on these devices was the verification of the etching depth of the tunnel window. For further information on this concept the reader is referred to the works by Henning Winterfeld.[27], [28]

Chapter 3

Methods

The methods employed for analysis are all based on transmission electron microscopy. The general workings of these microscope shall not be discussed here, as they are well established and documented elsewhere. The reader is referred to the standard works by Williams and Carter[29], as well as Reimer and Kohl.[30] For specific descriptions of scanning transmission electron microscopy (STEM), the book by Pennycook and Nellist[31] is also highly recommended. For general information about electron energy-loss spectroscopy (EELS) which was extensively used in this thesis the excellent overview by Egerton can be consulted.[32] However, as especially EELS is central to this thesis, some aspects of it as well as important issues of the energy-loss near edge structure (ELNES) are being discussed. Furthermore, sample preparation is the basis of any TEM analysis and key points shall also be addressed here.

3.1 Sample preparation

There are a number of established and widely used methods for preparing solid-state samples for the TEM such that they retain their original makeup – i.e. do not gain any artifacts during preparation – and are still electron transparent. Among these, scanning electron microscope (SEM)-based focused ion beam (FIB) milling was required to prepare samples from the wafer scale double barrier memristor. As previously mentioned, these devices are only a few micrometer in size laterally and only few nanometers thick implying that FIB is essentially the only option for reliable sample preparation. As FIB milling relies on high energy (5-30 kV acceleration voltage) gallium ions to systematically bombard and thus mill the sample there are several known artifacts occurring during this type of sample preparation.[33]–[35] Artifacts that are both easily avoidable and easy to spot if they occur are gallium ion implantation and curtaining. The latter refers to a situation where differences in sputter rate on the sample material cause an uneven milling and thus sample

thickness.¹ None of the samples analyzed in this thesis showed Ga ion implantation, which would have been easily detected in energy dispersive X-ray (EDX) spectra. Curtaining occurs occasionally and is mainly caused by an uneven Pt protective layer deposited on top of the sample before FIB milling. Curtaining curtails the sample quality in areas where it causes less milling and thus a higher sample thickness. A prevalent artifact is the amorphization of surface layers of the FIB sample. This is caused by penetration of the amorphization layers by Ga ions, not to be confused with the implantation and alteration of the sample by deep Ga ion implantation. This amorphization can be hampered but rarely avoided. However, post-treatment by low energy (100-1000 eV) argon ions can remove this amorphization layer without inducing any further artifacts into the sample.[36] All samples prepared by FIB milling have been subjected to this post-treatment.

Other artifacts could be induced ballistically because of the high momentum of the Ga ions. Back side thinning can be the remedy to avoid this artifact or to check whether this occurred during the standard front side thinning.[37] Back side and front side refer to the thinning direction either from the Pt side (front side) or from the Si side (back side). The advantages of back side thinning are plenty. One can save time during deposition of the protective Pt layer, because a thin layer is sufficient as it is not removed as strongly during the thinning process. Instead the entire underlying wafer serves as a protective layer. This is advantageous not only because the Si is much thicker than the Pt layer (some 10 to 15 μm depending on the depth of trenches before lift-out instead of about 1 μm of Pt) but also because the Si is inherently much more uniform and thus prevents curtaining. Also the back side is typically made from a pure Si wafer and does not contain all kinds of carbon species like the Pt, a residue of the organic Pt precursor molecule used for deposition. The drawback, however, is that back side thinning requires the sample to be turned by 180° between lift-out and thinning which requires either a specialized micromanipulator or a so called flip stage. Notwithstanding the rarity of both these devices, back side thinning has been employed on one sample. As front side and back side thinning showed congruent results, it is safe to assume that no directional artifact was induced by the beam. A closer look at the results is shown in section 4.1.

3.2 Elemental quantification, EELS and ELNES fingerprinting

The most extensive investigation was the analysis of oxidation states in the DBMs. The most common methods to determine the oxidation state with nanometer resolution is done by elemental quantification, i.e. calculating the anion to cation ratio,

¹Sample thickness refers to the thickness of the electron transparent sample along the beam. Layer thickness refers to the laterally resolved extent of the layers, therefore its thickness determined by fabrication parameters.

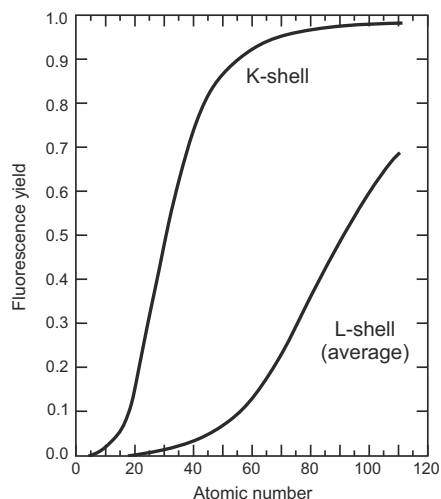


FIGURE 3.1: Fluorescence yield as a function of atomic number. Energy that is not emitted as characteristic X-rays is emitted in the form of Auger electrons. After [40].

or by probing the local electronic structure by EELS. As exact elemental quantification is notoriously erroneous and relies either on simulating spectra or on model based quantification, the identification and matching of the electronic structure with reference spectra – called ELNES fingerprinting – is generally faster and more exact. EDX spectra are influenced by sample geometry, detector geometry, spurious X-rays, sample composition and other factors; their quantification is either done with empirical k-factor quantification, model based ζ -factor quantification or simple comparison with reference data. None of these methods are particularly accurate and allow for a reliable determination of oxidation states. EDX spectroscopy of light elements, such as oxygen – also generally suffers from poor fluorescence yield (cf. Figure 3.1) and extremely poor solid angle of the detectors; even the best EDX detectors generally detect only around 5 % of the emitted characteristic X-rays[38] aside further limitations through adsorption by the sample holder.[39] EELS on the other hand is not curtailed by a poor fluorescence yield because it does not rely on a secondary emission process. All inelastic scattering processes of the TEM’s electron beam with the sample atoms are represented in the absorption spectrum, i.e. both the emission of characteristic X-rays as well as the emission of Auger electrons. Of course, EELS also suffers from some drawbacks. The model based quantification requires the absorption edges of all elements to be quantified to lie in the same spectrum. Absorption edges that are far apart from each other are hard to record simultaneously because absorption at low energies are generally much more intense than edges at high energy, thus lower energy edges “overshadow” high energy edges. Also, recording the edges simultaneously requires a comparatively small energy dispersion, thus restricting energy resolution and obscuring details in the ELNES. Oxide identification by ELNES fingerprinting obviously requires reference spectra of the respective absorption edges, for most binary metal oxides these can be found in literature though. Generally EELS is advantageous for recording low Z elements as compared to EDX

because of the aforementioned poor fluorescence yield of light elements. A limiting factor for EELS is the absolute energy-loss of the core-loss edges of interest. Absorption edges at low energies (up to 50 eV) are often times impaired by overlapping plasmon losses and the strong background of the zero loss peak. On the other hand, absorption edges at higher energies (more than 1500 eV) are generally weak, because the transitions belonging to these energies are less probable. Thus, generally speaking edges in the intermediate energy range from 50 to 1500 eV are the most meaningful. Edges in this energy range that are of interest in this thesis are for example Al – L₂₃ (73 eV), Nb – M₄₅ (205 eV), O – K (532 eV) and Al – K (1560 eV). The carbon C – K edge (284 eV) also lies in this range and sits on top of the Nb – M₄₅ edge thus occasionally obscuring its features. Hence, contamination with atmospheric hydrocarbons is especially disadvantageous, as this common artifact of TEM investigations not only renders spatial resolution but also ELNES fingerprinting.

3.3 Defects in EEL spectra

Aside from fingerprinting, the ELNES can also unveil deviations, i.e. defects, in the electronic structure if these defect states lie above the Fermi energy so that they constitute empty states. As the principle of (core loss) EELS is to excite core electrons through inelastic scattering with beam electrons into empty states the resulting spectrum is essentially a convolution of the energy spread function of the electron beam with the empty local density of states (LDOS) above the Fermi energy and the LDOS of the excited core electrons. As the latter are highly localized the entire loss spectrum can be interpreted as a measure for the LDOS of the material, rather than a generalized DOS. In the case of K edges – this means that the excited core electrons originates from the shell – it is a good approximation that there is only one energy level of the K shell, therefore the LDOS of the excited core electron ideally is of the form $\text{LDOS} \delta(E)$, therefore the deconvolution is its identity. There are further effects contributing to the spectra, such as plural scattering and an inelastic background as well as other elastic effects, however, these are often times either easily removed from the spectrum or negligible in their extent. This means, that an energy-loss spectrum – after background subtraction and removal of plural scattering by deconvolution with the zero loss peak – is proportional to the empty LDOS of the material.

3.4 Spectroscopic selection rules

Selection rules - specifically the dipole selection rule (LaPorte rule) and spin selection rule - govern the shape of *optical* emission and absorption spectra.

The LaPorte rule states that electronic transitions in centrosymmetric atoms, complexes and molecules can only occur if the initial and final states of the electron undergo a parity inversion. An atom is considered centrosymmetric if it only contains

centrosymmetric orbitals. Therefore transition from even-to-even (g to g) orbitals and odd-to-odd (u to u) orbitals are forbidden. Less abstract this means that if the center of electric charge does not change between initial and final wave functions no dipole is induced and therefore no coupling with electromagnetic radiation can occur. In the easiest case this happens during a transition between two s orbitals. The center of electric charge of the centrosymmetric s orbitals is always their common central point; no dipole moment is induced and therefore this transition cannot be excited by electromagnetic radiation.

The same principle applies in EELS, but inversely; it applies to the emission process during relaxation of excited states. The typical experimental setup in a TEM - as it was used in all measurements presented in this work - limits the collection semi-angle β of the spectrometer to about 16 mrad. Therefore, only strongly forward scattered electrons of the electron beam can enter and pass through the collection aperture and are recorded. The inelastic processes that the beam electrons excite in the sample are strongly forward scattered, therefore constitute of those *not* involving a large transfer of momentum. This is case in photon-coupled processes, i.e. processes where the energy is transferred not to an Auger electron but to a characteristic X-ray. In order to excite a characteristic X-ray a dipole has to be induced between the initial and final wave function of the excited electron and thus the dipole selection rules apply. This is particularly important, as this implies that interpreting the loss spectrum as the LDOS is heavily augmented by the dipole and spin selection rules. Accordingly, the loss spectrum recorded on K edges - where $1s$ electrons are excited - indicates mainly empty p states, whereas L_{23} edges - where $2p$ electrons are excited - are dominated by empty d states.

3.5 Tomography and tomographic reconstructions

Tomographic analysis allows to produce 3D representations of objects. This technique can not only be applied to macroscopic objects, but also in TEMs to produce 3D images of nano- and microsized samples. This is particularly important as TEM generally suffers from the lack of ability to discern between up and down in a sample. As samples are transmitted by the electron beam all TEM images regardless whether they are recorded in TEM or in STEM mode or whether they are bright field or dark field images can be interpreted as "shadow images" of the sample. If two objects are on top of another along the electron beam they produce a common "shadow" and one can therefore not discern if one object is in front of the other or vice versa.

A remedy to this problem is tomography. For this technique images are recorded from multiple angles and afterwards merged by a reconstruction algorithm to form the 3D representation of the recorded object. In TEMs this is accomplished by tilting the sample holder around a rotation axis parallel to its long axis, commonly called

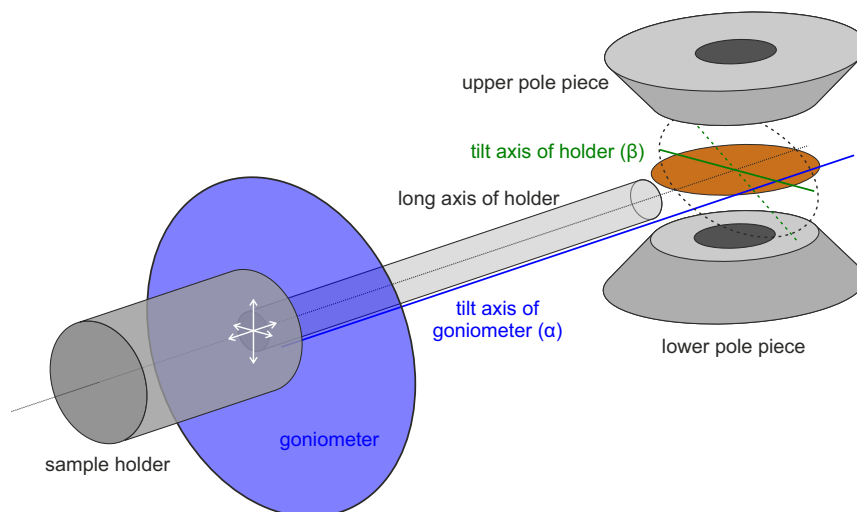


FIGURE 3.2: Geometric sketch of goniometer and sample holder. The tilt axis of the goniometer (blue) is parallel to but not coinciding with the long axis of the sample holder allowing adjusting the X-Y sample position as well as eucentric height in Z direction independently from the tilt axis. This is not possible for the tilt axis β (green) which cannot move relative to the holder. The pole pieces restrict the alpha tilt to certain values. Sketch is not to scale.

the α angle. Most sample holders also allow tilting the sample around a second axis perpendicular to the long axis of the holder, called β . Tomography can effectively only be conducted while tilting around the α angle. This is because the rotation axis is set by goniometer of the microscope and not by the holder, unlike the β tilt which is fixed to the sample holder and whose rotation axis cannot be moved relative to the sample. Physically, the reason for this is the goniometer responsible for the α tilt acts as a trunnion while the β tilt has a fixed rotation axis like a hinge.(cf. Figure 3.2) In turn, this also implies that the eucentric height for each and every sample position in the microscope can only be set for the α tilt, the eucentric height for the β tilt cannot be manipulated and therefore only sample position lying exactly on the axis of rotation can be tilted without laterally moving them and changing their Z-height in the microscope which also changes their focal length.

This is a strong limitation, as it limits the sample tilt during tomographic analysis to a single axis. Furthermore, tilting the sample holder is limited by the dimension of the holder itself and the space in between the pole pieces of the objective lens. This distance is generally chosen to be very small, because the smaller the distance in between the pole pieces, the more homogeneous is the magnetic field confining the electron beam and thus the higher resolution of the microscope because of fewer lens aberrations. A small gap in between the pole pieces in turn also limits the tilt range and thus inherently hinders tomographic analysis. Even in microscopes optimized for tomography the tilt angles are limited to be smaller than + and - 90° because at high tilt angles the sample holder itself covers the sample, such that no images can be recorded.

While TEM- or STEM-based tomography is generally an established technique it therefore suffers from multiple challenges:

- As the measurements generally take a lot of time drifting of the sample must be accurately compensated to always record the same exact position of the sample.
- The prolonged measurement time also means that the area of interest is prone to be severely contaminated, but also particularly suffers from damage induced by the electron beam.
- Tilt angles in the electron microscope are limited by several constraints.
- The reconstruction algorithms are complicated and require a lot of fine tuning.

3.6 Instrumentation

TEM analysis was conducted on three different microscopes. Preliminary experiments were run a FEI Tecnai F30 G2 STwin at 300 kV with no monochromator and no Cs correction. This microscope is equipped with a Gatan Tridiem spectrometer model 863. The typical energy resolution achieved on this setup is around 1.4 eV. It is also equipped with an EDAX EDX detector and has STEM-EDX, but no reliable STEM-EELS capability.

Particularly for the DBMs, the intricate details of electronic structure are utterly important. Therefore, through the EU funded projects „Enabling Science and Technology through European Electron Microscopy“ (ESTEEM2 and ESTEEM3) access to the microscopy facility of the Technical University of Graz FELMI-ZFE was gained. Their state-of-the-art FEI Titan³ STEM is operated at 300 kV, equipped with an XFEG and a monochromator limiting the energy resolution to well below 250 meV. The Gatan GIF Quantum spectrometer allows DualEELS acquisition, i.e. acquisition of the ZLP and the core loss region simultaneously, therefore enabling energy-loss alignment and deconvolution of the core loss spectra at every single point of a STEM experiment. Additionally, the STEM has a ChemiSTEM EDX detector consisting of four individual EDX detectors placed around the sample region, drastically improving the amount of X-rays collected and also being independent from the tilt angle of the sample.

Tomographic analysis was conducted on a JEOL JEM-2100 capable of STEM tomography. The maximum tilt angle with a holder optimized for tomography is around 61°. The microscope operates at 200 kV and is equipped with a LaB₆ cathode. Its nominal resolution is lower than that of the previously mentioned FEI microscopes but it has advantages in long term stability, i.e. especially beam movement and sample drift, making it suitable for extended tomography analysis.

3.7 Conventions within this study

In order to make this thesis as comprehensible as possible the following conventions are being used throughout this work:

1. The color coding for elements, particularly in the DBM section is fixed and described in Table 3.1.
2. Layer sequences are always written from top to bottom.
3. Images are always rotated such that the top electrode is at the top of the image.
4. EDX line scans that go from the top of an image to the bottom are displayed from left to right.

TABLE 3.1: Color coding for elements in this study. Oxides are mixed RGB colors of the metal and oxygen, e.g. AlO_x is green and blue, so cyan.

Element	Color
Au	yellow
O	blue
Al	green
Nb	red
Hf	orange

Chapter 4

Investigations on Double Barrier Memristors

The double barrier memristor has been introduced in Chapter 2. In the following, devices in the high resistance and low resistance state (HRS and LRS) are being analyzed to check whether there is a detectable difference between the two and if so what that difference is. Possible explanations for the changing resistance state are either accumulation of surface charges or movement of charged defects in the Schottky barrier. Attempts to analyze these devices by dynamic X-ray photoelectron spectroscopy (XPS) remained inconclusive. While XPS generally offers even better energy resolution than EELS it inherently lacks the spatial resolution. However, in the case of such layered materials depth resolution is by far the more crucial parameter. While XPS generally offers good depth resolution it is hard to pinpoint from which depth a given signal stems; the signal generating depth of XPS is on the order of a few nanometers, which automatically spans all of the layers. Dynamic XPS was used to remove the surface layers by sputtering and create an elemental depth profile through intermediate XPS measurements. This, too, remained unsuccessful; while the general layer sequence was resolvable, the intricate sub-nm details were kept concealed. Accordingly, extensive TEM work was necessary to address the following questions:

1. What is the exact layer sequence, is there interdiffusion or migration of oxygen ions?
2. How thick are the respective layers and what is the surface roughness?
3. What is the chemical composition and oxidation especially of the oxide barrier layers?
4. Is there an observable difference between high and low resistance states?

4.1 Preparation

Before preparation of the samples, each samples was electrically characterized as to correlate their nanoscopic layout with its electrical properties. The fabrication of devices and electrical characterization was conducted in the subproject "Memristive,

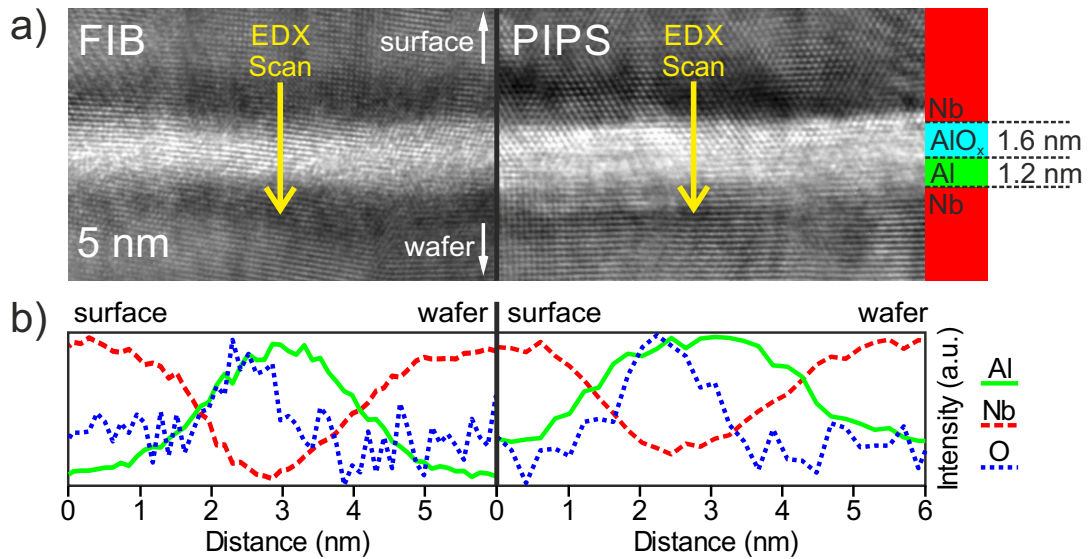


FIGURE 4.1: Comparison of the identical sample prepared by FIB and PIPS. a) High resolution TEM (HRTEM) micrographs of the FIB (left) and PIPS (right) prepared sample. While the resolution of the PIPS-prepared micrograph is higher (as determined by the FFT power spectrum) they are qualitatively the same. Yellow areas indicate where EDX scans in b) have been acquired. b) Comparison of EDX line scans of the FIB (left) and PIPS-prepared (right) sample. Both scans show qualitatively the same, specifically the partial oxidation of the Al layer on the surface-facing side, while the wafer-facing side appears metallic.

quantum mechanical tunnel junctions and MemFlash cells" by Mirko Hansen and his successor Finn Zahari. In order to answer the questions posed in the previous section, reliable sample preparation without inducing artifacts had to be established. To this end, in a preliminary step the sample preparation by FIB milling – which was required for the site specific lift-out of the memristive devices – was put to the test. The protocol for testing consisted of comparing a sample prepared by FIB milling with a sample prepared with a precision ion polishing system (PIPS). As the PIPS preparation utilizes low energy Ar ions instead of highly energetic Ga ions, it is universally accepted that PIPS produces no or at least minimal artifacts.

The HRTEM images displayed in Figure 4.1 a) show comparable areas of FIB and PIPS prepared samples. The sample material stems from the identical original stock material. This dummy sample was prepared from a Josephson junction closely related to the DBMs the only difference being the Nb oxide layer Schottky barrier which is missing in the here presented Josephson junction. Still, the sample exhibits the same Al-AlO_x layer and importantly, Josephson junctions are well established and analyzed by various techniques in literature. Its layout is therefore well explored and the TEM samples can be compared this expectation. What is more, the Josephson junction has been electrically characterized before TEM sample preparation, such that it's confirmed to exhibit an ultra-thin Al oxide layer and otherwise only metallic components.

These expectations are fully confirmed by TEM analysis. The HR micrographs show a thin partially crystalline layer in between two highly crystalline darker layers. The

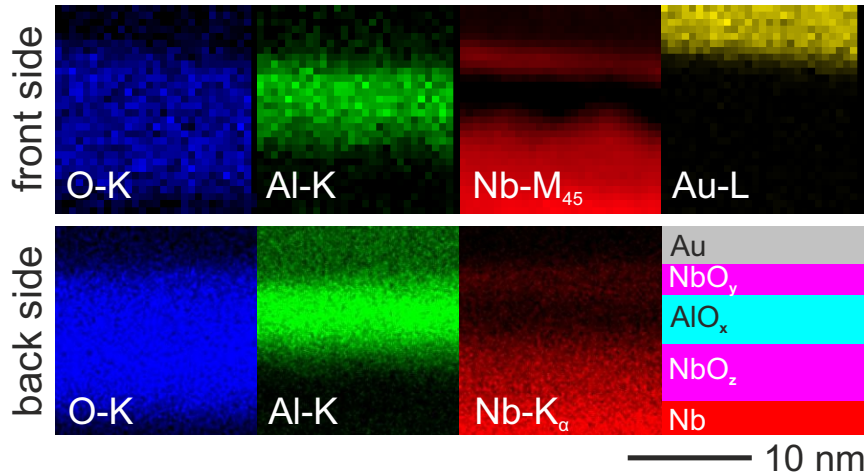


FIGURE 4.2: Comparison of DBM devices prepared by FIB front side thinning (top row) and back side thinning (bottom row) displaying the Au/NbO_y/AlO_x/NbO_z/Nb (top to bottom) layer sequence. The EDX analysis of the back side thinned sample has a much higher spatial sampling rate, other than that the results are congruent, and the oxide layer present in both samples is of comparable extent. In the bottom right the layer scheme valid for both analyses is presented.

EDX scans in b) (see yellow arrows) measured across this multilayer confirm that the layer sequence is indeed Nb/AlO_x-Al/Nb from top to bottom. The EDX scans from both samples are congruent and nicely indicate the partial oxidation of the Al layer on the surface facing side. This partial oxidation is accomplished by thermal oxidation with an oxygen partial pressure inside the vacuum chamber. Al is known to exhibit self-limiting oxidation of around 1.5 nm which closely corresponds to the presented results. Importantly, the FIB and PIPS prepared samples show qualitatively congruent results. The main difference is the higher quality of the HR micrograph of the PIPS prepared sample and its higher spatial resolution as determined by the Fourier power spectrum (not shown). The main result of this investigation was proof that FIB milling can be successfully applied to such thin multilayers without introducing severe artifacts, such as displacement of oxygen ions. Another insight was that the spatial resolution of these FIB lamellae was somewhat limited due to their higher thickness compared with PIPS prepared samples. This was later fixed for the DBMs by post-treatment with low energy argon ions. PIPS by itself could not be applied to the DBMs due to inevitable requirement for site-specific sample preparation which PIPS cannot accomplish. In addition to this step, FIB milling was carefully examined by comparing front side and back side milling to check whether there are directional artifacts such as selective ballistic displacement of atoms in the sample. Again, it was found that both preparation methods show qualitatively the same outcome (cf. Figure 4.2).

On top of that, all samples have been subjected to post-treatment with low energy Ar ions of 900 eV. This accomplishes (a) removal of the amorphization layer induced by FIB milling, (b) reduces sample thickness which improves spatial resolution and EELS signal quality, and (c) removes any potentially present redeposition from FIB

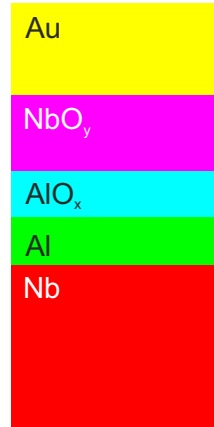


FIGURE 4.3: Schematic representation of the expected layer sequence in the first generation DBMs.

milling. The latter is occasionally observed through the presence of Si atoms, stemming from the milled substrate, in non-Si containing layers above the substrate. As this rare artifact is also removed by the Ar ion treatment it has not been observed in this thesis.

Aside from the purely technological aspects of sample preparation, the correct methodology for analyzing these samples has to be applied. First and foremost, this includes ensuring that the prepared sample is accurately perpendicular to the electron beam during analysis. Otherwise, layers might overlap along the beam direction, mimicking interdiffusion where there is none, or layers might appear broader or narrower depending on the degree of tilt between beam and sample. Alignment of the samples inside the microscope has always been provided by orienting a $\langle 110 \rangle$ direction of the Si wafer underneath, along the electron beam which was checked with the corresponding Kikuchi pattern. The accuracy for this procedure is expected to be better than 0.1° . This of course assumes that the wafer exhibits a $[111]$ orientation of its surface such that all layers deposited on the wafer are parallel to $[111]$. As $\langle 110 \rangle$ directions are perpendicular to $[111]$, rotation around $[111]$ is allowed and does not lead to overlapping layers, other rotations are not allowed.

4.2 First generation DBM

From the deposition parameters a layer sequence of Au/ NbO_y / AlO_x -Al/Nb was expected as displayed in Figure 4.3. The deposition of Al on top of Nb is known to effectively reduce surface roughness. The partial oxidation of the Al layer is achieved by self-limited thermal oxidation; the resulting AlO_x layer serves as the tunnel barrier. The NbO_y layer above is deposited by reactive sputtering with an Ar/O plasma. The total thickness of the two oxide layer is expected to be on the order of 3 to 5 nm. In a comparative study, biased and unbiased samples are being analyzed and contrasted against each other to check if there is any detectable difference between the two. Biased and unbiased refers to whether the samples are in

their high resistance or low resistance state.

4.2.1 Preliminary analysis

Preliminary experiments on the FEI Tecnai TEM in Kiel suggested a different layer sequence, particularly because in the acquired HR micrographs (Figure 4.4) an amorphous layer of more than 10 nm thickness is visible. The here presented data stems from a biased sample (342).

Furthermore, chemical analysis by EFTEM showed the presence of a much thicker oxide layer. The correlation of EFTEM and HRTEM (Figure 4.5 a) and b)) prove that the entire amorphous layer is at least partially oxidized. The STEM-HAADF image shown in Figure 4.5 c) generally proves the existence of four layers with different chemical composition. Unfortunately, due to poor spatial resolution in this image no more significant statements can be derived from this image. The subsequently acquired EDX line scans (Figure 4.6) and maps underline this results, though, and prove that the amorphous layers visible in the HR micrograph are the Al oxide tunnel barrier at the top and an underlying at least partially oxidized Nb oxide layer. The expected Nb oxide Schottky barrier in between Au and Al oxide is not visible in this scan, likely due to lack of spatial resolution as suggested by Figure 4.5 c). In a lower magnification STEM-HAADF image (Figure 4.7) in which the contrast and

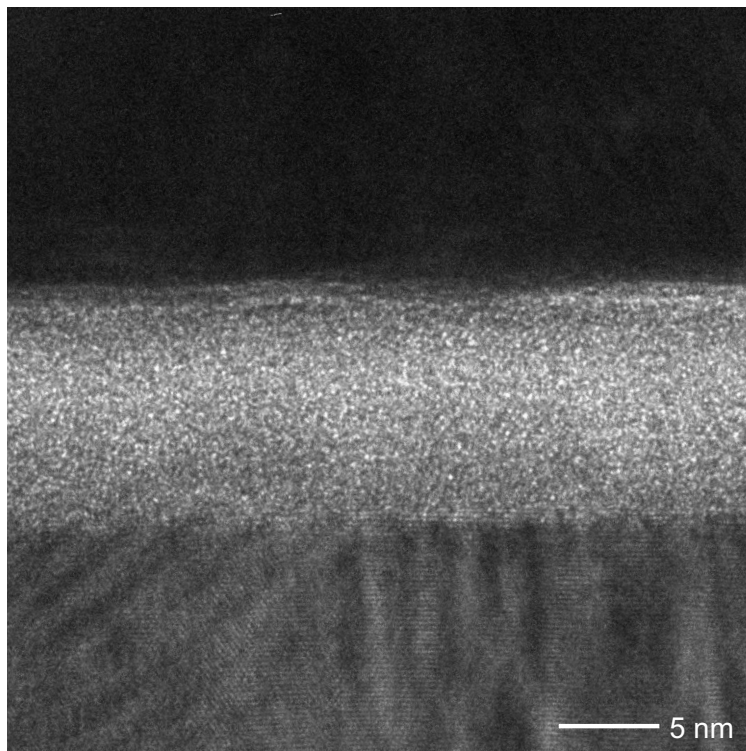


FIGURE 4.4: HR micrograph of the first generation DBM. The Au electrode at the top and the Nb electrode at the bottom are polycrystalline, the layers in between appear amorphous. The total thickness of the amorphous region is approximately 10 nm. A slight difference in contrast is discernible in the amorphous region; the top half appears a bit brighter than the bottom part.

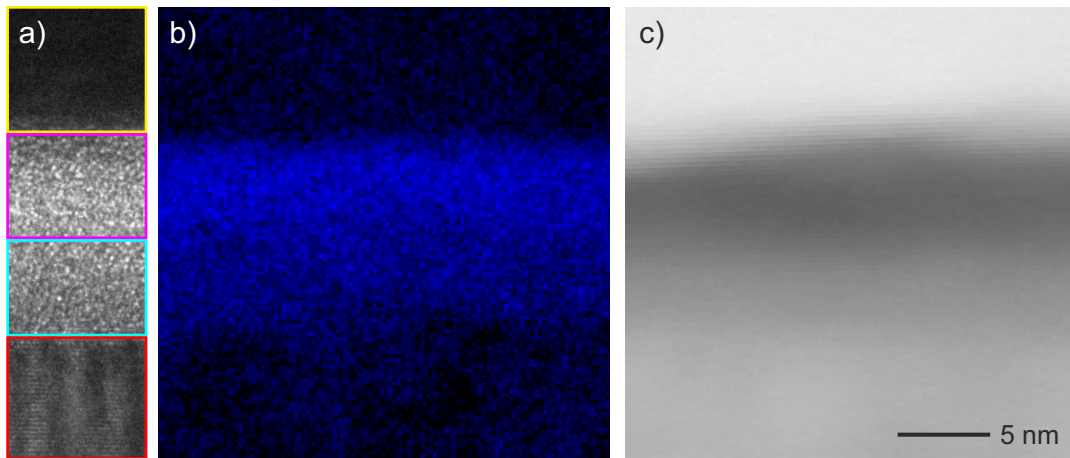


FIGURE 4.5: EFTEM analysis of the DBM and correlation with HRTEM and STEM. a) Cut-out of Figure 4.4. The colored frames indicate the regions which appear visually different. The yellow frame marks the Au electrode, magenta the slightly brighter and cyan the darker of the two amorphous regions. Red marks the Nb bottom electrode. b) EFTEM image of the O-K edge. The intensity of the mapped edge decreases gradually from top to bottom indicating a higher oxygen content near the Au electrode than near the Nb electrode. c) STEM-HAADF image of the same area, also showing four areas of different contrast. As HAADF contrast is proportional to Z^2 this indicates the presence of at least four chemically different layers.

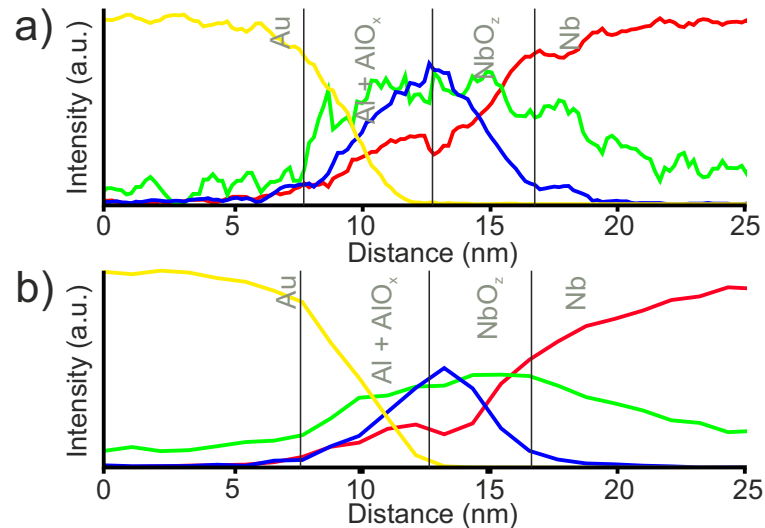


FIGURE 4.6: Distribution of chemical elements across the DBM. a) EDX line scan across the layers shown in Figure 4.3 from top to bottom. The presence of the Au electrode, Nb oxide, Al oxide and Nb metal is confirmed and correlates to the four layers visible in the HR micrograph. b) Same as a) except this is an EDX map integrated along the layers showing qualitatively the same result.

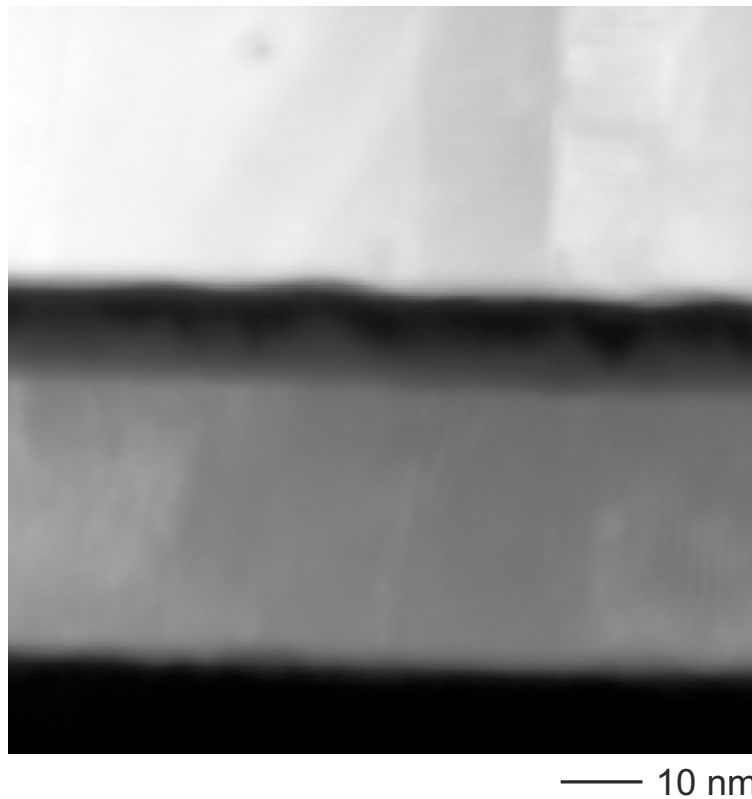


FIGURE 4.7: Lower magnification STEM-HAADF image of the DBM. The oxide layer in the middle is separated by an interface with considerable surface roughness.

brightness have been manipulated to improve distinguishability of the two amorphous oxide layers a rough interface between the two layers is clearly visible. Correlation with the previous results suggests that the darker (lower average Z) layer is Al oxide and the slightly brighter (higher average Z) layer is Nb oxide. As no reliable 2D EDX mapping could be recorded, this results is only further interpreted after the following results.

The main result of these initial experiments was that the deposition seemed to have produced a layer sequence different from the expected one, as the back electrode clearly shows significant oxidation of several nm depth. However, in order to address the questions posed above, it was also clear that the instrumentation available in Kiel would not be sufficient as neither a C_s -corrected and monochromated TEM nor the ability for Ar post-treatment of samples was given. Also, as the differences between devices in the high-resistance and low-resistance state are supposedly minute, it is expected that no difference between the two is visible in this investigation.

Therefore, further investigations were continued in the framework of the ESTEEM2 network on the dedicated at the Center for Electron Microscopy of the Technical University of Graz. As the microscope at the University of Graz is a dedicated STEM without a TEM mode, all investigations were complemented by HRTEM investigations at the FEI Tecnai in Kiel.

TABLE 4.1: Overview table of analyzed DBM samples.

SB oxide	Generation	Elec. characteristic	Resistance state	Name
Nb	1	switching	LRS	Nb-1-sw-LRS
Nb	1	switching	HRS	Nb-1-sw-HRS
Nb	1	switching	LRS	Nb-1b-sw-LRS
Nb	2	switching	LRS	Nb-2-sw-LRS
Nb	2	non-switching	LRS	Nb-2-no
Hf	2	switching	LRS	Hf-2-sw-LRS
Hf	2	non-switching	LRS	Hf-2-no
Nb (anodic)	2	N/A	-	Nb-2-no-anodic
Nb (thermal)	2	N/A	-	Nb-2-no-thermal

4.2.2 In depth spectroscopic analysis of DBM

After the preliminary experiments which already hinted at the discrepancy between expected and actually deposited layer sequence an in depth investigations was conducted at the C_S probe-corrected, monochromated FEI Titan STEM at the Center for Electron Microscopy in Graz. The samples analyzed here were treated with low-energy Ar ions before the STEM analysis for the benefits described above. The samples described in this chapter from the first generation and second generation of DBM are displayed in Table 4.1. The sample labelled Nb-1b-sw-LRS is different from the other two first generation devices as it was prepared with a different Ar/O ratio during reactive sputtering of the NbO_y Schottky barrier. The second generation was fabricated after scrutinizing the sputter parameters. Furthermore, as it was found that the reactive sputtering of Nb oxide had an influence on the oxidation of subjacent layers, test samples were fabricated where the Schottky barrier was anodically and thermally oxidized to circumvent this problem.

The analysis of spatial elemental distribution was carried out by combined STEM-EELS/EDX investigations. This allows to simultaneously map light elements (like oxygen) in EELS as well as heavier elements like metals, particularly the gold top electrode. ELNES fingerprinting was carried out afterwards in order to accurately determine oxidation states of the layers of interest.

Spatial elemental distribution

Figures 4.8 to 4.10 show the spatial elemental distribution of the first generation DBM. The results are generally congruent with results from the preliminary analysis presented in section 4.2.1 but show the layers to greater detail. In particular, the interface between Nb and Al shows pronounced surface roughness, which was not visible in Figure 4.5. The sample thickness - as determined by the log-ratio method

[41] - is well below 30 nm, while the observed surface roughness is on the order of 1-2 nm. Therefore, due to the overlapping 3D surface roughness along the beam direction, regions of apparent overlapping Al and Nb signal visible in the EDX line-scans of Figure 4.6 are minimized in the in-depth investigations.

The memristive switching mechanisms discussed by Hansen *et al.* [22] rely on interfacial trap state between the Schottky barrier and gold electrode as well as movement of oxygen ions within the Schottky barrier. While these models have only been postulated tentatively they do underline that the difference between LRS and HRS might be extremely subtle. The elemental maps of oxygen have deliberately been displayed with a white/blue instead of black/blue contrast to improve visibility which is otherwise poor in the common contrast mode, where black symbolizes no signal of the displayed signal and the respective color channel displays the signal magnitude.

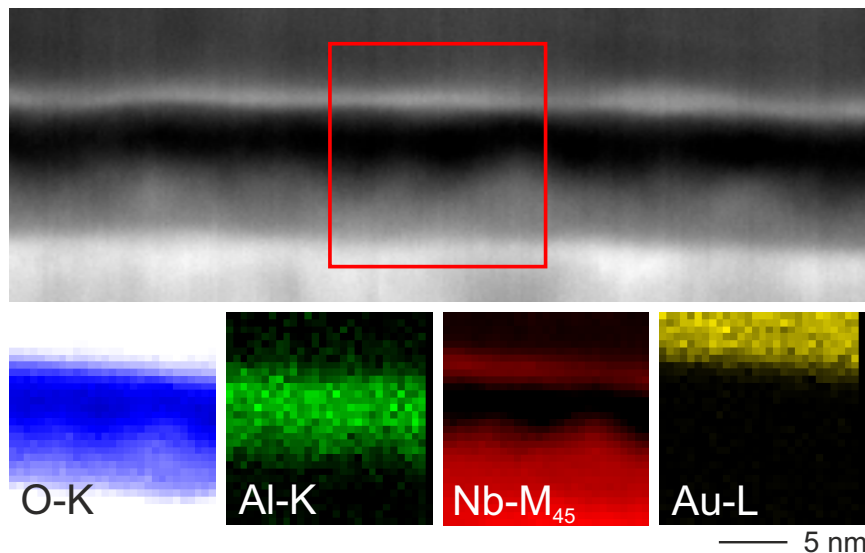


FIGURE 4.8: STEM-ABF image and spatial elemental distribution of Nb-1-sw-HRS determined by EDX (Al, Au) and EELS (O, Nb). Red square in the ABF image shows region where elemental distribution has been determined. The O-K map has a white instead of a black background to increase visibility.

However, all three analyzed samples exhibit a pronounced oxidation of the Nb back electrode. The oxide layer - as apparent from the combination of O and Nb elemental maps reaches a couple of nanometers into the back electrode. This pronounced oxidation is surprising in particular for two reasons. Firstly, the Al layer was expected to be only partially oxidized, similar to the results presented in Figure 4.1; an AlO_x layer of this thickness is expected to simply act as an insulator. Secondly, an additional NbO_x layer potentially serves as another insulating layer. Nonetheless, the devices show the desired electrical switching. Aside these arguments from the functional side of view, the absence of metallic Al and the partial oxidation of the back electrode are of course also surprising because the previously analyzed Josephson junction (cf. Figure 4.1) did exhibit metallic Al and did not show any back electrode oxidation. Noteworthy is also the pronounced surface roughness

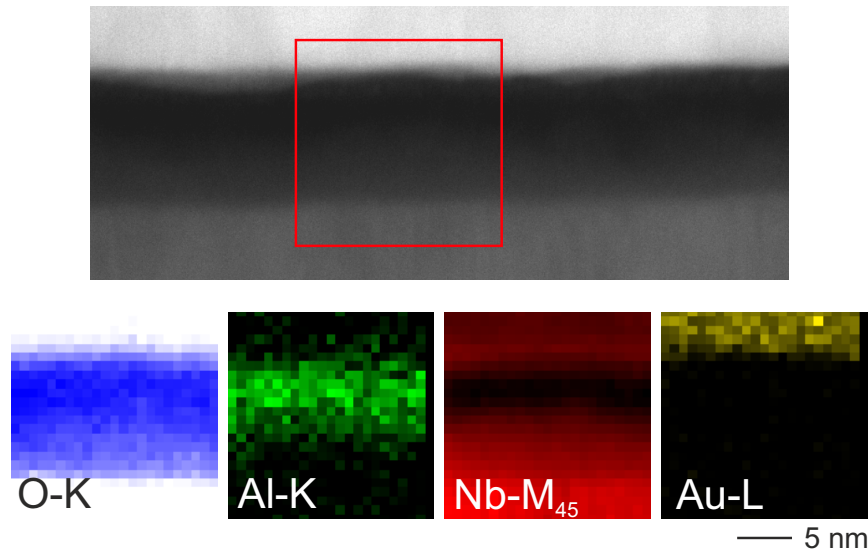


FIGURE 4.9: STEM-HAADF image and spatial elemental distribution of Nb-1-sw-LRS determined by EDX (Al, Au) and EELS (O, Nb). Red square in the ABF image shows region where elemental distribution has been determined. Presence of Nb signal in the Au top electrode is caused by the fitting algorithm used to create the maps which produces this misleading map due to the overall weak EELS signal generated from this sample.

between the back electrode and Al oxide tunnel barrier which is particularly obvious in the STEM-ABF image of Figure 4.8 but also in the Nb elemental maps from all three first generation devices. Opposite to the aforementioned investigations, this surface roughness was not observed in the Josephson junction. The results from samples Nb-1-sw-LRS and Nb-1b-sw-LRS are essentially congruent: considerable surface roughness between Nb and Al, absence of metallic Al, pronounced oxidation of the Nb back electrode. (cf. Figures 4.9 and 4.10). Contrary to the explicit aim of these investigations - finding and analyzing the difference between devices in HRS and LRS - no difference was found in the elemental distribution of these devices.

This of course raises the question where the oxidation originates from. The preliminary experiments regarding suitable methods for sample preparation showed with certainty that such oxidation will not be induced by FIB milling. As the deposition of first generation DBMs and Josephson junction are identical up to the Al oxide tunnel barrier, an obvious candidate for the induced differences is the subsequent deposition of the Nb oxide Schottky barrier by reactive sputtering. Whether this step could cause both the observed oxidation as well as a potential increase in surface roughness is still under investigation. Several investigations of the plasma characteristics such as the energy flux, plasma potential, temperature and Bohm current, which is the current of charged particles able to escape the plasma, are being conducted at present. During careful examination of the deposition process, in particular the exact geometry of targets and substrates it was noticed, though, that the distance between target and substrate potentially was not as originally designed, such that the reactive Ar/O plasma used for reactive sputtering of Nb oxide was potentially closer

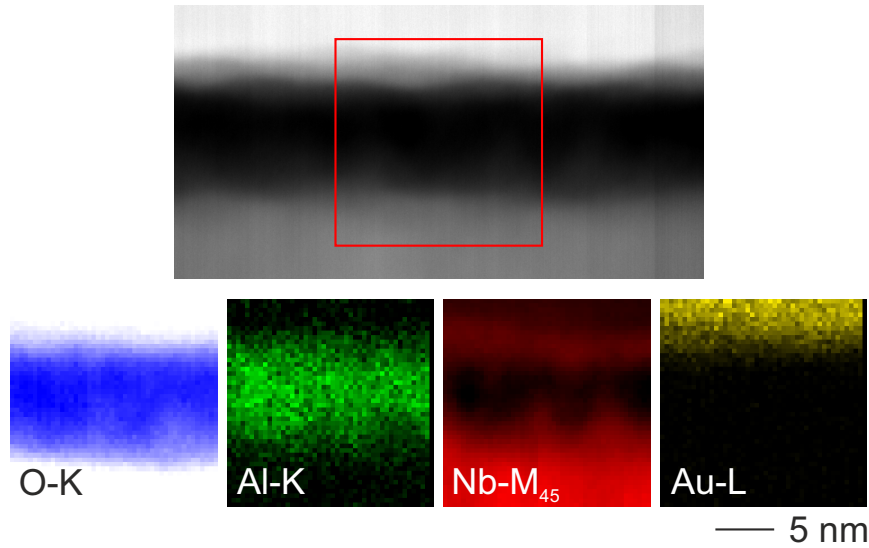


FIGURE 4.10: Spatial elemental distribution of Nb-1b-sw-LRS determined by EDX (Al, Au) and EELS (O, Nb). Red square in the ABF image shows region where elemental distribution has been determined. Presence of Nb signal in the Au top electrode is caused by the fitting algorithm used to create the maps which produces this misleading map due to the overall weak EELS signal generated from this sample.

to the substrate and is thus might be the cause of it. Aside exploration of plasma characteristics, further effort is put into researching the link between deposition parameters, microstructure and electrical characteristics. This also involves simulation of plasmas and their influence on the target and substrate materials. Such simulations are extremely challenging, as they need to bridge several orders of magnitude on both length and time scales.[42] For example, typical sputtering times are on the order of tens of seconds, while the vibration of adatoms on the surface substrate occurs with a frequency of 10^{14} Hz thus spanning some 15 orders of magnitude. The typical length scale of a substrate is several centimeters, while the size of an atom is on the order of Ångstroms thus spanning at least eight orders of magnitude. Thus accurately describing such a system by means of simulation is gigantic task.

From the O-K map in Figure 4.8 (and similarly in Figures 4.9 and 4.10) the difference in O-K signal in the separate layers is clearly visible. This difference in signal magnitude does not, however, translate directly to a difference in oxygen content. As Nb ($Z=41$) is much heavier than Al ($Z=13$) it absorbs more oxygen signal, accordingly a quantitative analysis is necessary to determine the oxidation state in each layer. A detailed and semi-quantitative analysis of the oxidation states is undertaken in the following section.

Spectral analysis, ELNES fingerprinting

Quantitative EDX analysis is possible with dedicated analysis software which takes into consideration sample geometry, overall presence of elements and specific absorption factors. However, even with modern correction algorithms inherent problems such as peak overlap or strong spurious X-ray signal. Spurious signal where

the electron beam focuses on a certain spot on the sample in STEM mode, the EDX detector, however, does not only record characteristic X-rays generated in this particular interaction volume but also in other locations which are generated by strongly scattered electrons. One example for this is the ubiquitous Cu signal generated in samples that are placed on Cu grids. Even though the grid itself is not irradiated by the electron beam, Cu radiation is present in virtually every single EDX spectrum because of spurious X-rays. This effect is also strong near interfaces of a heavy and a light material; such is the case in this sample with the Au-Nb oxide interface. When the electron beam is scanning over the Au electrode in close proximity to the underlying oxide layers, the Au atoms strongly scatter the beam electrons a fraction of which enters the neighboring oxide layers and generate spurious X-rays. Accordingly, Nb, O and Al signal is falsely recorded in places where there is none of these atoms. This effect is only so much more apparent in these samples because of the tiny dimensions of the layers and even more so the lack of channelling along atomic columns. If all of the constituents were crystalline and oriented along a low-index zone axis, the electron beam would be channelled along the atomic columns and less scattering would occur. Spurious X-rays can be observed in all previously presented elemental maps and likewise in all of the following elemental maps.

More reliable than quantitative X-ray analysis - under the aforementioned constraints - and simple elemental mapping is the analysis of EEL spectra by ELNES fingerprinting. Quantification of EELS cross-sections was often times rendered impossible because of overlapping edges. For example, in the case of Nb-M₄₅ (205 eV) and O-K (532 eV) edges there is generally no overlap, however, quantification is still curtailed by the C-K (283 eV) edge which obscures the delayed maximum of the Nb edge. In the cases of Hf-M₄₅ (1662 eV) and Al-L₂₃ (73 eV) or Al-K (1560 eV) the edges are simply too far apart to be reliably recorded within the same spectrum with reasonable intensities for both elements, i.e. recording the edge of one element without overexposing the camera with the much higher intensity of the lower energy element.

Accordingly, ELNES fingerprinting as described in section 3.2 is the most reliable method for identifying oxidation states in these samples. Figure 4.11 depicts the Nb-M₄₅ edge extracted from several first generation DBMs and averaged to reduce noise.

Figure 4.11 displays the Nb-M₄₅ edge as well as references by Bach et al [43] for Nb(V) and Nb(IV) and Nb(II) oxide. A direct correlation between spectra is not possible. Experimental and reference data have been acquired under different experimental conditions. Furthermore, background subtraction as well as removal of plural scattering can differ and thus cause distortions in the spectra. However, this does neither affect relative intensity between spectra nor position of spectral features. Therefore, the intensity of features can be compared between spectra as well as the position for example of the peak between 240 and 260 eV.

Several features are noteworthy; the feature near the onset of the edge between 200 and 225 eV is much more pronounced in both experimental spectra as compared to

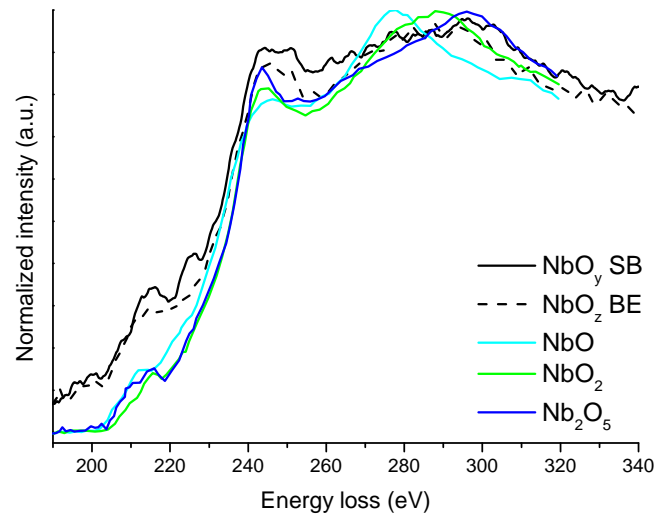


FIGURE 4.11: Nb-M₄₅ ELNES of the first generation DBM. The graph shows the ELNES extracted from an Nb oxide area near the bottom electrode (BE) and at the Schottky barrier (SB) alongside references for three different Nb oxides.[43] Experimental data has been smoothed by a 10-point adjacent averaging algorithm.

the two references. It appears as a twofold peak at 215.5 and 226.1 eV in the SB spectrum and a single peak at 215.5 eV in the BE spectrum. In comparison the reference spectra show a much weaker shape, however, the spectrum for Nb(V) oxide (blue) shows a tendency to form the strongest peak, whereas the Nb(IV) and Nb(II) reference form less pronounced features in this region.

The intensity of the peak close to 250 eV is stronger in the SB spectrum than in the BE spectrum, and similar to the previous feature the SB tends to resemble Nb(V) oxide because of its higher intensity and the BE's lower intensity is more akin to Nb(IV) or Nb(II) oxide. The position of this feature is almost identical for all five spectra, interestingly the intensity is split in the SB spectrum.

While this description and careful examination of features may seem tedious it does highlight that these EEL spectra are not unambiguously assignable to a certain phase but show a tendency to indicate a certain oxidation state. This can be founded in the fact that the experimentally observed spectra are not obtained from pure and crystalline phases with a distinct oxidation state but rather from an amorphous oxide potentially containing a mixture or local variations of oxidation states. What is more, as previously described, the C-K edge sits at 283 eV and thus even without any prominent intensity, organic contaminants might very well have an influence on the position and relative intensity of the maximum in the Nb spectra, which is located some 80 to 100 eV beyond the onset and thus directly below the C-K edge.

According to the only mildly conclusive identification of the Nb-M₄₅ edge a focus is set on the O-K edges as depicted in Figure 4.12. While the O-K edge generally suffers from the same problems described above, it does have a major advantage,

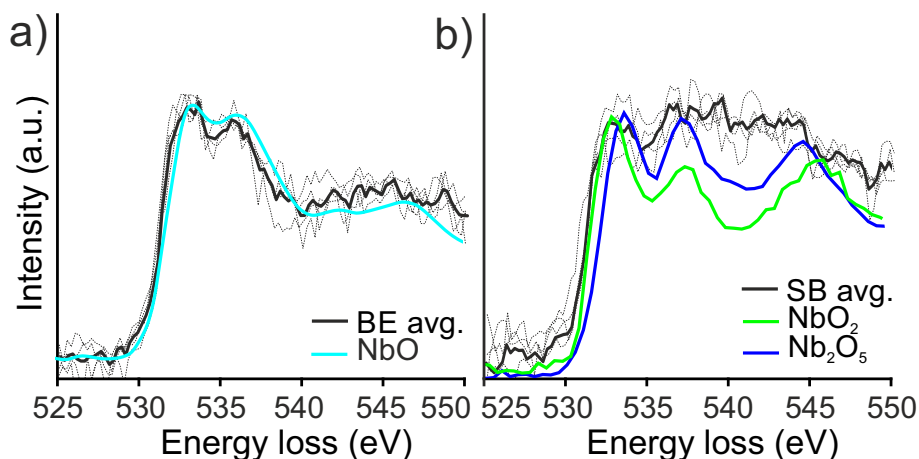


FIGURE 4.12: O-K ELNES from the SB of the first generation DBM. a) ELNES extracted from a region near the BE. b) ELNES extracted from a region near within the SB. Experimental data averaged from several measurements (black dots) is displayed as solid line. Reference data displayed in color. ELNES in a) nicely corresponds to the NbO reference, while ELNES in b) resembles neither of the references closely, but rather a mixture of the two. Experimental data were not only background subtracted but plural scattering was also removed, thus ensuring good comparability of the similarly treated references. This figure has been previously published in similar form in Reference [44].

being its shape. Unlike the Nb-M₄₅ edge with its delayed maximum, the O-K edge has a typical white-line or saw-tooth shape, where the onset and maximum can be compared and interpreted much easier.

As the shape of the O-K is much more unique between the SB and BE, it is not displayed on top of each other but rather side-by-side. In Figure 4.12 a) the BE spectrum can be seen alongside a reference of the O-K edge of NbO₂, b) displays the SB spectra alongside references for NbO₂ and Nb₂O₅. While the BE Nb oxide seems to be clearly assignable to NbO, the SB spectra are less distinct. However, especially the first maximum at around 533 eV appears to fit a combination of the two oxide references.

Both the previously analyzed Nb-M₄₅ edge as well as the O-K edge hint towards the same, namely the BE exhibiting a lower oxidation state - likely Nb⁺² - than the SB Nb⁺⁴ or Nb⁺⁵). This is also congruent with the relative intensities of the oxygen signal in the EDX maps presented in Figures 4.8 to 4.10. Even though it is known that oxides of niobium with a low oxidation state, such as NbO, are good metallic conductors, the pronounced oxidation of the bottom electrode was neither intended nor desired.

Unfortunately, just as in the analysis of elemental distribution, no difference was found in the absorption spectra of the SB between LRS and HRS, which can have multiple reasons:

1. there is no difference, because there is no correlation with elemental distribution and resistance state,
2. there is no difference, because the retention time was smaller than the time between setting the state and analysis,

3. there is no difference, because the sample preparation or TEM analysis eliminated it,
4. the spatial resolution is insufficient to resolve the difference,
5. the spectroscopic detection limit is too low to resolve a difference.

As mentioned above, it was proposed by Hansen *et al.* that the devices rely on migration of oxygen ions and/or accumulation of interfacial electronic defects in the Schottky barrier. While particularly the latter would not manifest in the elemental distribution, it might be possible to visualize these defects via EELS. Aside the Nb oxide layers, however, the Al oxide tunnel barrier is of course of high interest. Figure 4.13 displays the O-K edge of the AlO_x layer of the first generation DBM. The edge of all three samples looks qualitatively the same. About 6 eV before the main absorption edge a small pre-peak can be seen. Both features have been fitted, for the pre-peak a Gaussian was chosen, the main edge has been fit with a Pearson IV peak to account for its inherent background. Such a pre-peak has been discussed in literature before and several origins of the pre-peak are possible:

1. Electron beam damage to hydroxide inclusions.[45]
2. Electron beam damage by repulsion of small positive ions.[46]
3. Influence by empty 3d or 4d orbitals of neighbouring species.[47]

The first two possibilities are notably strongly time dependent, however no evolution of the feature over time has ever been observed. It is known that oxides generally suffer from intense electron irradiation through these and other processes, such as the Knotek-Feibelman mechanism[48], however, these processes are accompanied by a local change of morphology, which has never been observed during investigations. Lastly, the third possible origin, i.e. the charge transfer of AlO_x to neighbouring metal species, in case towards empty 4d orbitals of Nb can also be excluded as the M_{45} and M_{23} edge was not observed in spectra where the pre-peak has been observed. These spectral features were otherwise clearly visible where Nb was present.

As these possibilities have been ruled out, the implication is that the observed feature is likely intrinsic to the analyzed samples. Nigo *et al.* observed a similar O-K pre-peak in AlO_x in their study [49] and concluded that oxygen vacancies were the reason for this feature. According to the molecular orbital model by Johnson and Pepper [50] and theoretical calculations [51]–[53] on the same topic, the electronic structure of alumina is well explored. In fully stoichiometric alumina, O(2p) orbitals form bonds with Al(3s) orbitals. However, as soon as there are oxygen vacancies, they cause unfilled Al(3s) orbitals to localize and shift to higher energies, as compared to the filled Al(3s) orbitals of stoichiometric Al_2O_3 . The increase in energy by about 8 to 10 eV is high enough to lift them above the Fermi energy but small enough such that these states are still below the conduction band. Accordingly, these localized Al 3s states are unfilled and not energetically equivalent to other states. This

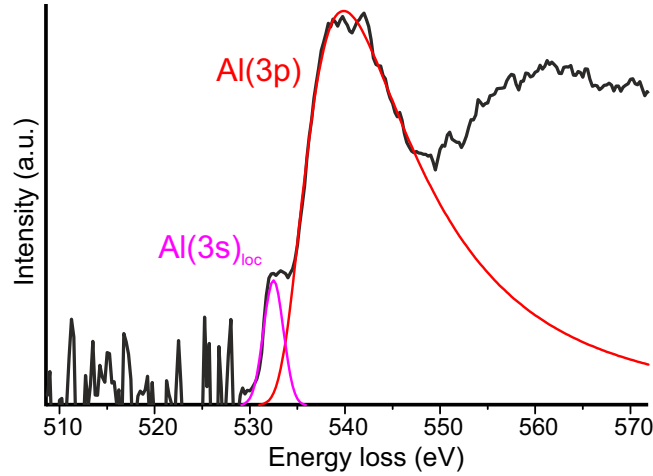


FIGURE 4.13: O-K spectrum of AlO_x of Nb-1-sw-LRS. Pre-peak and main edge have been fitted with a Gaussian and a Pearson IV peak respectively.

coincidence makes them visible via EELS as it uncovers all transition of core electrons to unfilled states.

The intrinsic presence of oxygen vacancies in AlO_x implies a slight non-stoichiometry of the oxide and - as Nigo *et al.* pointed out - potentially even a significant increase in electrical conductivity. In order to better assess the effect of oxygen vacancies, an attempt to quantify them shall be established. The molecular orbital model by Johnson and Pepper [50] establishes that the free states that are closest to the Fermi energy belong to the threefold-degenerate $\text{Al}(3p)$ orbital. These are also the part of the LDOS making up the main absorption edge observed in EELS as they are energetically lowest unfilled states. The valence band on the other hand is made up from non-bound $\text{O}(2p)$ and bound $\text{O}(2p)\text{-Al}(3s)$ states the latter of which form the localized $\text{Al}(3s)$ pre-peak in the O-K edge if not saturated with oxygen. If the transition probability of $\text{O}(1s)$ electrons into $\text{Al}(3p)$ or localized $\text{Al}(3s)$ is effectively equal then the integrated EELS intensities are a direct measure of the number of free states. As amorphous alumina retains some of its local structure and on average every oxygen ion forms a tetrahedron of bonds to four aluminum ions, every vacancy causes four localized $\text{Al}(3s)$ states. Taking into consideration all these factors the concentration of vacancies is given as

$$\frac{3}{4} \cdot \frac{N_{\text{Al}(3s)_{\text{loc}}}}{N_{\text{Al}(3p)}} = \frac{1}{4} \cdot \frac{N_{\text{Al}(3s)_{\text{loc}}}}{N_{\text{Al}(3s)}} = c_{\text{vac}}.$$

Assuming that there is also a number of octahedrally coordinated oxygen this fraction would decrease by a factor of $\frac{2}{3}$. As apparent from Figure 4.13, the experimentally determined quantity is the intensity ratio of $\text{Al}(3s)_{\text{loc}}$ to $\text{Al}(3p)$. Over all first generation samples, the vacancy concentration varies between 1.7 and 3.4 % according to the above equation. It should be noted, however, that this is only an

estimate and no literature to confirm this kind of quantification was found. Potential error sources are a missing factorization of scattering probability into $\text{Al}(3s)_{\text{loc}}$ and $\text{Al}(3p)$, respectively. Given that the oxide is amorphous no large influence from anisotropic scattering probabilities are expected. Both sets of states are completely empty so neither Coulomb nor spin repulsion should have an effect. Furthermore, as the states are energetically extremely close no drastic influence from the exponentially decaying probability is likely but the calculated concentrations are considered upper limits.

As briefly discussed in chapter 3 the dipole selection rule for electronic transition states that g - g and u - u transitions are forbidden; however, in octahedral molecules and complexes this selection rule is weakened by a mechanism introduced by van Vleck.[54] As he points out, the dipole selection rule can be circumvented when a g parity wave function receives u parity contributions due to lattice vibrations. This effect has been discussed by van Vleck for f - f transitions in rare earth metals, which is of course significantly different from the transition in question here. However, as discussed by Fromme [55] the van Vleck mechanism also occurs in other nominally forbidden transition, proving that the dipole rule is not irrevocably true. The leeway for atomic vibrations is higher in amorphous solids compared to crystalline lattices and the momentum input by the microscope's electron-beam is considerable, therefore the proposed mechanism does not seem impossible. The fact that the transitions indeed occur with an unknown transition probability is an additional challenge but still leaves them semi-quantifiable and therefore a comparison between the samples is possible.

The only quantifiable difference found between LRS and HRS was after all a difference in the vacancy concentration of the tunnel barrier which was lower for the HRS sample and slightly higher for the two LRS samples as summarized in Table 4.2. Experiments in the responsible subproject showed that the SB likely is responsible for memristive switching; this was found out by preparing devices with a mutually exclusive Schottky and tunnel barrier, respectively. In these samples only the SB-containing samples showed memristive switching. However, this still leaves the possibility of the interface between Schottky and tunnel barrier being governing for the memristive effect and therefore the tunnel barrier vacancy concentration might be an indicator for defects in the Schottky barrier or at the interface. From the in-

TABLE 4.2: Concentration of oxygen vacancies in first generation DBMs.

Sample	c_{vac} (%)
Nb-1-sw-LRS	3.2
Nb-1-sw-HRS	1.7
Nb-1b-sw-LRS	3.4

sights of the investigations described in this chapter the second generation of DBMs was designed and fabricated, which will be analyzed in the following section. One main intention of the second generation was to suppress oxidation of the back electrode.

4.3 Second generation DBM

After evaluating the results from the first generation of DBM an attempt to maintain their function while bringing it closer the originally envisaged design was undertaken. Specifically this meant trying to avoid the BE oxidation, reduce the surface roughness and get rid of the defects in the tunnel barrier. As the reasonable speculation posed - based on the previously presented results - was that reactive sputtering of the SB caused through oxidation of the Al layer as well as oxidation of BE three different approaches were followed to avoid this oxidation:

1. The sputtering parameters were adjusted as to increase the distance of the substrate to the reactive plasma
2. Nb metal was deposited by sputtering and subsequently oxidized by anodic oxidation.
3. Nb metal was deposited by sputtering and subsequently oxidized by thermal oxidation.

Furthermore, in an attempt to bring these devices towards CMOS compatibility, the Nb oxide based Schottky barrier has been replaced with Hf oxide in one series of devices. Hf oxide was also deposited by reactive sputtering similar to Nb oxide and for this fabrication, too, the geometry has been adjusted according to the previous findings. After adjusting the sputtering geometry, however, a characteristic non-linear dependence of device resistance with respect to distance from the center of the wafer was found. Devices close to the center of the device have a low electrical resistance and show resistive switching similar to first generation devices as shown in Figure 2.1. Devices closer to the sputter trench of the target showed a higher device resistance and did not exhibit resistive switching.

The aim of the investigations was therefore to find out whether

- fabrication was reproducible,
- the Hf oxide based devices had the similar desired layer sequence and oxidation state of Hf,
- anodic and thermal oxidation were passable techniques to deposit Nb oxide.

During introductory experiments HR micrographs of the devices were acquired. Representative images are presented in Figure 4.14. None of the samples showed crystalline phases besides the two metal electrodes. Accordingly, spatially resolved elemental imaging by EELS and EDX remained the option of choice to analyze these samples. The combined layer thickness of the Schottky and tunnel barrier is larger

for the switching samples as compared to the non-switching samples. This comes as no surprise, as the non-switching samples are extracted from outskirts area of the wafer containing the devices. The sputter deposition rate is lower than right in the center, where the switching devices have been taken from. Both switching samples also have in common that they contain a peculiar contrast variation in the middle of the layer. A thin region of about 1 nm thickness appear brighter than the rest of the amorphous layer.

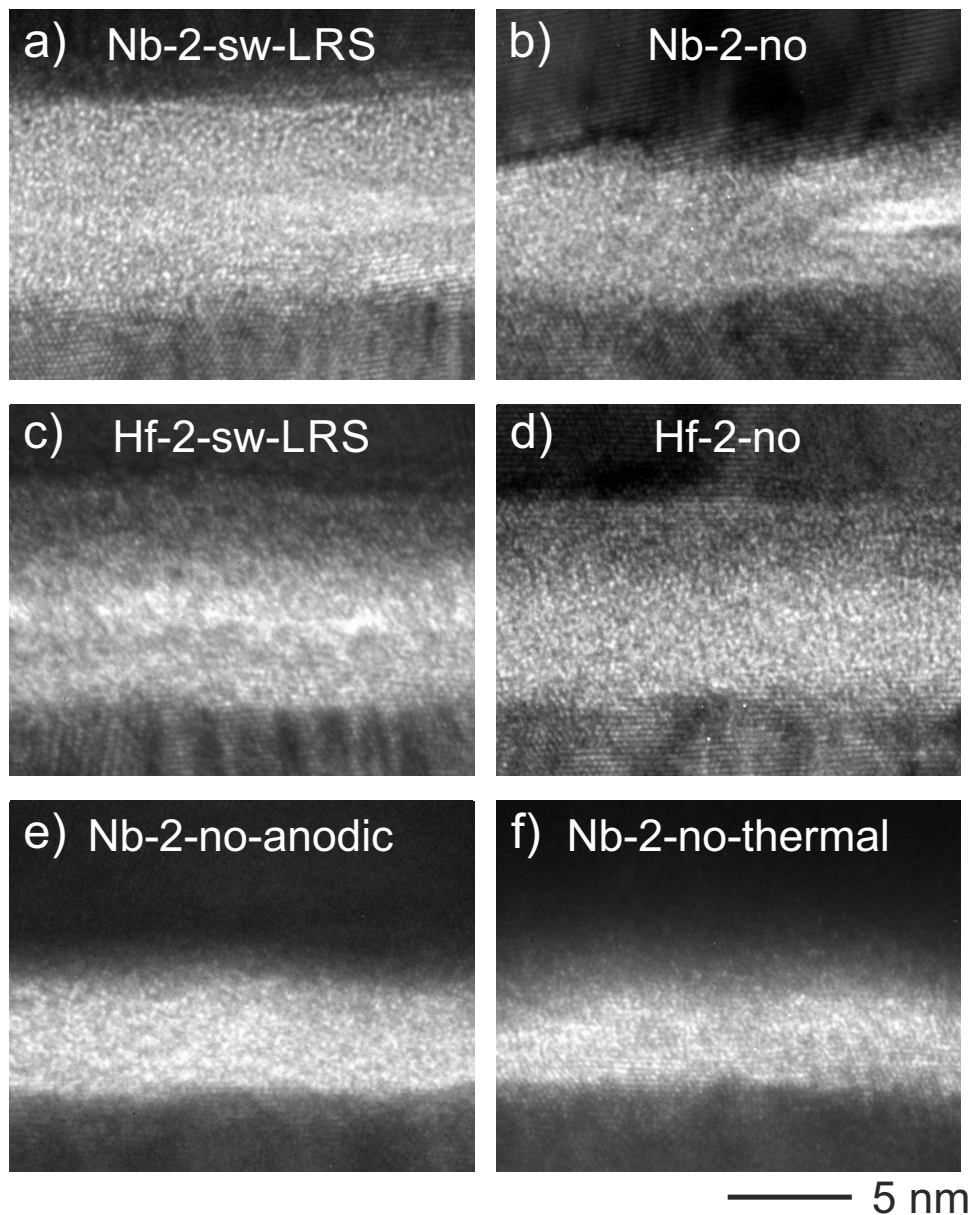


FIGURE 4.14: High resolution micrographs of second generation DBMs. The crystallinity of both the top and bottom electrode is evident, the layer in between is entirely amorphous. HR contrast does not allow to clearly identify the difference between the Schottky and tunnel barrier. Both switching samples (Nb-2-sw-LRS and Hf-2-sw-LRS) exhibit a bright contrast right in the middle of the amorphous layer.

Spatial elemental distribution

Analogous to the first generation DBM, the first step was to see if there were any peculiarities in the spatial distribution of elements, i.e. if the deposition had worked as intended. Figures 4.15 to 4.22 show STEM-HAADF images of the DBM alongside EDX (Al, Au, Hf) and EELS maps (O, Nb) of the constituting elements. In the HfO_x based samples Nb was also mapped by EDX. As no Nb oxide was present in these samples the EELS mapping of the Nb edge was foregone.

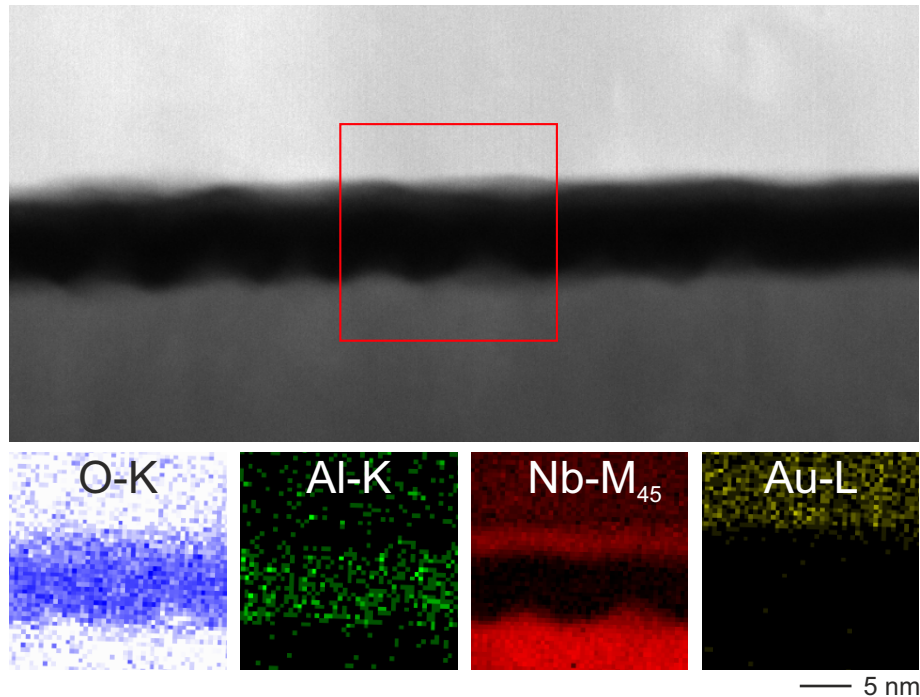


FIGURE 4.15: Spatial elemental distribution of Nb-2-sw-LRS.

The results depicted in Figure 4.15 are extracted from the direct successor of the first generation DBM devices, the only difference being the adjusted geometry during fabrication. These devices qualitatively show the same switching behavior as the first generation DBMs. Unfortunately the investigations on these devices suffered from poor overall intensity. At first glance the absence of BE oxidation is apparent by the lack of overlap between O-K and Nb-M₄₅ signal. The surface roughness observed at the Nb-Al interface persists, it seems therefore safe to assume that the previously observed oxidation of the back electrode and the surface roughness are not causally linked in any way. Other than in previous investigations a peculiar feature in the Al layer was observed. In the middle of this layer there is a distinct dip in intensity indicating a lower Al concentration. This decrease in signal intensity is not directly apparent from the Al-K map, however when the signal is integrated along the layer the intensity profile displayed in Figure 4.16 reveals this feature. Oddly, the O signal does not decrease in this region, indicating an Al depleted AlO_x region. In this exact region the O-K edge of AlO_x displays a strong pre-peak; its origin and possible interpretation will be further discussed in the following section opening up

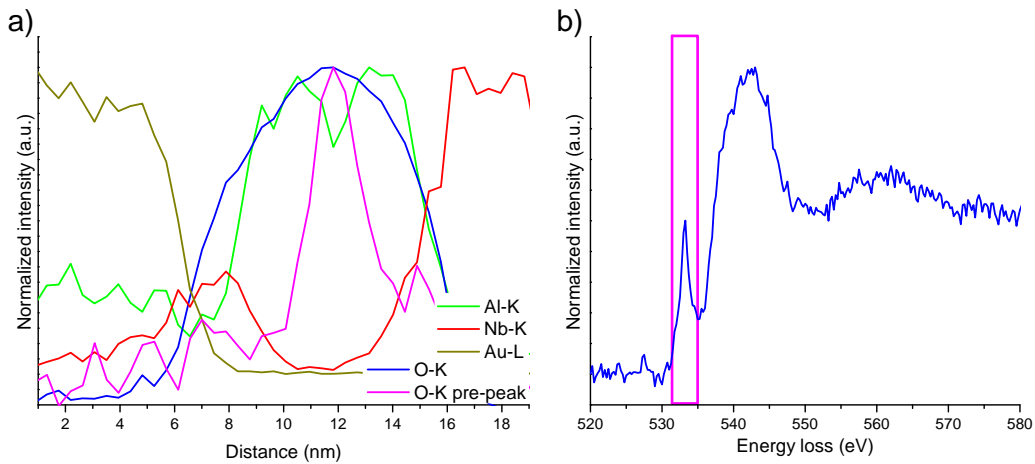


FIGURE 4.16: Intensity distribution of elements across the layers of Nb-2-sw-LRS and O-K pre-peak observed in the middle of the AlO_x layer. a) Intensity distribution generated by integrating the maps displayed in Figure 4.15 along the layers. Magenta line represents O-K pre-peak displayed in the spectrum in b). b) EEL spectrum of the O-K edge extracted from the middle of the AlO_x layer. A pronounced pre-peak is visible at around 533 eV (magenta box).

a possible explanation for the Al depletion. This is also congruent with the high resolution image presented in Figure 4.14; the Al depleted region seems to be congruent with the region of contrast variation the HR micrograph.

Figure 4.17 displays the spatial elemental distribution as well as a STEM-HAADF image of sample Nb-2-no fabricated on the same wafer, i.e. under identical conditions, except not being extracted from the center of the wafer but instead farther outside. This device did not show any memristive behavior and considerably higher device resistance. Initially, the results are congruent with the previously presented sample, besides each of the layers being around 15 % thinner. A pre-peak similar to one observed in Nb-2-sw-LRS has been observed occasionally, but not evenly along the AlO_x , and only in certain areas within the layer. Figure 4.18 displays the lateral distribution of the O-K pre-peak within the oxide layer of this sample. Interestingly, the pre-peak occurs only in isolated positions and is located closer to the SB instead of the middle of the Al oxide tunnel barrier. This stands in strong opposition to the results of Nb-2-sw-LRS where the pre-peak is evenly distributed *along* the Al oxide layer and confined to the middle of it. Also, unlike Nb-2-sw-LRS, no areas of contrast variation in high resolution contrast have been observed within the AlO_x layer.

Hf oxide based devices showed two distinctly different areas in the investigations. The first observed layer sequence is displayed in Figure 4.19. A pronounced gap in the middle of the AlO_x seems to have formed reminiscent of delamination. Unlike the previously documented reduction Al signal in the Nb-2-sw-LRS sample (cf. Figure 4.16) it is accompanied by a comparable lack of oxygen intensity in the EDX map. Intuitively, it would seem reasonable that a similar pre-peak is to be observed in this area, but it is only present highly localized analogous to what has been

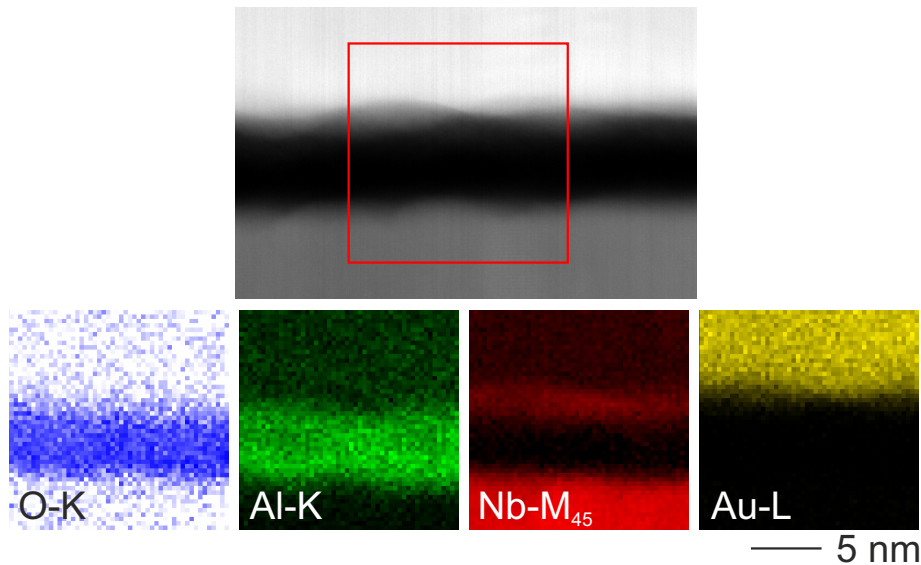


FIGURE 4.17: Spatial elemental distribution of Nb-2-no.

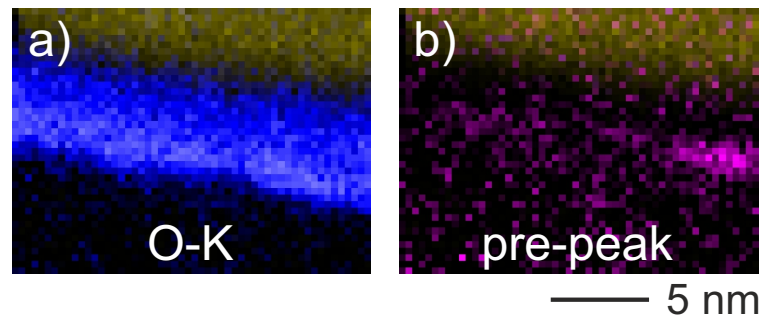


FIGURE 4.18: Lateral distribution of the O-K pre-peak in Nb-2-no. a) The O-K (blue) and Au (yellow) intensity map as reference. b) The pre-peak (magenta) intensity map showing the strong localization. Note that the pre-peak is located much closer to the SB but is not distributed uniformly throughout the AlO_x layer.

shown in Figure 4.18 for sample Nb-2-no. What is more, the high resolution micrograph shows a similarly distinctive feature with an area of brighter contrast in the middle layer.

In the second observed result no such delamination can be observed. Figure 4.20 shows the transition from a delamination region to a compact layer sequence. Both regions alike show complete overlap of the Al and O signal, i.e. no metallic Al was observed, it is completely oxidized as in the previous DBM generation.

Next to Hf-2-sw-LRS, a non-switching sample has been analyzed and is depicted in Figure 4.21. Unlike the other samples, this was the only one solely analyzed on the FEI Tecnai microscope, which lacks stability and EDX sensitivity to analyze such thin layers in more detail. Therefore, only a linescan is available from this sample and no elemental mapping. Nonetheless, qualitatively the result show the expected outcome similar to the results displayed in Figure 4.20, i.e. no delamination and no dip in intensity of either the Al or O signal.

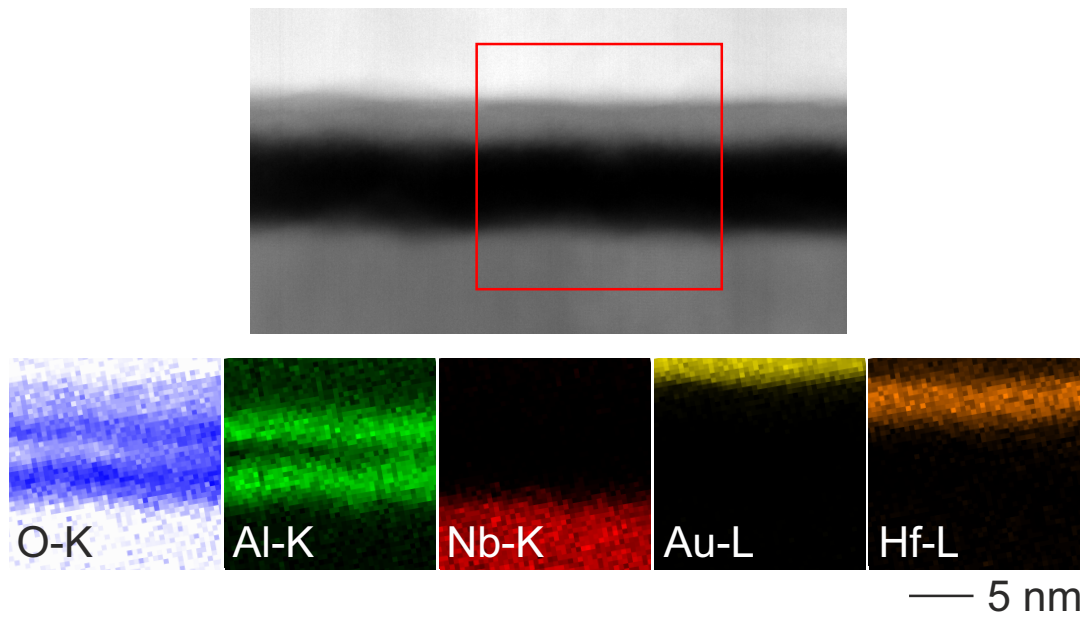


FIGURE 4.19: Spatial elemental distribution of Hf-2-sw-LRS with a localized pre-peak at the very top and seemingly delamination in the middle of the Al layer.

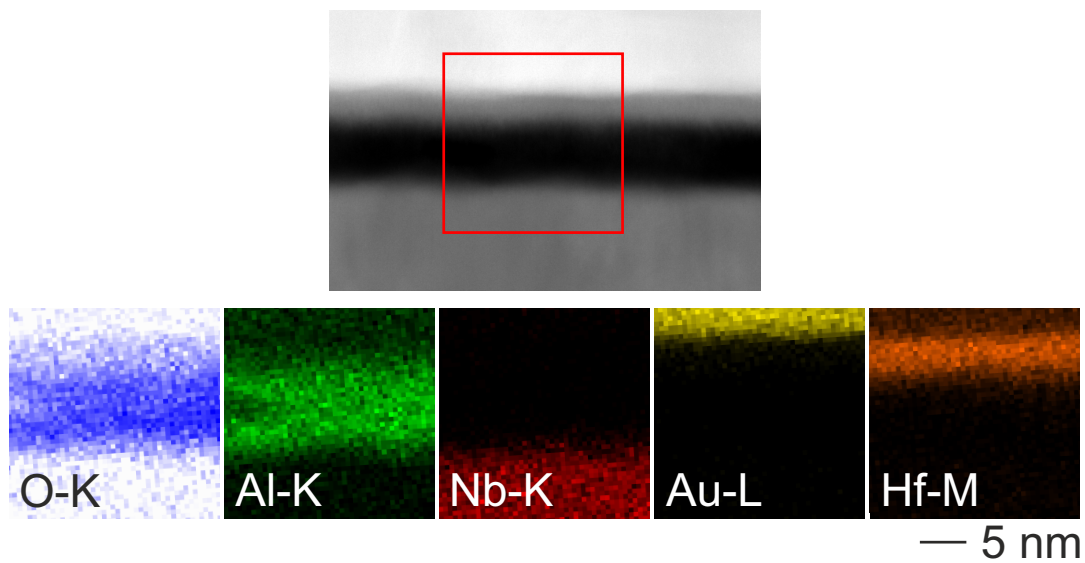


FIGURE 4.20: Spatial elemental distribution of Hf-2-sw-LRS with no delamination.

Lastly, samples from two fabrication methods were analyzed where the deposition of the Nb oxide Schottky barrier is not based on reactive sputtering. Specifically, in these samples the Schottky barrier was deposited by sputtering Nb metal on top of the tunnel barrier and subsequently oxidizing it either anodically (Figure 4.22) or thermally (Figure 4.24). Devices from both fabrication methods, however, show no memristive switching.

The anodically oxidized sample displays similar dip in Al signal in the middle

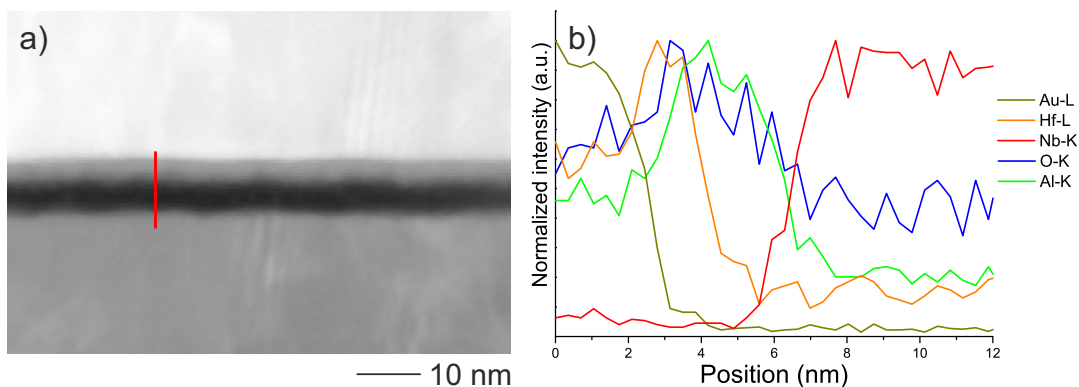


FIGURE 4.21: Spatial elemental distribution of Hf-2-no. a) STEM-HAADF micrograph depicting the individual layers. b) STEM-EDX linescan over the layers. No elemental mapping could be recorded of this sample.

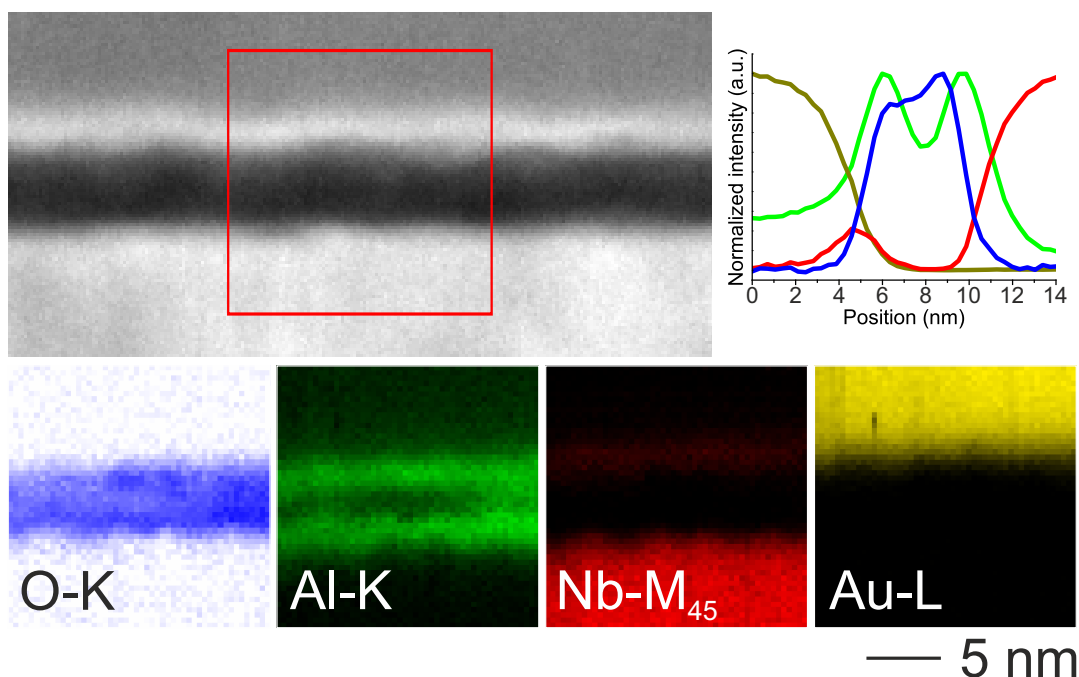


FIGURE 4.22: Spatial elemental distribution of Nb-2-no-anodic. Similar to the sample Hf-2-sw-LRS the Al intensity shows a decreased intensity in the middle of the layer, the O intensity does not follow suit, as clearly visible in the integrated EDX intensities in the top right.

of the Al layer as the Hf-based sample does in some regions. While this generally resembles the results from Nb-2-sw-LRS and Hf-2-sw-LRS (cf. Figures 4.16 and 4.19) which exhibited a similar dip in Al intensity, Nb-2-no-anodic neither exhibits a strongly localized O-K pre-peak in the region of lower Al signal intensity (like Nb-2-sw-LRS), nor does it exhibit an accompanying dip in O-K signal intensity reminiscent of delamination (like Hf-2-sw-LRS). The O-K signal is indeed slightly increased towards the interface with the bottom electrode, but in the middle of the AlO_x layer where the Al intensity decreases, there is no pronounced decrease in O-K intensity. To highlight this, the maps displayed in Figure 4.22 have been integrated along the

layers to create a quasi-line scan which is displayed in the top right.

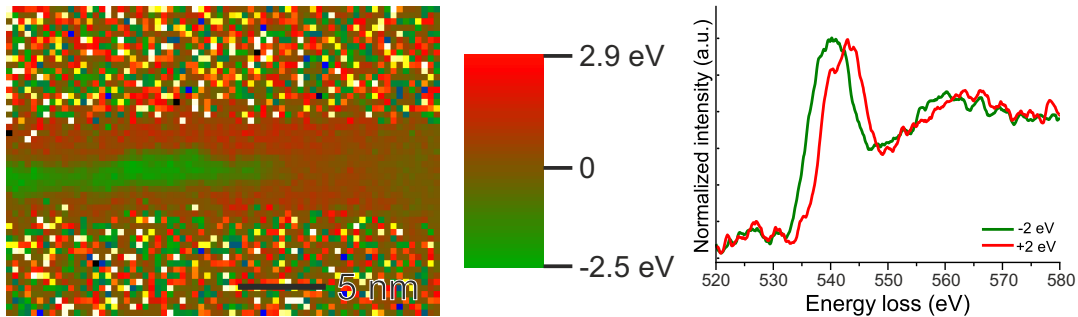


FIGURE 4.23: Spatially resolved energy shift of the O-K edge (left) congruent to the area presented in Figure 4.22 and two example spectra showing the relative shift of ± 2 eV respectively. Negative and positive refer to the spectral shift relative to the reference area on the right of the image, where no decrease in Al signal was observed in Figure 4.22. The red and green area in the middle represents the oxide region, the strongly pixelated multi-colored regions above and below are regions where no oxygen is present, such that the fitting algorithm is not able to determine a beam shift and yields somewhat random results. A negative energy shift can be explained by decreased coulombic attraction towards the ion core of the electron excited from O 1s to an empty state.

Interestingly, though, the region in which the Al intensity decreases is perfectly superimposable with a slight shift of the O-K absorption edge towards lower energies (see also the green area in Figure 4.23). This makes sense in that if that region is indeed Al depleted and thus has formally a more negative charge density there is less coulombic attraction towards the ion core for the O 1s electron being excited in this process. The energy shift towards higher energies in the red area which mainly coincides with the area where the AlO_x layer neighbors the Nb Schottky barrier is caused by the interaction of O(2p) with the (4d) orbitals of Nb. The HR micrograph on the other hand did not display any features in within the amorphous layer, implying that the Al depletion does not manifest itself with a morphological change. Besides these striking features, the elemental maps and line scan also highlight the surprisingly low O-K intensity in the Schottky barrier. The oxidation of Nb in the Schottky barrier will be analyzed in detail in the following section. Importantly, though, in these samples it was possible for the first time to evidently observe metallic Al close to the bottom electrode, apparent from the lack of complete overlap of the O-K and Al-K maps towards the bottom electrode. There clearly is a part of the Al layer that contains no oxygen, also highlighted by the previously mentioned line scan.

Similar to the anodically oxidized sample the thermally oxidized sample (cf. Figure 4.24) also shows metallic Al towards the bottom electrode. A detailed spectral analysis in the following section will reveal if there is a slight oxidation in this area.

Spectral analysis, ELNES fingerprinting

Unlike the first generation of devices, the differences between single second generation devices observed in morphology and elemental distribution are significant

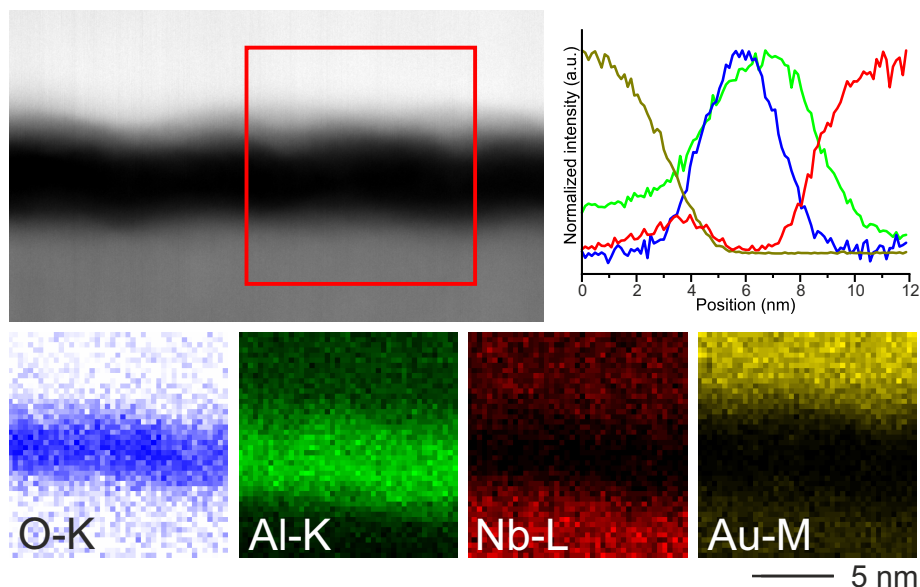


FIGURE 4.24: Spatial elemental distribution of Nb-2-no-thermal. Similar to the sample Nb-2-no-anodic the EDX intensities were integrated along the layer to create a quasi linescan, see top right.

and thus no generalization for the devices can be drawn. Figure 4.25 shows the O-K edges extracted from the AlO_x layer of all second generation DBMs along with three references for amorphous, α - and γ -alumina. A reference for ϑ -alumina was omitted, as it closely resembles that of γ -alumina and these phase are thus virtually indistinguishable through their EEL spectra.[56] Sample Hf-2-no presents an outlier, in that especially the onset flank of the edge looks different from the other edges. It should be noted, that this is the only edge recorded on the FEI Tecnai microscope in Kiel under different experimental conditions and with a nominally much worse energy resolution. As already presented in Figure 4.16, there are also regions in these samples where a pronounced pre-peak exists at around 9 eV prior to the main absorption peak. Interestingly, when the pre-peak is particularly pronounced the entire shape of the O-K edges changes. Figure 4.26 spectra containing this pre-peak; the shown spectra represent the strongest observed pre-peak in the respective sample.

A similar analysis of the Al-L₂₃ edge extracted from the AlO_x layer is also possible, but much more complex because for once the Al-L₂₃ edge has a higher number of features to be compared and secondly the signal-to-noise ratio is much worse at such a low energy loss because of the much higher background. Figure 4.27 displays the Al-L₂₃ edge in part a), demonstrating this problem. In an attempt to break the edge down into easily comparable factors, the two main contributors, i.e. the L₃ and L₂ peaks, were fitted with Gaussians as displayed in Figure 4.27 b); the main characteristics of these Gaussian peaks can be easily compared between references and experimental data. These characteristics are amplitude, position and the full width at half maximum (FWHM). Importantly, unlike the other spectra presented for the second generation DBM the Al-L₂₃ spectra possess a calibrated energy axis, as they

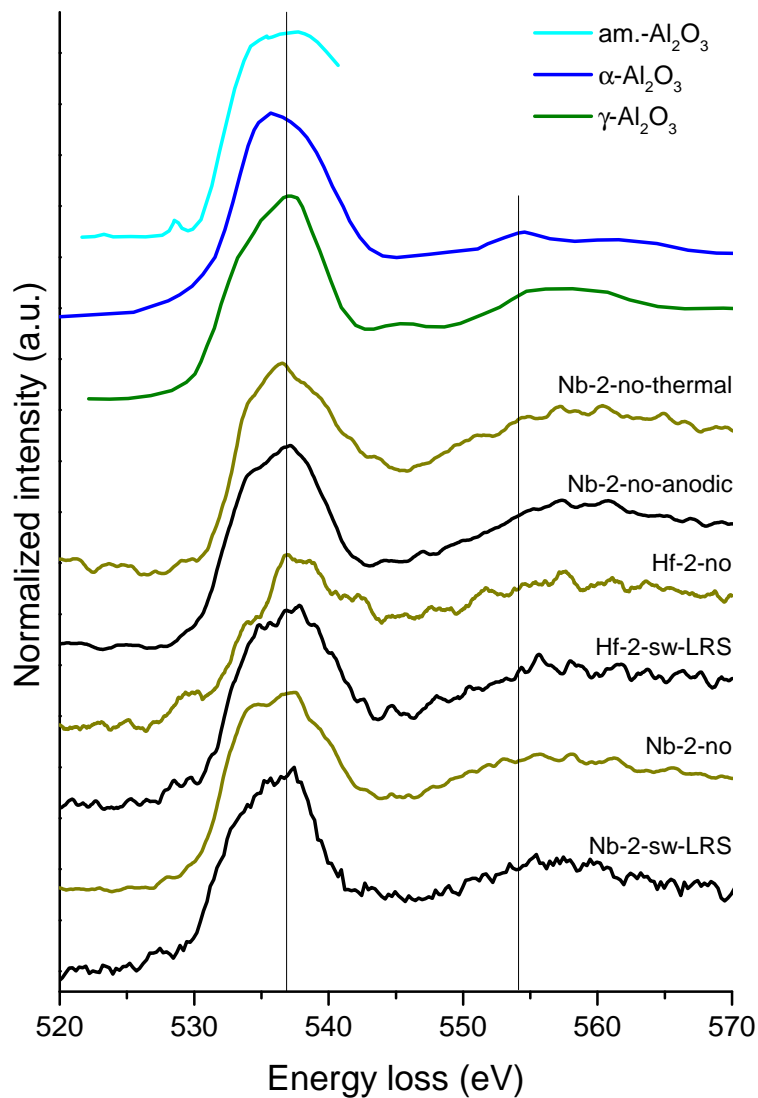


FIGURE 4.25: O-K edge from the AlO_x layer of second generation DBMs and three references at the top. Except for the non-switching Hf-based DBM all experimentally acquired spectra show the tendency that the edges' maxima are skewed to the right, similar to γ -alumina. Reference spectra are taken from [57](α -alumina), [58](amorphous alumina) and [59](γ -alumina)

are such a low energy loss that they have been recorded together with the zero loss peak which was used to align these spectra.

The O-K edge extracted from the Nb oxide Schottky barrier is presented in Figure 4.28. The only spectrum assignable to a reference stems from sample Nb-2-sw-LRS which resembles Nb_2O_5 similar to what has been observed in the first generation of devices. The other spectra are very much untypical for O-K edges of Nb oxide, as these typically contain a sharp onset as evident from the reference spectra recorded by Bach [43]. This is attributed to fact that the other samples likely exhibit an extremely low degree of oxidation within the SB; this is also congruent to the observation made previously, where O-K maps in these samples barely seemed to

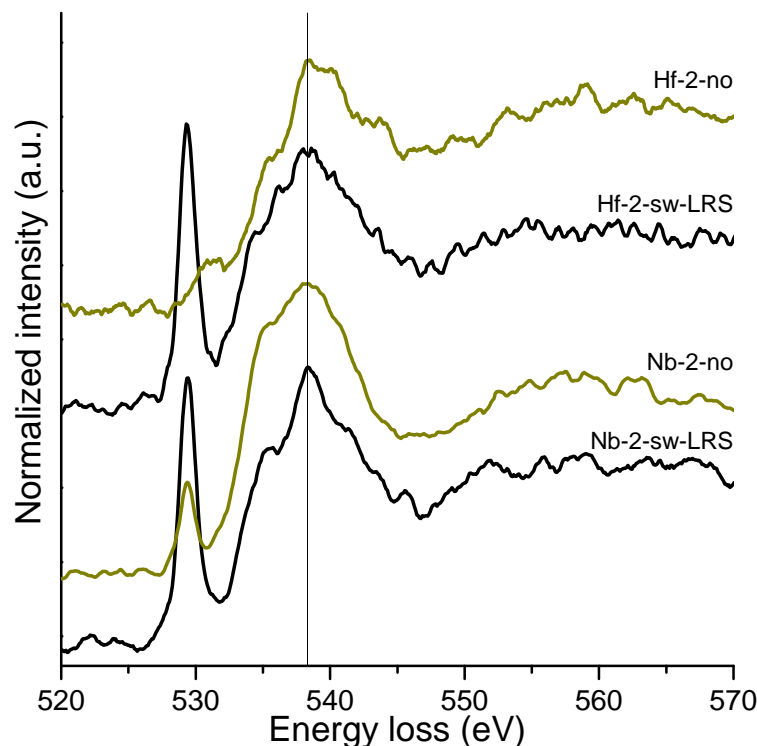


FIGURE 4.26: O-K edge with strong pre-peak from the AlO_x layer of second generation DBMs.

overlap with the Nb signal of the Schottky barrier. Therefore, the conclusion that the thermally and anodically oxidized samples as well as the non-switching reactively sputtered sample did not produce properly oxidized Schottky barriers.

The trend visible in Figure 4.29 that spectra from longer exposure times tend to be shifted to lower energies is judged to be a coincidence. The spectra were recorded chronologically, therefore the shift in the spectra is attributed to a shift of the zero loss peak over time.

4.4 Comparative analysis

Even more important than the mere description of the individual devices is the comparison between them. Spectral features have already superficially compared in the preceding section, besides a more detailed description of these the layer thickness and more will be analyzed in this section. Table 4.3 aims to summarize the results from the individual analyses in a comprehensive form. The main findings so far were the presence or absence of a pre-peak in the tunnel barrier oxide, as well as the layer thicknesses.

Figure 4.30 also shows the elemental distribution of all analyzed devices side by side. When comparing first and second generation devices, the most striking difference is obviously the reduced thickness of the oxide layer; the lack of back electrode oxidation has been discussed previously. Nonetheless, the surface roughness

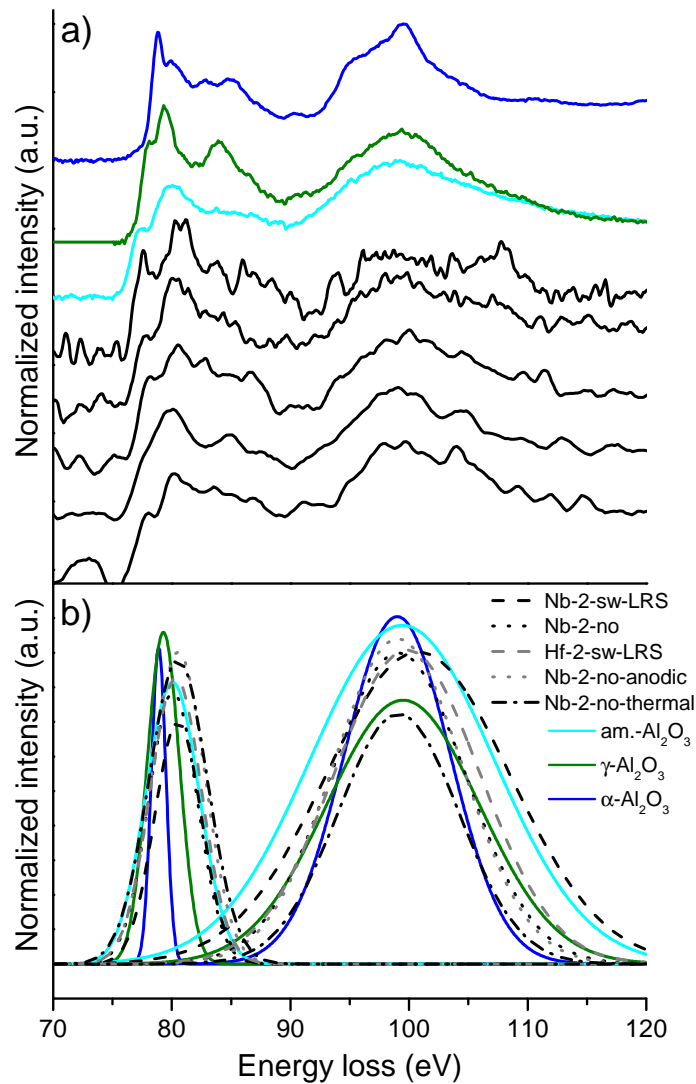


FIGURE 4.27: Al-L₂₃ edge from the AlO_x layer of second generation DBMs. Reference spectra were taken from Reference [56].

between the Nb back electrode and the Al oxide layer is also drastically reduced in the second generation. Since deposition parameters for the back electrode have not been altered from the first to the second generation, this implies that the unintentional "plasma treatment" during reactive deposition of the Nb oxide Schottky barrier might have also induced an alteration - i.e. an increase in surface roughness - of the interface.

While this seems unintuitive at first, particularly why this would not result in an even intermixing of the Nb back electrode and Al from the layer on top, this claim is corroborated when comparing the surface roughness of the first generation with the images taken of the Josephson junction (cf. Figure 4.2). As the latter also shows a low surface roughness comparable to that of the second generation while not being modified by a reactive oxygen plasma it seems plausible that the surface roughness indeed originates from plasma modification. What the mechanism behind increased

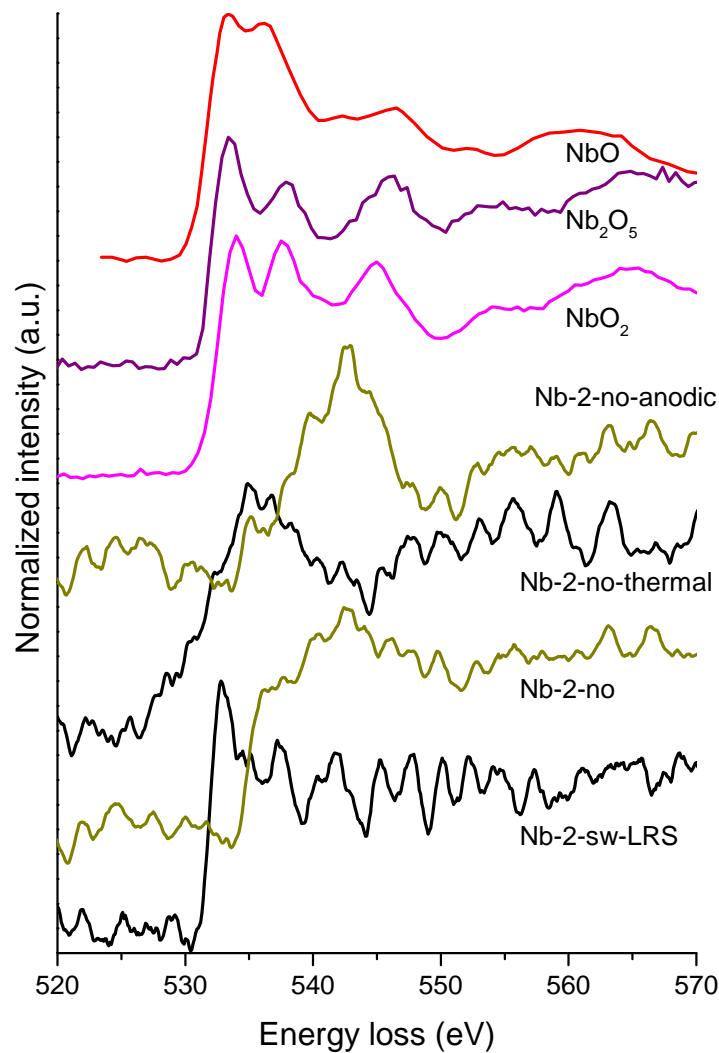


FIGURE 4.28: O-K edge from the NbO_y layer of second generation DBMs. Reference spectra were taken from Reference [43].

surface roughness is can only be speculated about. The bumps and valleys of the interface do not seem to correlate with grain boundaries in the Nb back electrode; the grain size in this layer is approximately between 25 and 30 nm. The surface roughness has a lateral "period" of about 5 nm. Furthermore, the oxidized layers are completely amorphous and therefore do not contain any kind of grain structure. Another possibility is the local fluctuations in energy density of the plasma or peaks in the field strength. Oddly, though, the penetration depth of oxygen is rather constant along the layers and does not vary in conjunction with the surface roughness. If the latter were caused by an uneven oxygen plasma, it would seem reasonable that this is also reflected in an uneven oxidation depth, which is not observed. The variations in the plasma probably occur on much larger length scales than what can be observed by a single TEM sample.

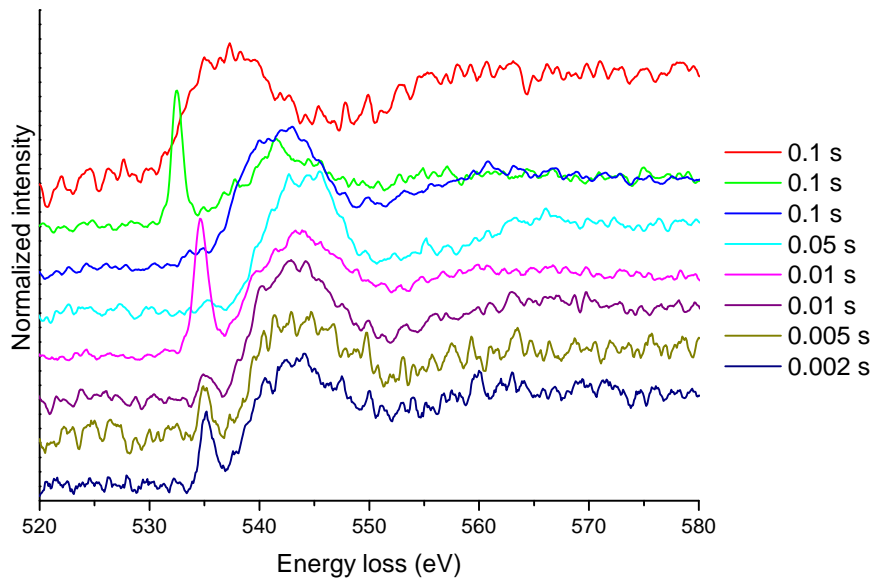


FIGURE 4.29: Exposure time series investigation on the O-K edge of AlO_x . The shortest exposure time producing data with a reasonable noise level is 0.002 s per pixel. Spectra with the same exposure time have been recorded at different locations. No correlation between exposure time and pre-peak intensity was found.

The thicknesses of the layers depicted in 4.30 have been determined in multiple regions of the sample, not all of which are depicted in this work. The results are shown in Figure 4.31. The error bars represent both the spatial resolution of the investigations as well as the standard deviation of the determined thicknesses. The increased oxide layer thickness observed in sample Nb-1-sw-LRS (in total about 12 nm, as compared to less than 10 nm in other first generation samples) is mainly due to a more pronounced oxidation of the back electrode, the actual SB and TB thickness is very much similar to those of other samples. Interestingly, the thickness of the Nb oxide SB is more or less constant with a value of about 2.1 nm. The Al oxide tunnel barrier's thickness on the other hand fluctuates significantly. The two HfO_x -based devices are the exemptions, the SB is at least 1 nm thicker compared to the NbO_y -based devices. The difference between the two HfO_x -based devices is due to the previously mentioned position on the wafer. Hf-2-sw-LRS was extracted from the center of the wafer, where the deposition rate is higher and therefore layers are thicker, while Hf-2-no is extracted from an off-center position at the rim of the wafer. At this position the deposition rate is lower and therefore layers are thinner.

Furthermore, the spectral features of the Al – L_{23} edge were compared in detail as the ELNES fingerprinting depicted in Figure 4.27 was inconclusive. Figure 4.32 shows the systematic comparison of spectral features. The FWHM map as well as the centers of these peaks suggest that generally closer to amorphous alumina (cyan)

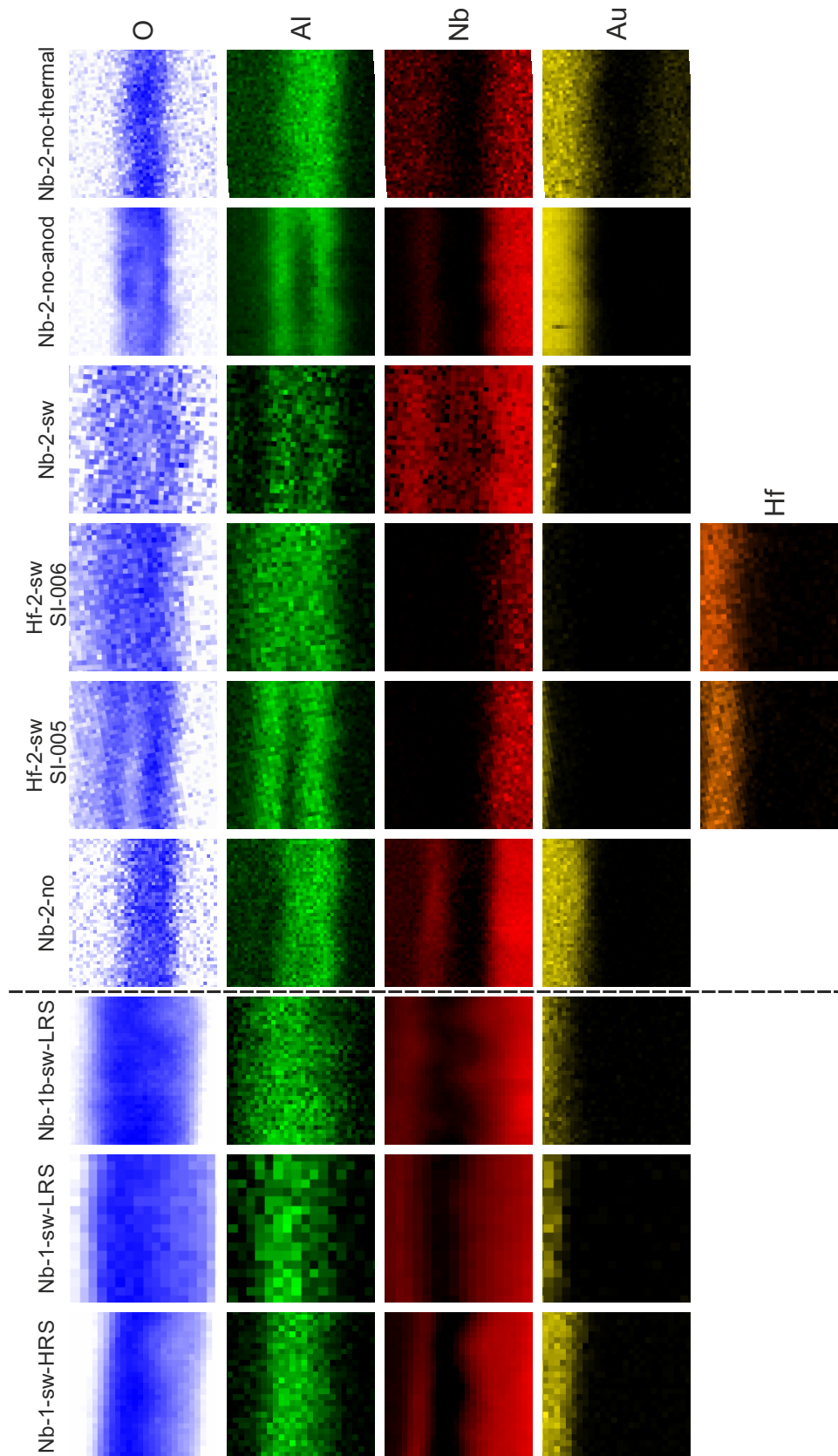


FIGURE 4.30: Comparison of the spatial elemental distribution between all analyzed devices from the first generation (below dashed line) and the second generation (above dashed line). Sample Hf-2-no has not been analyzed by STEM-EDX mapping.

TABLE 4.3: Overview table of DBM properties.

Sample	Pre-peak		Layer thickness	
	Shift (eV)	Confinement	SB (nm)	TB (nm)
Nb-1-sw-LRS	6	continuous	2.1	5.7
Nb-1-sw-HRS	6	continuous	2.0	5.7
Nb-1b-sw-LRS	6	continuous	2.2	6.2
Nb-2-sw-LRS	9	mostly continuous	2.2	6.6
Nb-2-no	9	localized	2.1	5.5
Hf-2-sw-LRS	9	localized	2.7	7.8
Hf-2-no			3.0	4.5
Nb-2-no-anodic			2.1	6.5
Nb-2-no-thermal			2.1	4.8

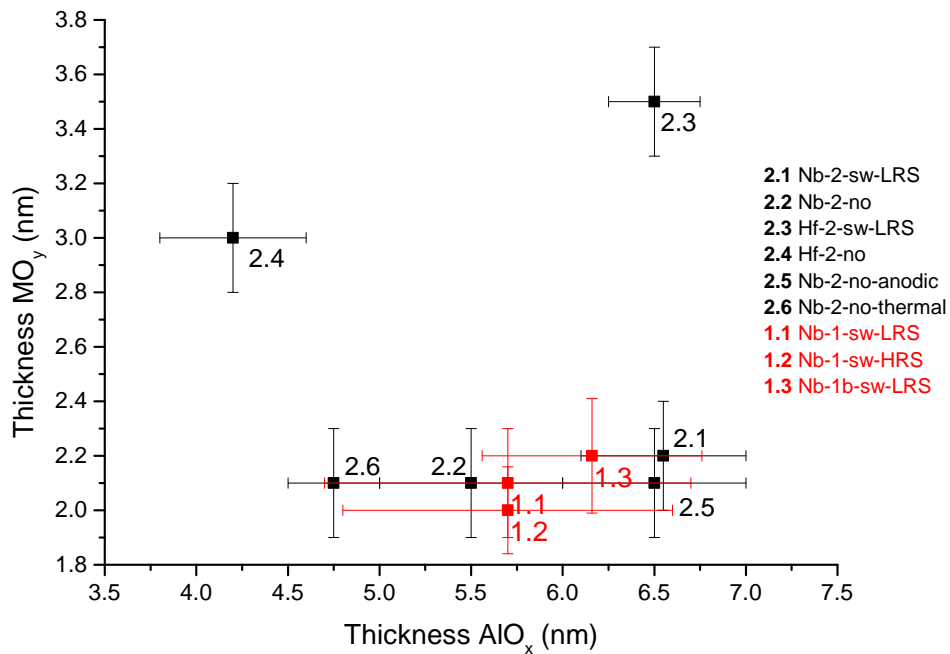


FIGURE 4.31: Comparison of oxide layer thicknesses in DBM devices. Number next to date indicates individual devices, see also the legend. MO_y refers to the Hf or Nb oxide SB, respectively.

than to the other two references. The intensity ratio of L₃ and L₂ peaks shown in Figure 4.32 b) is less significant, the trend suggests that the biggest difference is between samples Nb-2-sw-LRS and Nb-2-no-anodic whose ratios are similar to that of amorphous alumina and γ -alumina, respectively. The O-K edge from the AlO_x region

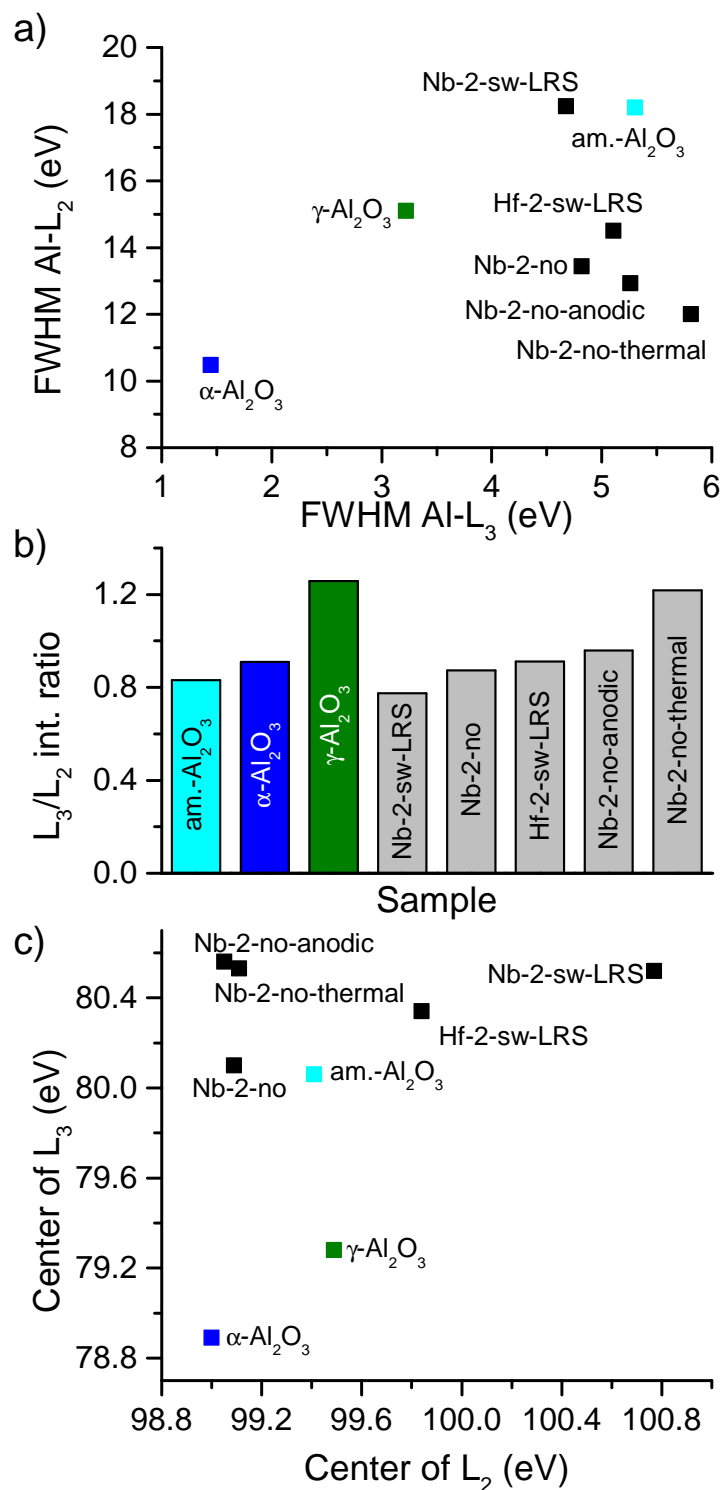


FIGURE 4.32: Analysis of the Al-L₂₃ between second generation DBMs. a) FWHM of the Al-L₂ and L₃ of second generation DBMs and references. b) Intensity ratios of the L₃ and L₂ peaks. c) Centers of the L₃ and L₂ peaks.

previously discussed (cf. Figure 4.25) resembled that of γ -alumina in all samples the most. The inherent difficulty of assigning the Al-L₂₃ edge in a similar fashion is that excited core level is not a singular level as in the O-K edge where the O(1s)

electron is excited. Instead, the Al-L₂₃ edge represents the Al(2p) orbital containing two levels where the total angular momentum j is $\frac{1}{2}$ and $\frac{3}{2}$, respectively. The fact that no pre-peak is observable 9 eV before the L₃ edge can have its reason in two factors; a) the spectra could be recorded at position where there are no defects or b) be due to forbidden transitions from the Al(3p) electrons to the defect state. The former is unlikely but unfortunately cannot be ruled out completely. The Al-L₂₃ at 73 eV energy-loss has not been recorded simultaneously with the O-K edge at 532 eV, which is next to impossible because of the large difference, as discussed before. Therefore, no direct correlation between the Al-L₂₃ and O-K spectra from the very same measurement is possible. However, as presented in the case of Nb-2-sw-LRS, the pre-peak is almost ubiquitously present; "missing" the pre-peak in all measurements is therefore deemed unlikely. The absence due to selection rules is more likely. As laid out in chapter 3, transitions that conserve parity in centrosymmetric molecules and atoms are forbidden; as the excited electrons in the two cases have opposite parity (O(1s) in the O-K edge is of g parity, Al(2p) of the Al-L₂₃ is of u parity) they cannot be excited to the same states. This also implies that the states represented by the pre-peak feature in the O-K edge are of u parity and therefore belong to antisymmetric orbitals. A spin-forbidden transition is not the reason for this, as both original states contain both spin-up and spin-down electrons to circumvent this selection rule. Accordingly, the pre-peak is caused by a partially- or non-filled antisymmetric orbital, such as a heteronuclear antibonding orbital or e.g. a tetrahedral orbital which also lacks an inversion center. As previously established oxygen indeed generally forms a tetrahedron of bonds to four Al atoms. Therefore the absence of an Al atom from this tetrahedral bond would cause a partially filled antisymmetric orbital. As this corresponds to the reduction in Al signal in the EDX maps it can therefore be deduced that the presence of the strong pre-peak is indeed an indicator for Al vacancies. An oxygen vacancy on the other hand would cause a partially filled octahedral bond which is centrosymmetric; a transition from O(1s) to this orbital would be forbidden. This is all under the assumption that the close-range order of alumina is similar to crystalline alumina; all recorded AlO_x O-K spectra without a pre-peak generally resemble that of the γ phase, spectra with a pre-peak show severe deformation of spectral features.

Another possibility for this pre-peak is also the presence of hydroxides as already briefly discussed in the case of first generation DBMs.[60] While the spectral features match well with that of hydroxides (cf. Figure 4.33) they do not evolve over time and apparently are not dose rate dependent as shown in Figure 4.29 which speaks against the hydroxide origin. Furthermore, no plausible explanation for the lateral variation of hydroxide presence was found. If the hydroxide had formed during deposition of the layers there is no reason for local variations of hydroxide presence and neither is there a reason for hydroxide formation after TEM sample preparation with local fluctuations. Unfortunately, this detail remains an open question.

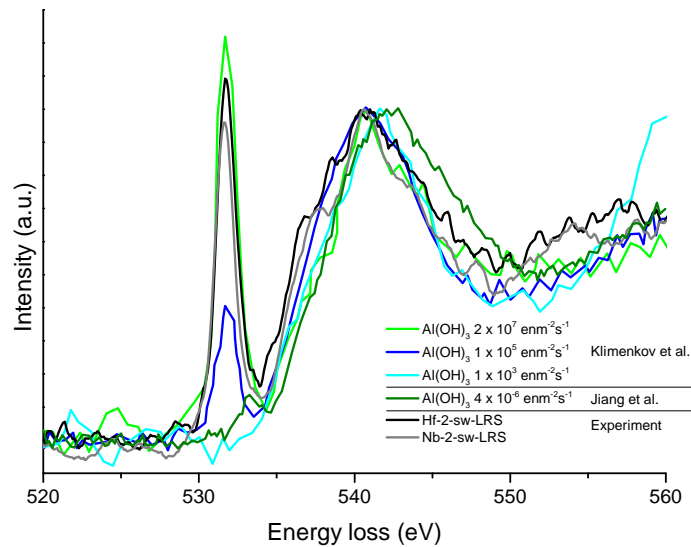


FIGURE 4.33: O-K spectra with a strong pre-peak and various hydroxide references by Klimenkov *et al.*[46] and Jiang *et al.*[45]. The dose rate during recording the experimental data was approximately $10^6 \text{ e} \cdot \text{nm}^{-2}\text{s}^{-1}$ with a dwell time of 0.01 s

In reference to the questions posed at the beginning of the chapter, the findings presented in this chapter were:

- The layer sequence was different from expectations in that no metallic Al was found and in first generation devices the back electrode showed pronounced oxidation.
- The layer thicknesses were determined and while the Nb oxide layer was of uniform thickness, the Al oxide showed variation between 4.5 and 7.0 nm.
- Two different electronic defects have been observed in the O-K spectra of AlO_x . The probable reasons for these defects are the presence of oxygen vacancies in the first generation DBMs and aluminum vacancies or the presence of hydroxides or suboxides in the second generation devices.
- No quantifiable difference between LRS and HRS devices was found.

Chapter 5

Investigations of Nanoparticulate Memristor Prototypes

Unlike the double barrier memristor described in the preceding chapter, the nanoparticulate memristor does not rely on local changes of chemistry or oxidation state. Instead, the distribution of nanoparticles in a dielectric matrix are authoritative for this device and thus this chapter deals with the exact characterization of nanoparticle distribution, density and - in the case of bimetallic particles - also their composition. Accordingly, energy-loss spectroscopy was less central to these investigations, instead conventional imaging techniques were utilized to characterize these devices. The composition of nanoparticles was also of interest; to that end EDX quantification of particles produced under various experimental conditions was applied. All of these investigations were conducted on the FEI Tecnai TEM in Kiel. As future memristive devices of this kind will rely on the 3D distribution of nanoparticles in a matrix with custom tailored gradients tomographic analysis was conducted on the JEOL JEM-2100.

To the effect of producing these nanoparticles a physical vapor deposition (PVD) process based on a Haberland-type gas aggregation source (GAS) was chosen. It is based on magnetron sputtering in a vacuum chamber with an additional aggregation chamber with a higher pressure. The source is described in more detail in the book by Huttel [61]. A specialized target for the GAS has been developed in the subproject "Vertical and horizontal memristive nanocomposite devices without the formation of filaments"[62]. While the details may be read up on the publication by Vahl *et al.*[63] the general idea of the source is to implement a metal wire in the region of the sputter trench of a metal target. Target and thread are made from different metals. The target is placed in the aggregation chamber with a higher pressure than in the rest of the vacuum chamber, where individual atoms aggregate to nanoparticles. The result is the sputtering of two metals, the sputtered atoms aggregate in the chamber and are ejected through an orifice onto the substrate. The composition and particle distribution can be controlled via the sputtering parameters, namely pressure, duration and power. All results displayed in this chapter are recorded on samples produced by Alexander Vahl using this GAS.

As the development and fine-tuning of this novel nanoparticle source required extensive attention, this work mainly deals with prototypes for such nanoparticulate systems and excruciating care was taken to analyse the properties of the gas aggregation source. The sputter targets were created from silver with an inert-metal wire embedded in them. This combination was chosen as Ag is highly active in an electric field - i.e. it ionizes and moves along the field lines - while e.g. gold and platinum remain inert. As described in chapter 2, this combination was chosen such that silver can migrate and change the electrical conductivity of the device while the inert metal serves as an immobile anchor to enable the silver cations to return to their original position instead of being immobilized at the metal cathode.

5.1 Monometallic (Ag, Au) particles on carbon films

Before producing bimetallic particles with the described added-wire target, monometallic particles were produced to validate whether the GAS is working as intended with simple single metal targets. Select results are depicted in Figure 5.1. The overview image suggests that there might be a bimodal size distribution which is confirmed by statistical analysis.(cf. Figure 5.1 b)) Few particles agglomerated but generally the mode sizes of the bimodal distribution are at 2 and 8 nm, respectively. High resolution analysis shows that the larger particles are crystalline; smaller particles have been found to exist in both crystalline and seemingly amorphous states, i.e. no high resolution contrast was visible on a fraction of particles. As EDX analysis showed only Ag signal and diffraction experiments show no other phase but crystalline Ag the particles all originate from the target as intended. The particle depicted in Figure 5.1 c) exhibits a characteristic fivefold twin [64] also nicely recognizable by its fivefold symmetry in the FFT. Interestingly, in contrast to monometallic Ag particles, Au particles show no such bimodal size distribution. Even though the two samples in comparison were produced with the exact same parameters, the outcome is strikingly different. Aside the size distribution, the volume density deposited particle volume per unit area has been calculated. Assuming spherical particles, the values are 167000 and 454000 nm³/μm² for Au and Ag, respectively.¹ The difference in deposition rate is to be expected, as Au (atomic weight $A_r \approx 197u$) and Ag ($A_r \approx 107u$). The magnitude of the difference is surprisingly large, nonetheless. The absence of smaller particles in the Au sample is unintuitive, the kinetic processes inside the GAS are not fully understood though, so that variations between different atomic species are to be expected. One possible explanation is that the higher sputter yield of Ag leads to a larger number of nuclei in the gas phase above the target and therefore also a higher number of particles on the substrate. The low sputter yield of Au on the other hand leads to smaller number of nuclei in the gas phase which in

¹In terms of more graspable units this is equal to a metal film of 0.17 and 0.45 nm thickness, respectively.

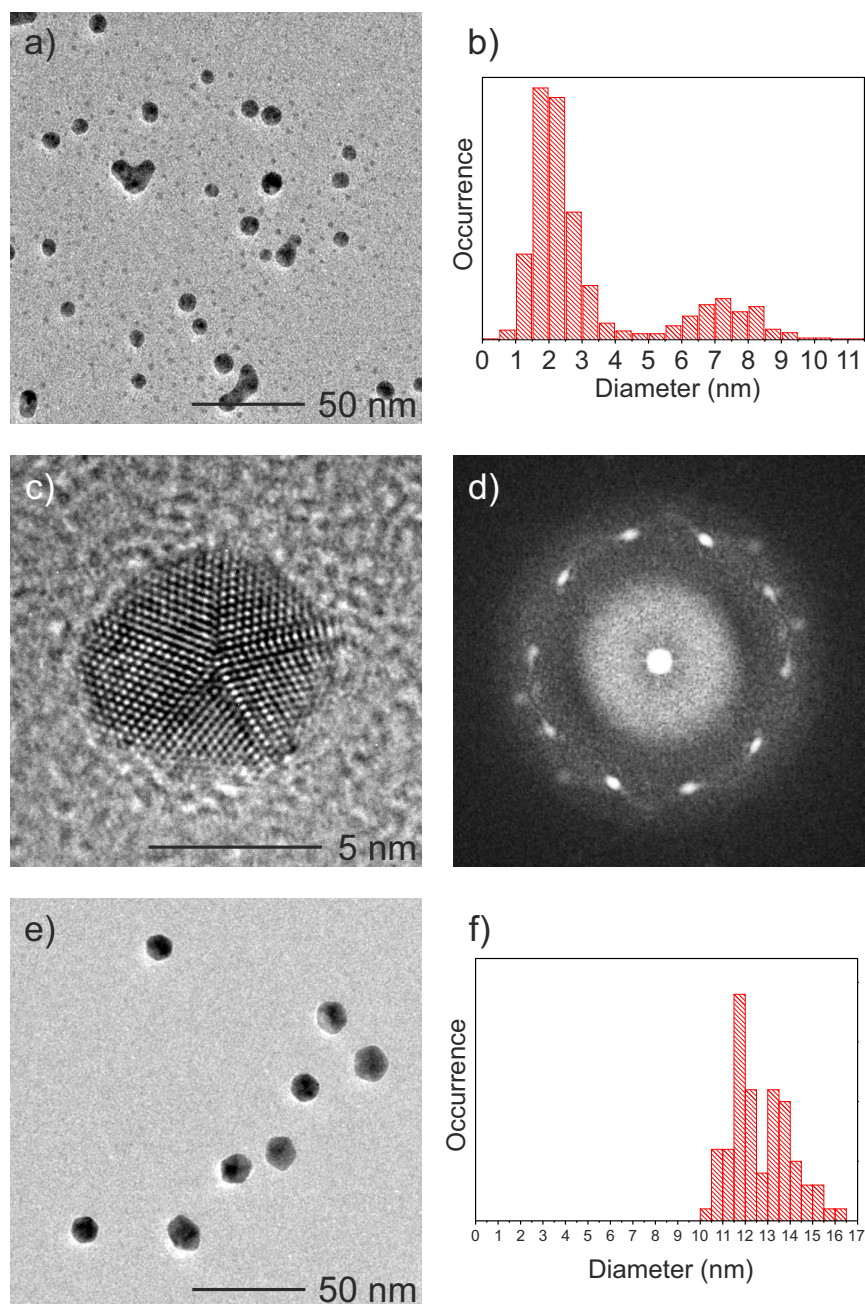


FIGURE 5.1: TEM investigations of monometallic particles on a carbon film. a) Overview image of Ag particles. b) Ag Particle size distribution showing a pronounced bimodal character. c) HRTEM micrograph of a Ag particle with a characteristic fivefold twin. d) FFT of the particle in c) showing a seeming fivefold symmetry. e) Overview image of Au particles. f) Au particle size distribution showing a monomodal character. Sputter parameters for both samples were the same at 40 W, a flow of 48 sccm Ar and a deposition time of 5 s.

turn allows them to grow bigger and thus fewer but larger particles are ejected onto the substrate. This theory has to be developed further and could be explored by producing monometallic particles from even more metals. Copper is a good candidate for this, as it is from the same group as Ag and Au and thus has the same valence electron configuration such that bonding effects can be excluded.

Accordingly, it was concluded that the GAS is working as intended even though the particle formation mechanisms are not fully understood. The bimodal size distribution is surprising and its origin is subject to ongoing investigations. Given that smaller particles are expected to be more mobile, heating the substrate to intermediate temperatures for a limited time frame could allow the smaller particles to agglomerate or merge with the pre-existing larger particles. In a next step the introduction of these particles into a dielectric matrix was investigated.

5.2 Silver particles on and in a Si matrix

Additionally, the results of cosputtering the particles together with a Si matrix were evaluated by TEM to find out how the cosputtering process affects the particles. Specifically, this was accomplished by having two separate sputter targets in the vacuum chamber. One is the aforementioned GAS while the second one deposits the Si matrix. Figure 5.2 displays the results of samples with a constant sputter time of 80 s for Si, and varying subsequent sputter times for Ag nanoparticles between 0.5 and 2 s. In these samples the Ag particles are on the surface of the Si matrix. The sample indicated as 3 s sputter time differs from the others as it was fabricated by depositing 80 s of Si and 1.5 s of nanoparticles two times on top of each other, respectively. All samples show a similar size distribution (cf. Figure 5.2 a)) with a mode particle size between 2 and 7 nm. While the sample with the shortest sputter time (0.5 s) does exhibit the smallest mode particle size (2 nm) the other samples do not follow the correlation of increasing particle size with increasing sputter time. Interestingly, two samples show a second local maximum at 13 nm particle size. Besides the mode size, apparent from part a), the average particle size and number density of particles was analyzed. Oddly, neither of them follows a clear trend. Lastly, the volume density of deposited silver was calculated - again by assuming spherical particles - where a clear trend for samples with sputter times between 0.5 and 2 s is visible. The sample which received two 1.5 s phases of Ag nanoparticles and 80 s of Si matrix was analyzed to have a smaller volume density, which seems unintuitive at first glance.

The volume density of this sample is in all likelihood higher and probably follows the linear trend apparent from the first five samples. Taking into account particle kinetics a reason for this could be the doubled Si deposition:

- Particles deposited in the first 1.5 s phase of Ag sputtering are subsequently buried under the second phase of Si sputtering. This limits their mobility as it strongly curtails surface diffusion. Fewer particles have therefore the possibility to agglomerate and form bigger particles.
- The potentially high number of small particles is not or only barely discernible in TEM images, because the now twice as thick sample - compared to the five references - has worse contrast and resolution.

The former point is also not in contradiction with the high average particle size calculated for this sample. Instead, the average particle size is that high precisely *because* the smaller particles are invisible. If this reasoning is indeed correct it would also drastically increase the number density in this sample. These results are in good agreement with the previous results of Ag particles without a Si matrix. Although the size distribution is not bimodal as in the case of Ag particles on a carbon support film, the mode particle sizes are in a similar range. Another potential reason for the huge variation in average size, number density and volume density - at least for last sample - is the non-exact and non-identical position of the substrate under the target during sputtering. A change of lateral position of the substrate with respect to the

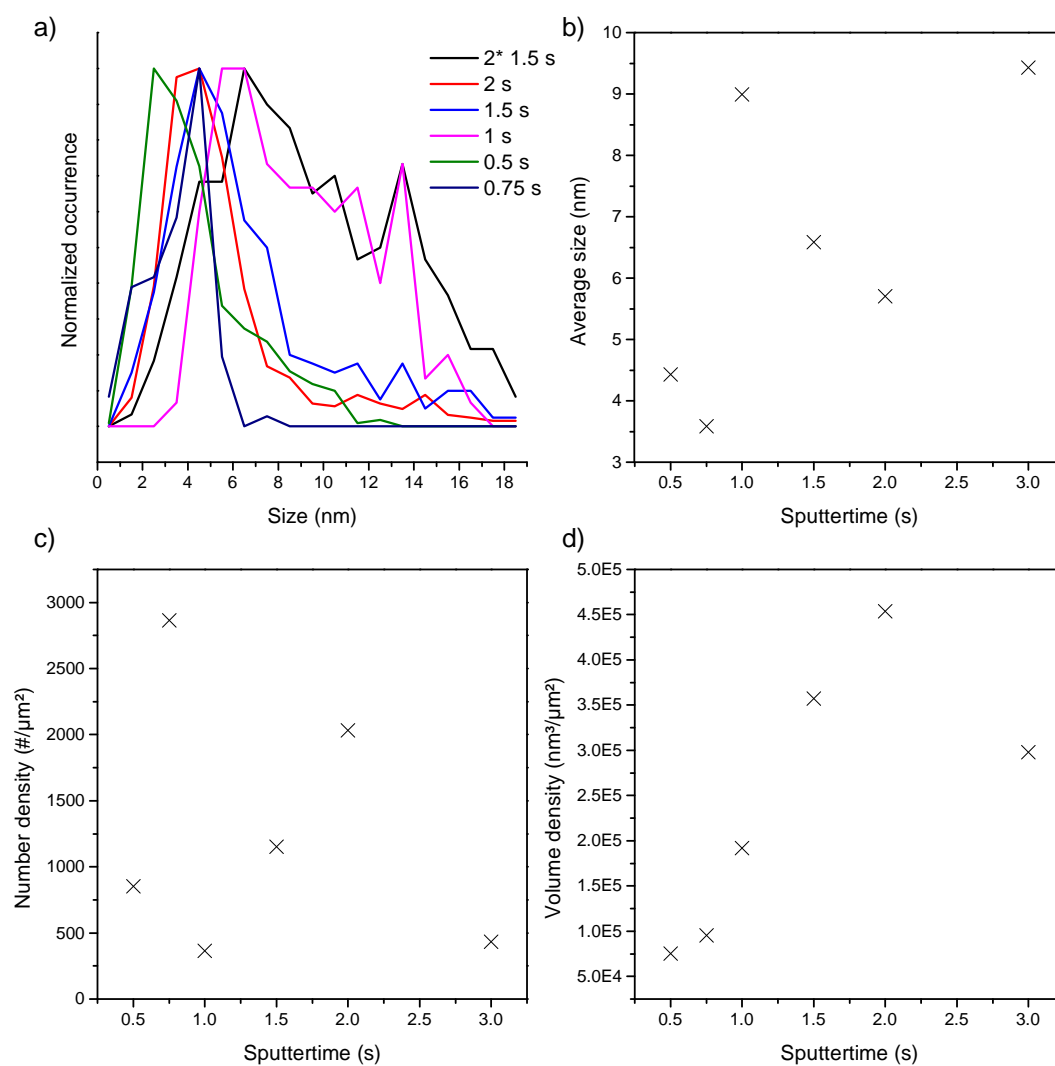


FIGURE 5.2: Influence of the sputter time of particle size and density. a) Size distribution of samples with sputter times from 0.5 to 3 s. The mode size of all samples varies between 2 and 7 nm. b) Average size of particles with respect to sputter time. c) Number density of particles with respect to sputter time. d) Volume density in nm^3 of Ag per μm^2 analyzed area with respect to sputter time.

target during deposition between different samples might be reflected in the unintuitive and seemingly random results of size and density. Furthermore, the substrate diameter of 3 mm also leaves leeway for local differences within samples therefore potentially giving rise to the unexpected results.

Besides the particles, the Si matrix in these samples was also subject to analysis. As shown by diffraction experiments (cf. Figure 5.3) and supported by high resolution, the Si matrix is entirely amorphous. As shown by the extensive works of Haberl [65] structural differences between various amorphous Si modifications exist, but are marginal and are expected to not drastically influence Ag mobility. One of the most reliable indicators of amorphous materials is the nearest neighbor distance. Unfortunately, though, the nearest neighbor distance varies around 2.35 Å which coincides with the Ag (111) diffraction maximum. As such, no exact characterization of the Si matrix can be undertaken in the presence of crystalline Ag particles. However, as the co-deposition of matrix and particles might very well have an influence, the deposition of amorphous Si without Ag nanoparticles will solve this issue as it mightly simply be a different amorphous Si. However, as previously mentioned, the Ag mobility is not expected to be strongly affected by the minute structural differences.

In comparison with particles deposited on bare carbon films as presented in Figure 5.1, no pronounced bimodal size distribution was found, the mode particle size has

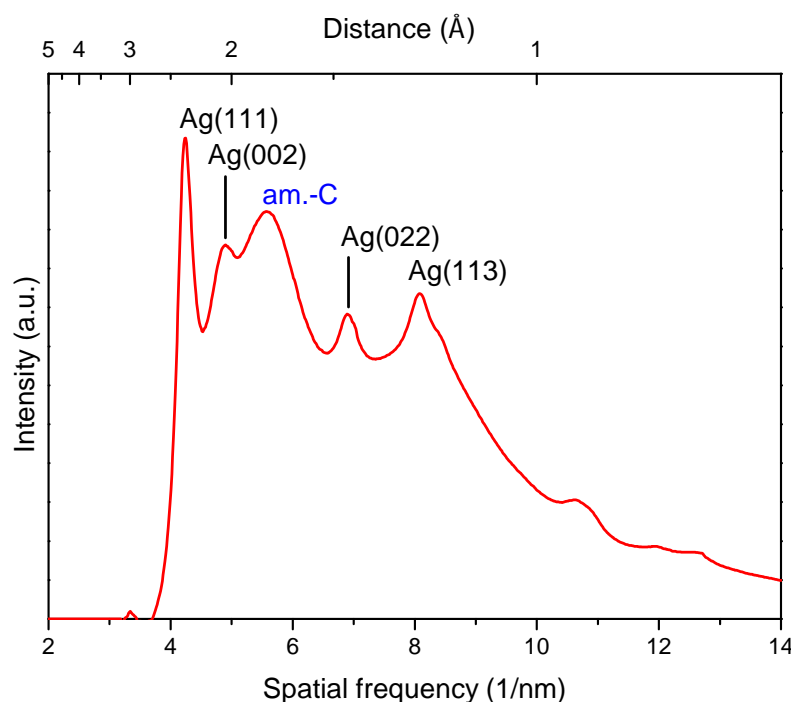


FIGURE 5.3: Azimuthal average of a diffraction pattern intensity of Ag particles in Si matrix. Diffraction maxima belonging to the crystalline Ag particles are clearly assignable at 2.36, 2.04, 1.44 and 1.23 Å. No diffraction maximum assignable to crystalline Si is present which would be expected at 3.14, 1.92 and 1.64 Å. The diffraction maximum of amorphous Si lies at 2.35 Å and is therefore indistinguishable from the Ag diffraction maximum.

a similar maximum at around 2 nm though. The difference in sputtering power (10 W for the carbon film samples and 40 W for the Si matrix samples) also explains the different amount of sputtered silver. The linear trend of the volume density apparent from the first five data points in Figure 5.2 would result in a volume density of around $1.3 \cdot 10^6 \text{ nm}^3/\mu\text{m}^2$ so roughly a factor of three below the measured volume density of $4.5 \cdot 10^5 \text{ nm}^3/\mu\text{m}^2$ while the difference in sputtering power is a factor of four. The general trend is thus obvious, the numbers suggest that the power does not scale linearly with the deposited amount of Ag but shows a correlation smaller than linearity.

As briefly discussed in the introduction, preliminary investigations quickly showed that monometallic particles were not a promising approach for memristive switching because of immobilization of Ag at the back electrode. Accordingly, as monometallic particles were discarded for the functionality of nanoparticulate memristors, investigations on these were put on hold and the fabrication of bimetallic particles was pursued.

5.3 Bimetallic AgX particles (X = Au, Pt)

After this proof of concept bimetallic particles with a gold or platinum wire in a silver target were produced. The aim was to accurately quantify the chemical composition to check whether the bimetallic target produced particles as intended, as well as what the composition of these particles was and whether it can be controlled. Particles were sputtered onto plain carbon films with a thickness of a few nanometers such that they are easily analyzable in a TEM.

The first important point to raise is that of particle composition and to check whether the wire-in-target method does indeed produce bimetallic particles and what their shape is. As previously shown in several studies, bi- or polymetallic particles can take various morphologies such as core-shell particles[66]–[68], Janus-type particles[69], [70], alloy particles[71], [72] or a range of combinations of these.[73]. As already observed for the monometallic case, TEM investigations on bimetallic AgAu GAS-produced nanoparticles are alloy particles. This comes as no surprise as Ag and Au are perfectly miscible even in the bulk case.

The pressure in the GAS changes the number of particles, but the particles size is virtually independent from it. The slight variation between mode diameters from 8 to 12 nm is attributed to statistical variation. The volume density (or number density) of nanoparticles can of course be controlled by the sputtering time. However, as seen in Figure 5.4 a) at a certain number density of particles agglomeration on the substrate occurs such that individual particles are not separable anymore. The composition was also subject to analysis in order to check whether the deposition at different pressures might have an influence on the Ag to Au ratio. Results of these investigations are depicted in Figure 5.5. The particle composition was tested by four different methods: Quantification by TEM-based EDX, SEM-based EDX and XPS

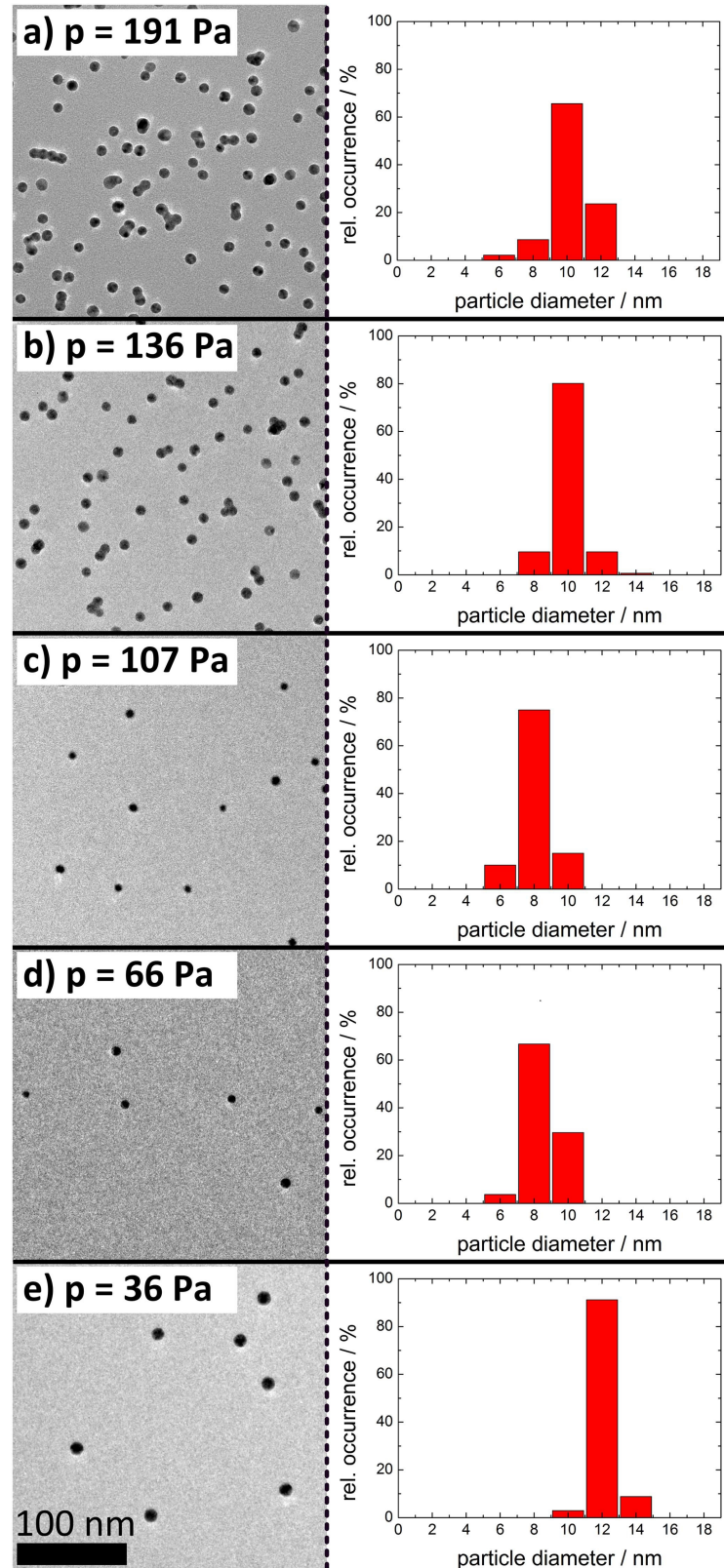


FIGURE 5.4: TEM bright field images and particle size distribution with respect to sputtering pressure of the GAS. Sputtering power was 40 W for 10 s. Scale bar for all micrographs see e). Reproduced from Reference [63].

as well as estimating the composition from the plasmon peak recorded by UV-Vis spectroscopy. All investigations show the same trend, that an increase in pressure leads to an increase of the Au content. However, there is apparently a systematic offset between XPS, UV-Vis and EDX quantifications. The former observation, of an increased Au content at elevated pressures is understandable, as the region where target atoms are sputtered - the sputter trench - is more narrow at higher pressures, therefore more "focused" on the embedded Au wires such that more Au and less silver is sputtered out of the target. The offset between quantification methods is less obvious but might be caused by an enrichment of Ag in the particle shell. As the signal generating volume of XPS is strongly limited by the mean free paths of photoelectrons in the nanoparticles, XPS mainly probes the surface of these particles. Furthermore, the surface plasmon resonance probed by UV-Vis is also affected by this phenomenon. EDX, on the other hand, probes the entire particles as characteristic X-rays can escape from the entire volume. Furthermore, the theory of Ag enrichment at the surface of particles is backed by previously reported segregation of Ag and Au [74], [75] where it was indeed observed, that the Ag concentration is higher at the surface. This effect is not visible by STEM-HAADF imaging, even though it is Z-contrast-based, because there is pronounced core-shell character of these particles but a smooth transition between Au- and Ag-rich regimes which is inseparable from the contrast differences between the middle of the particle and its fringe. The middle is both thicker and Au-rich, causing stronger scattering of the e-beam, while the fringe is thinner and Ag-rich, causing less scattering of the e-beam and lower image contrast accordingly.

These samples were also subject to tomographic analysis. To this end, the AgAu particles were embedded in a Si matrix which was cosputtered with the aim of producing a particle gradient. The sample was produced by depositing five consecutive layers. Each individual layer was formed by depositing 60 s of Si and 10 s of nanoparticles. The deposition time of the nanoparticles was reduced by two seconds for each consecutive layer. The overview image of the analyzed area is depicted in Figure 5.6. The homogeneous particle distribution in the X-Y plane is apparent. Due to the inevitable trade-off during tomography acquisition, the resolution during the investigations was severely limited by the low spatial sampling rate of the individual STEM images. The presented image has dimensions of 512 by 512 px which equals an area of 350 by 350 nm. It was defined that a single particle must cover at least two by two pixels in order to produce reliable results. Given that previous investigations showed that below a threshold of 1.5 nm only insignificant amounts of particles are deposited the resolution was chosen such that a diameter of 2 px relates to a diameter of about 1.5 nm. This image resolution was deemed sufficient for these investigations. The determined particle size distribution from the investigations is shown in Figure 5.6 b). Unlike previous AgAu samples (cf. Figure 5.4) or embedded Ag particles (cf. Figure 5.3, sample with $2 \cdot 1.5\text{s}$ duration), these embedded AgAu particles show a surprisingly low mode size of only 2.5 nm.

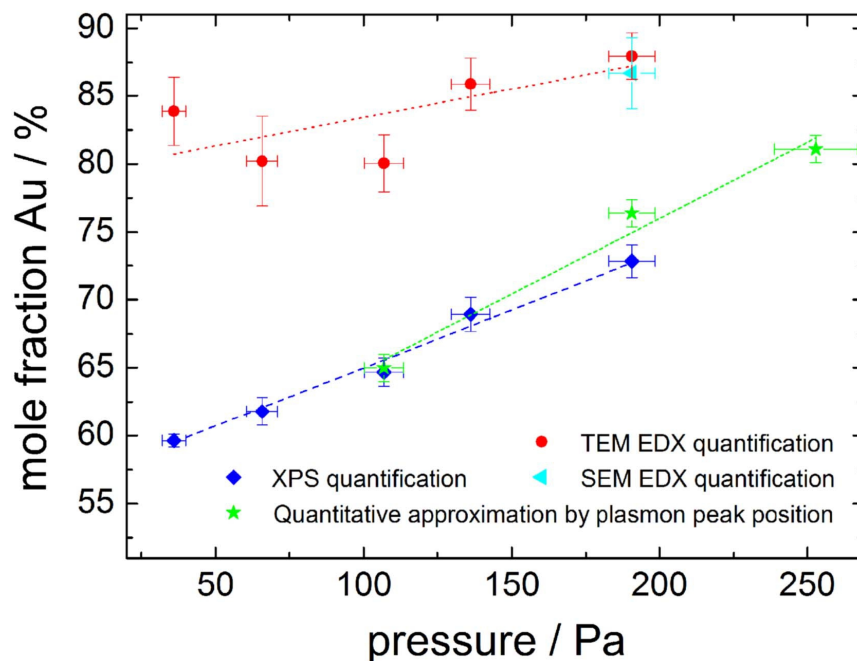


FIGURE 5.5: Composition of bimetallic particles produced by the GAS. A higher pressure during sputtering correlates to a higher content of Au in the particles. Error bars of concentration represent standard deviation (XPS), uncertainty of quantification (EDX) and error in linear approximation (UV-Vis), error bars in the pressure corresponds to the hysteresis of flow controllers. Reproduced from Reference [63].

Different tilt schemes for tomographic analysis were evaluated for this sample. The maximum range of tilt angles of the best tomographic analysis was from plus to minus 63° and was achieved by applying the Saxton tilt scheme.[76] With the Saxton scheme images are acquired at tilt angles that are far apart at low tilt angles and

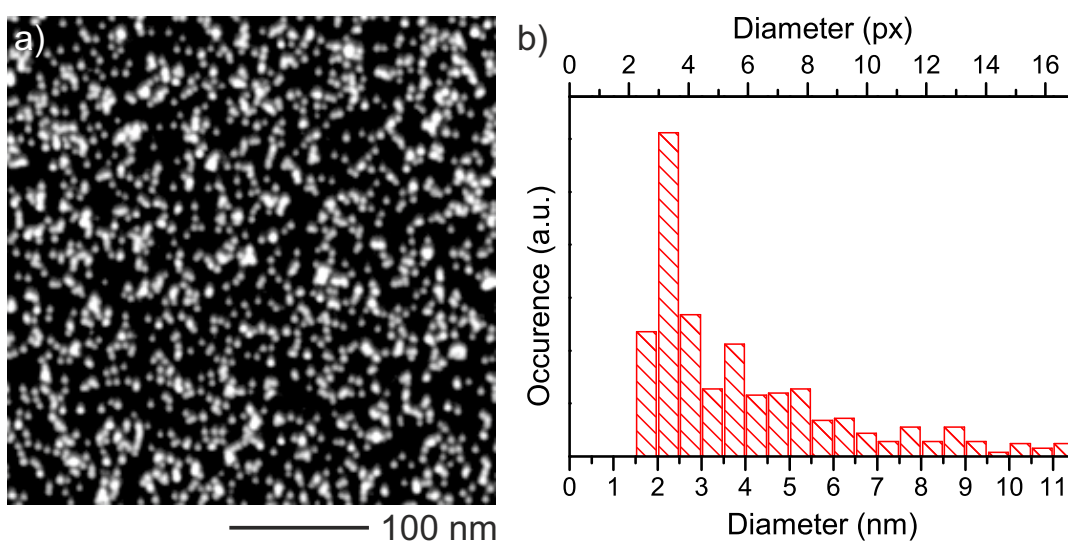


FIGURE 5.6: a) STEM-HAADF Overview image of the area analyzed by tomography showing the Y-Z plane. b) Size distribution of the deposited particles.

closer together at high tilt angles. The angles are chosen such that the $\cos(\psi)$ of the tilt angle ψ are roughly equidistant. While originally developed for tomographic analysis of crystalline samples the added benefit of this tilt scheme is the effective reduction of electron dose while still maintaining an overdetermined data set for tomographic reconstruction.

Figure 5.7 shows the result of the reconstruction. In the X-Z and Y-Z plane view a pronounced particle gradient from low concentration (bottom) to high concentration (top) is apparent thus confirming that the deposition was successful. This also proves that the particles are properly fixated in the matrix and no rearrangement takes place. The reconstruction displays the particles as slightly elongated in Z direction. This is likely an artifact due to the missing wedge problem caused by the inability of the microscope to acquire images of the sample in range from plus to minus 90° . All individual images recorded at varying angles always show circular particles. Acquiring a tomographic tilt range from even higher angles in an attempt to minimize this artifact was not possible. Analogous to the AgAu particles, AgPt particles were fabricated, the statistical evaluation of TEM results is shown in Figure 5.8. Particles sputtered for intermediate times between 4 and 10 s show a pronounced bimodal

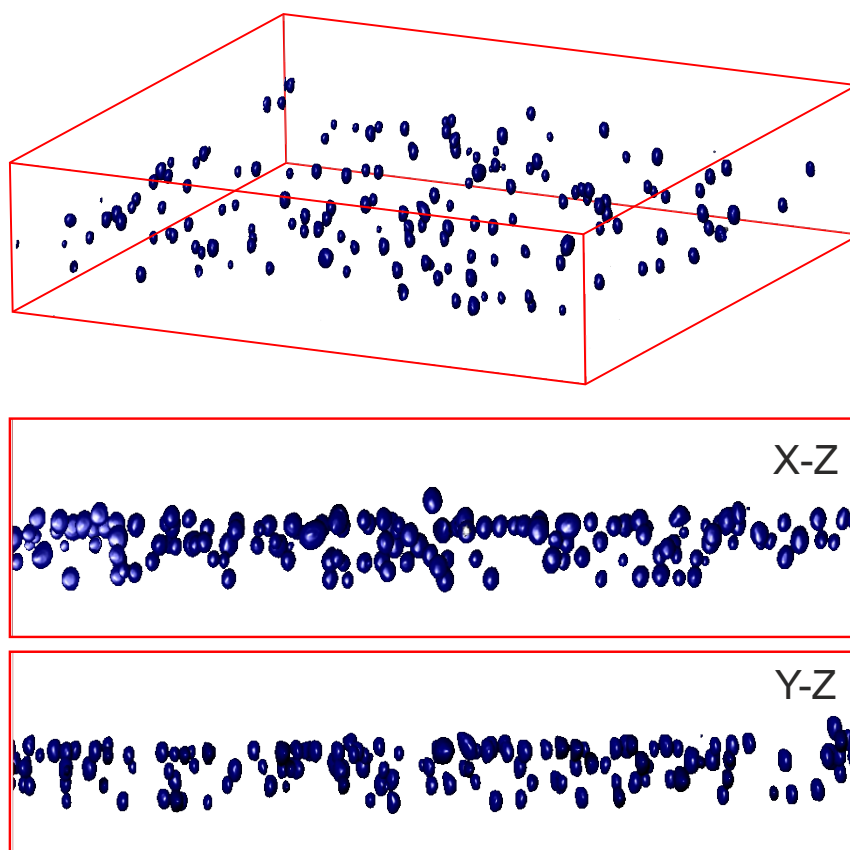


FIGURE 5.7: Tomographic reconstruction of particles embedded in a Si matrix. Red box is around 70 nm high and 280 nm wide and deep. The side views onto the Y-Z and X-Z planes clearly show the particle gradient otherwise invisible from the top view onto the X-Y plane.

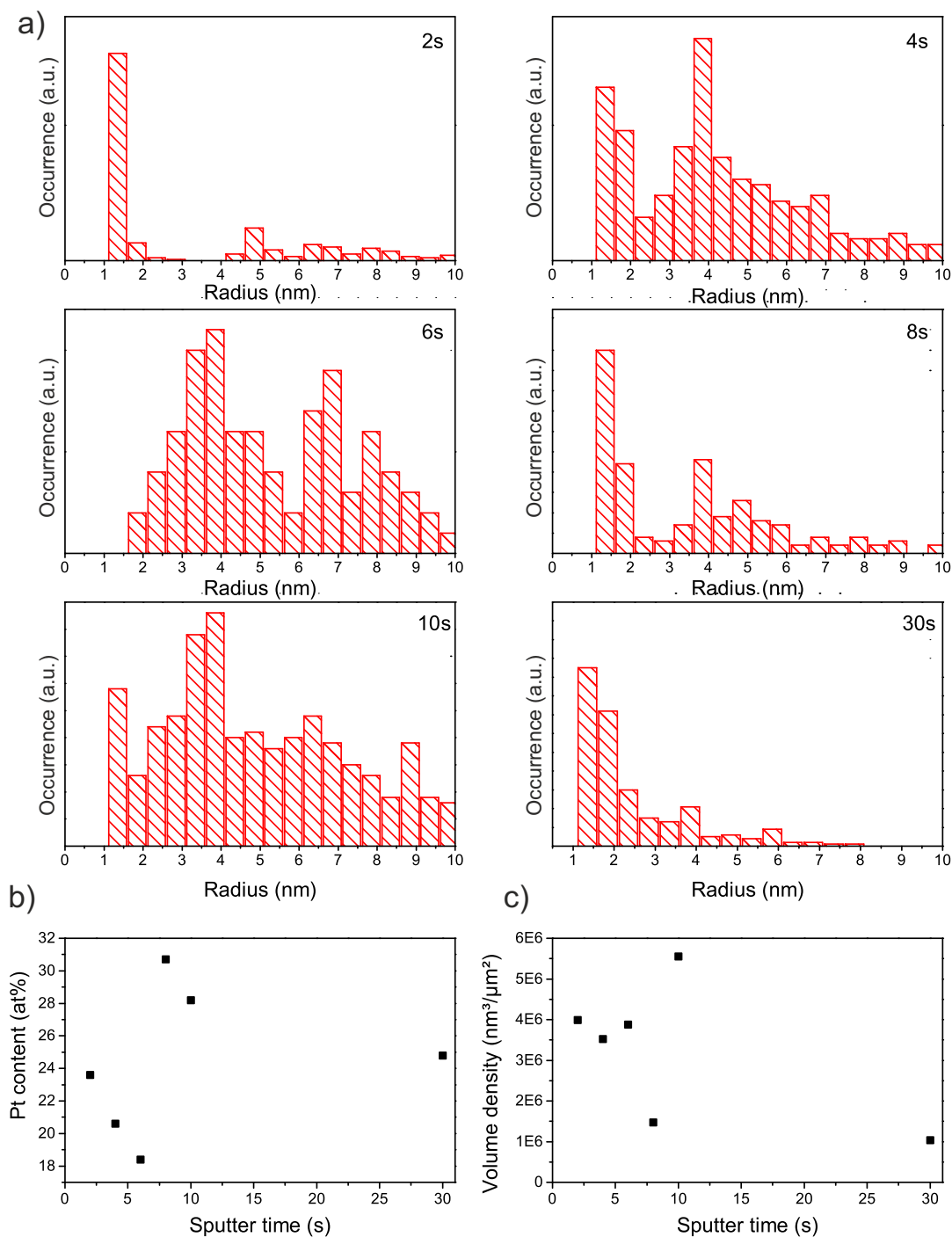


FIGURE 5.8: Particle analysis of AgPt samples. a) Size distribution of AgPt particles sputtered for 2/4/6/8/10 and 30 s. b) Pt concentration with respect to sputter time. c) Volume density of deposited particles with respect to sputter time.

size distribution similar to monometallic Ag particles sputtered for 5 s with varying mode particle sizes, though. (cf. Figure 5.1) The sample sputtered for a mere 2 s mainly shows very small particles below 2 nm diameter. The sample sputtered for 30 s on the other hand mainly shows extremely small particles with a monomodal distribution. The evolution of particle size distribution up to 10 s seems plausible:

Short sputtering times do not allow for agglomeration of particles such that mainly small particles arrive at the substrate. At intermediate sputtering times a bimodal size distribution evolves probably by the same mechanism as for monometallic Ag particles. The extremely broad size distribution at 10 s implies that by this time lots of particles merge together on the substrate surface. The size distribution at 30 s does not fit into this picture. In order to resolve the particle composition and total volume density have been determined. While the Pt content of particles is not expected to vary with sputter time, the volume density should scale in a similar way as seen for the Ag particles. Naturally, the Pt concentration varies within a range and taking into consideration inaccuracy of the EDX system the range between 18 and 31 at% of Pt seems reasonable. Oddly, though, the volume density should show an increasing trend with increasing sputter time. The determined volume densities follow no trend at all and the longest sputter duration seemingly resulted in the smallest amount of deposited particles. No satisfactory explanation can be presented at the current state of investigations. Further experiments are necessary to increase statistical significance. As the GAS deposition mechanisms are not fully understood the non-existent trend might also be caused by outliers. A possible explanation is also the previously discussed variation of sample position during deposition and the region of TEM investigation. If anything, the results suggest that there is a large variability in the produced samples such that further research has to be conducted. In summary, TEM investigations showed that the GAS did in fact produce mono- and bimetallic particles as desired and that the size distribution and composition can be controlled by sputter parameters. The origin of bimodal size distributions remains disclosed. The successful deposition of a Ag particle gradient in a Si matrix was shown by electron tomography. As experiments and simulations showed, nanoparticulate memristors based on monometallic particles were not feasible. Production of bimetallic particles, in particular with Ag and Pt, still poses a number of questions as the results do not allow a clear deduction of particle formation mechanisms. Therefore, extensive research on bimetallic nanoparticulate memristors is ongoing.

Chapter 6

Investigations on Memensors

As described in the introduction, memensors are meant to combine memristor and sensor functionality. While theoretically applicable to all kinds of sensors where the sensor shall adapt to a baseline input, sensors in the focus of this work are sensitive to certain gas species as well as pressure. Other sensors, sensitive for optical inputs, electrical or magnetic fields, or sound are not dealt with.

Sensors in this work were fabricated by Irina Plesco, Vasile Postica and Oleg Lupan. All sensors are based on materials with extremely high surface-to-volume ratios produced in the workgroup *Functional Nanomaterials*, specifically tetrapodal ZnO (t-ZnO) and Aerographite, a hollow graphite structure derived from t-ZnO. These scaffold materials were decorated with compound semiconductors, i.e. InP, CdS and CdTe. All TEM investigations were conducted by the author of this thesis.

6.1 InP-Aerographite strain sensor

These samples were grown by hydride vapor phase epitaxy (HVPE) deposition [77] of InP onto different scaffolds, i.e. t-ZnO, Aerographite and carbon nanotube tube (CNTT) substrates. The latter is closely related to Aerographite, except that the walls of the hollow structure are made up from CNTs instead of graphite planes. Details on the fabrication of Aerographite can be found in Reference [78]. Two approaches for synthesis were chosen, namely the HVPE deposition of InP supported by the preliminary deposition of Au NP onto the scaffold and without the Au particles. The synthesized sensors presented themselves as hollow, porous frameworks of Aerographite decorated by micro- and nano-crystallites.[79]

The electrical characteristics as well as the response to an applied strain is displayed in Figure 6.1. The non-linear I-V characteristic underlines that this device is not a simple ohmic conductor. The electrical response in b) highlights the sensor properties.

6.1.1 InP deposition on tetrapodal ZnO

Initial attempts to synthesize InP on top of t-ZnO resulted in unintended synthesis of different phosphates like InPO_4 (cf. Figure 6.2, space group Pnma) and $\text{Zn}_3(\text{PO}_4)_2$ (cf. Figure 6.3, space group C2/c). In both cases the synthesized structures were in

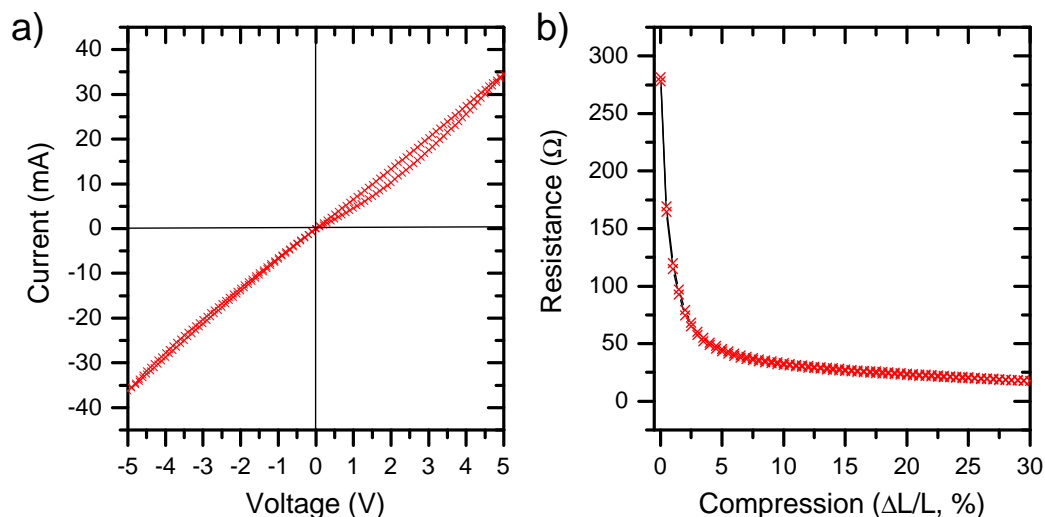


FIGURE 6.1: I-V curve and electrical response to applied strain of an InP hybrid material. a) I-V curve of an InP-Aerographite hybrid material. The I-V curve resembles that of a bipolar, analogous memristor as described in section 2. b) Electrical response to an external applied strain. Measurements were conducted by Irina Plesco.

the form of needles that are between 300 and 400 nm thick and several micrometers long. These needles have in common that they contain an In rich core, apparent from both the high Z contrast in the STEM-HAADF images as well as the EDX signal confined to the core region (see Figure parts b)). In the case of InPO_4 the same selected area electron diffraction (SAED) pattern clearly showed a single crystalline as well as a strongly polycrystalline content. Dark field imaging of the $31\bar{1}$ reflection of InPO_4 showed that the single crystalline content belonged to the core of the needle while DF imaging of the polycrystalline rings showed that these belonged to the shell of the needle. (Figure 6.2 e) and f)) Therefore, the needle apparently consists of a single crystalline InPO_4 core surrounded by a polycrystalline InPO_4 enriched with Zn. The Zn was deliberately included in the reaction as it was supposed to act as a dopant for InP. Unsurprisingly, the needles are strongly sensitive to prolonged electron beam irradiation, such that the comparison of before (Figure 6.2 c)) and after (Figure 6.2 d)) images shows a strong change in morphology. The needle's core does not lose its single crystalline character though, the morphological change apparently is restricted to the polycrystalline shell.

In the case of the observed $\text{Zn}_3(\text{PO}_4)_2$ phase no differentiation of single and polycrystalline regions was possible. As previously mentioned the needles generally resemble each other as they both contain an In enriched core. However, the diffraction pattern (cf. Figure 6.3 a)) acquired from the entire needle shows a single crystalline pattern assigned to $\text{Zn}_3(\text{PO}_4)_2$. In conjunction with the elemental line scan shown in Figure 6.3 b) it was concluded that the Zn rich shell contains crystalline $\text{Zn}_3(\text{PO}_4)_2$. It should be noted that the needle is several hundred nanometers in diameter and the single crystalline SAED was recorded from one specific domain. However, no

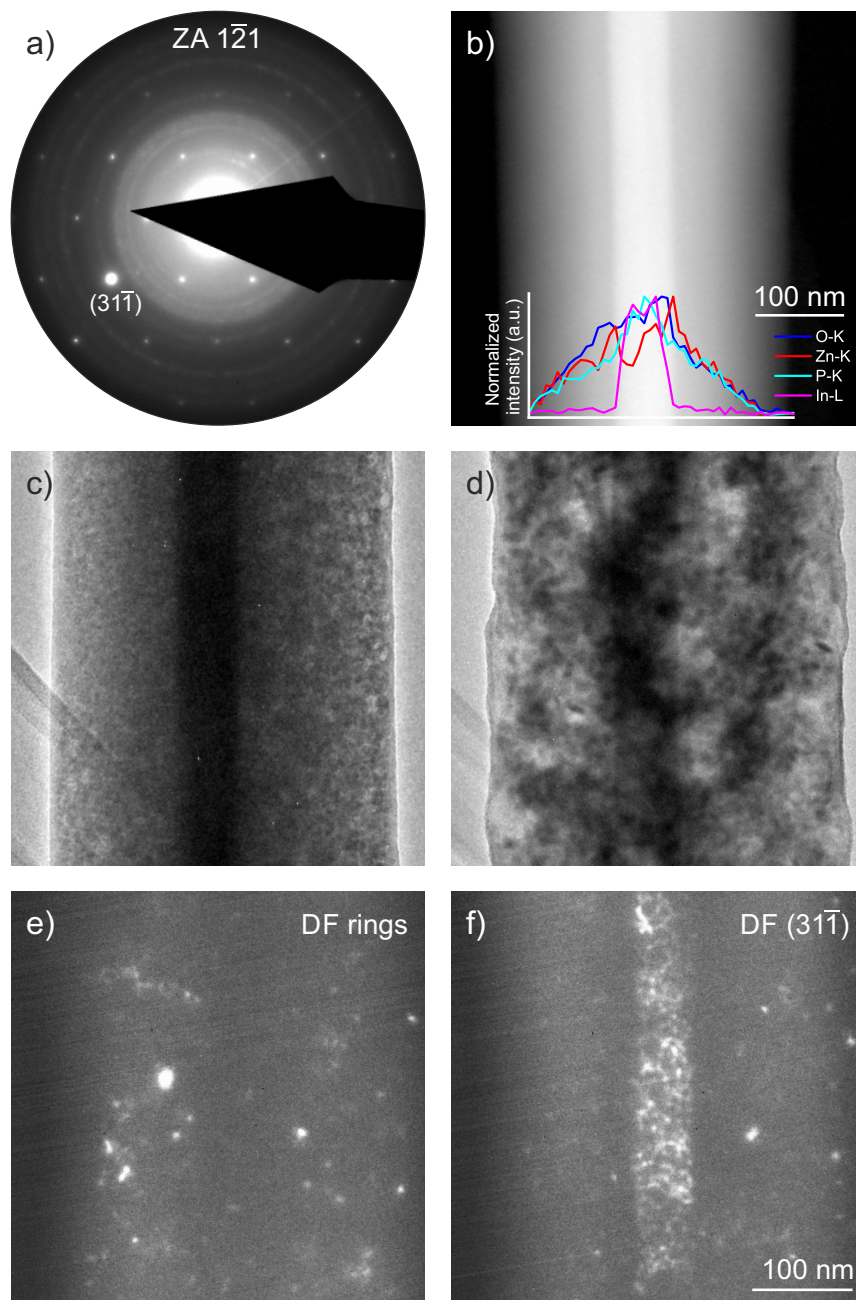


FIGURE 6.2: TEM analysis of InPO_4 needle. a) SAED pattern of the needle ($\text{ZA } \bar{1}21$ of sg. Pnma). The pattern also contains several rings indicating a coexistence of the single crystalline InPO_4 with a polycrystalline $\text{Zn}_3(\text{PO}_4)_2$. b) STEM-HAADF image of the needle indicating that it consists of a heavy core with a lighter shell. Inset shows the composition across the needle proving that the core contains In while the shell does not. c) and d) Needle before and after intense e-beam irradiation highlighting the sensitivity of the material. e) DF image with the objective aperture placed on the rings of the pattern in a). f) DF image with the objective aperture placed on the $31\bar{1}$ reflection visible in a).

strongly polycrystalline regions comparable to those in shown in Figure 6.2 a) were observed.

As no InP synthesis was successful on this scaffold and only phosphate phases were observed, the synthesis on InP on top of t-ZnO was deemed non-conductive and deposition onto the other scaffold materials was explored. The main reason for the

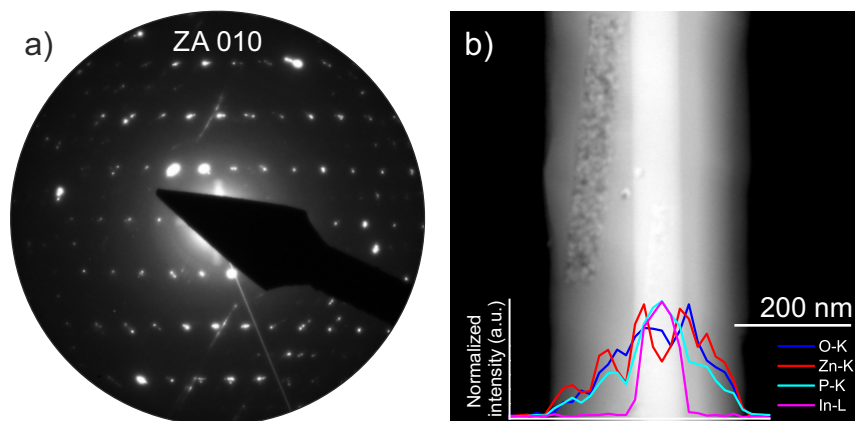


FIGURE 6.3: TEM analysis of $\text{Zn}_3(\text{PO}_4)_2$ needle. a) Diffraction of the needle. (ZA 010 of sg. C2/c) b) STEM-HAADF image of the needle indicating that it consists of a heavy core with a lighter shell. Inset shows the composition across needle proving that the core contains In while the shell does not. Speckled pattern to left of the core is caused by intense e-beam irradiation and accompanying morphological change.

production of phosphates is likely the interaction between the hydride vapor and the ZnO.

6.1.2 InP deposition on carbon nanotube frameworks

Subsequent synthesis attempts were more successful as no more phosphate products were found. Fabrication of InP-CNTT compounds did not show any oxides or oxygen containing phases. However, as depicted in Figure 6.4, no smooth coverage of the scaffold material by InP was achieved. Instead, few large particles are scattered across the CNTT surface. The SAED pattern contains diffraction rings belonging to the CNTT scaffold as well as reflection with d-values of 2.85, 2.68, 1.76 and 1.19 Å which could not be assigned to any known InP-phase with the space groups $I4_1/amd$, $Fm\bar{3}m$, $F\bar{4}3m$ or $P6_3mc$. As EDX quantification of these particles resulted in a stoichiometry of $\text{In}_{49}\text{P}_{51}$ with no detectable amounts of oxygen or any other element no phosphate or other tertiary compounds were considered. Besides these smaller particles, SEM investigations also showed large micro particles within and outside of the CNTTs. Notably, the InP within the CNTT scaffold formed in an area where the CNTT walls were porous and thus extremely permeable whereas the InP particle on the outside of the CNTT formed on a seemingly much more solid wall of CNTs. These particles were much too large to analyze them by TEM. As the aim was to achieve a uniform coverage of the scaffold by InP, this scaffold, too, was dismissed as non-suitable.

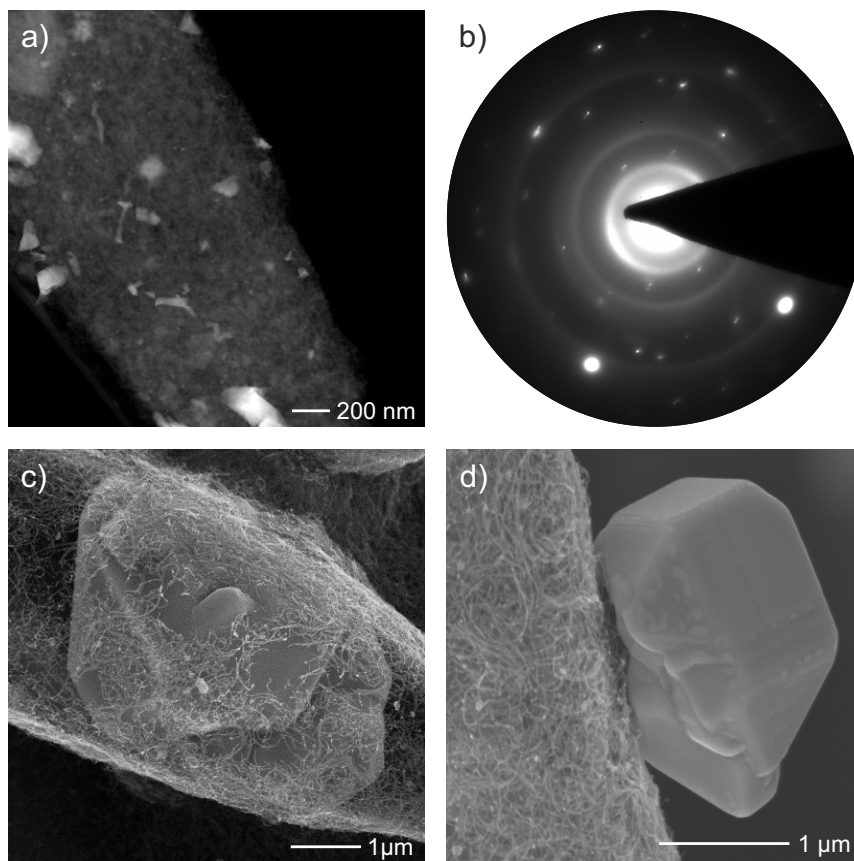


FIGURE 6.4: TEM analysis of InP on CNTTs. a) STEM-HAADF image of a CNTT covered with InP particles scattered across it. b) Diffraction pattern containing the characteristic diffraction rings of CNTTs and additional non-assignable diffraction maxima not belonging to any known InP phase.

6.1.3 InP deposition on Aerographite

Finally, InP deposition onto Aerographite was conducted. Interestingly, the results showed that this synthesis approach resulted mainly in microwires of dozens of micrometer in length and up to two micrometer in diameter as shown in Figure 6.5. The initial SEM analysis shows that the produced InP microwires are of about the same diameter as the AG scaffold, their length far exceeds that of the scaffold though. Subsequent TEM analysis shows that wires apparently form on the inside of hollow Aerographite tubes. The existence of InP was confirmed by diffraction experiments which showed that InP crystallized the cubic zinc blende structure (space group $F\bar{4}3m$). This nicely corresponds with literature, where Zn doping of InP also prohibited the crystallization in the wurtzite structure and instead promoted the cubic zinc blende system.[80]

Furthermore, EDX quantification was conducted which showed a stoichiometry of the wires on the inside of the Aerographite tubes of about $In_{45}P_{55}$ thus being congruent with the deductions about the crystal structure. Without a reference sample

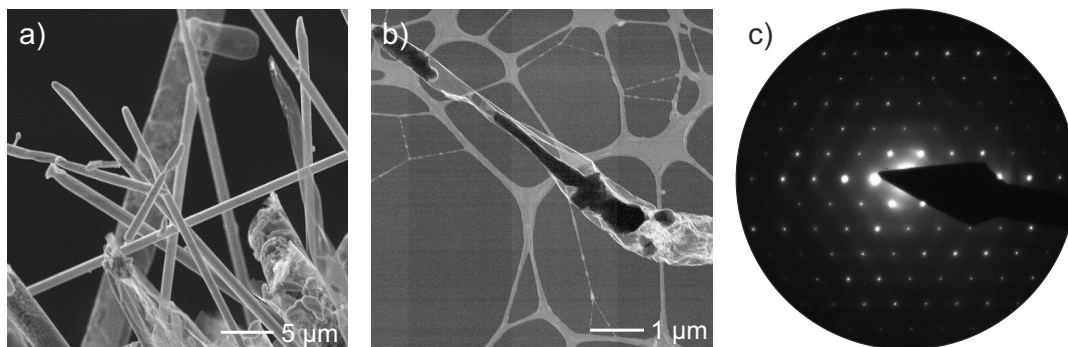


FIGURE 6.5: Electron microscopy analysis of InP-AG compounds. a) SEM image of InP microwires grown onto Aerographite. Some AG residues are visible in the foreground. b) Low-magnification STEM-HAADF image of an InP wire grown on the inside of Aerographite suggesting that even the wires which are dozens of micrometers long might start growing on the inside of the AG scaffold. c) SAED pattern of InP in the zone axis 111 (space group $F\bar{4}3m$).

for calibration the EDX accuracy is estimated to be around 5 % including the uncertainty of peak fitting of about 2 - 3 %. EDX analysis allows quick differentiation between InP and the occasional ZnO residue present on the inside of AG.

A more detailed analysis of the microwires, particularly those which are not surrounded by AG - which would complicate their analysis - showed several interesting features, as presented in Figure 6.6. The wire shown in part a) contains several lenticular shapes with two distinct orientations in the wire which are about 120° apart. As these shapes appear in HAADF contrast the assumption was that it might be a chemical segregation of some sort. However, EDX analysis uncovered no additional elements in this wire and the EDX line scan along the wire (see inset) confirmed a constant composition. Note that the seeming phosphorus enrichment might very well be an artifact of improper EDX quantification and thus a systematic error. As no chemical segregation seems to be the reason for these features, a structural reason was explored afterwards. The SAED pattern in Figure 6.6 b) shows a single crystalline pattern in cubic InP of the space group $F\bar{4}3m$ with no obvious peculiarities. The commonly observed twinning InP wires therefore seems not to be the origin.[81] Still, as the 120° angle between the features suggests, they are likely still related in some form to the crystal structure. Dark field images from the diffraction spots belonging to the planes structurally equivalent $2\bar{2}0$ and $\bar{2}02$ were acquired and are displayed in figure parts c) and d), respectively. While the dark field image from the $2\bar{2}0$ spot still indicates the position of these defects the strong diffraction contrast parallel and close to the fringes of the wire cuts right through the lenticular shapes. On the other hand, the dark field image taken from the $\bar{2}02$ spot shows that particularly the shape more in the center of the image cuts right through the region of strongest diffraction contrast. A slight tilt of the $(\bar{2}02)$ plane within the defects forming a low angle grain boundary might therefore be the cause of the defect. High resolution micrographs taken at the apex of the defects, i.e. right at the fringe of the wire, reveal a bump bulging around 8 nm out of the wire surface and

exhibiting a different HR contrast than the rest of the wire. While the latter shows the InP [111] orientation as previously shown in the diffraction pattern, the small bulge shows lattice planes with a spacing of 2.22 Å might belonging to metallic In which has a (110) spacing of 2.30 in its tetragonal modification. This lattice spacing is only present in the bulge outside the wire and has not been observed anywhere else in this sample. The Fourier Transform (FFT) (cf. Figure 6.6 f) also contains the reflections to these planes (see red circles) which do not seem to be crystallographically related to the InP planes thus excluding an epitaxial relation. Besides that, a very weak triplet of reflections (white arrows) is visible in on $\langle 220 \rangle^*$ direction with a periodicity of about 5.93 Å. As inverse FFT filtering proves, these reflections also originate in the small outward bulge. Although these reflections are parallel with the $\langle 220 \rangle^*$ reflections of InP their distance does not coincide and is off by about 0.1 Å. Whether these two features - the presence of InP and a set of planes of with a long periodicity - are connected to the lenticular defect in the InP wire is uncertain but likely, given that they appear in close proximity to it. HR imaging of the interface between the defect and the rest of the wire (Figure 6.6 g) shows no reorientation

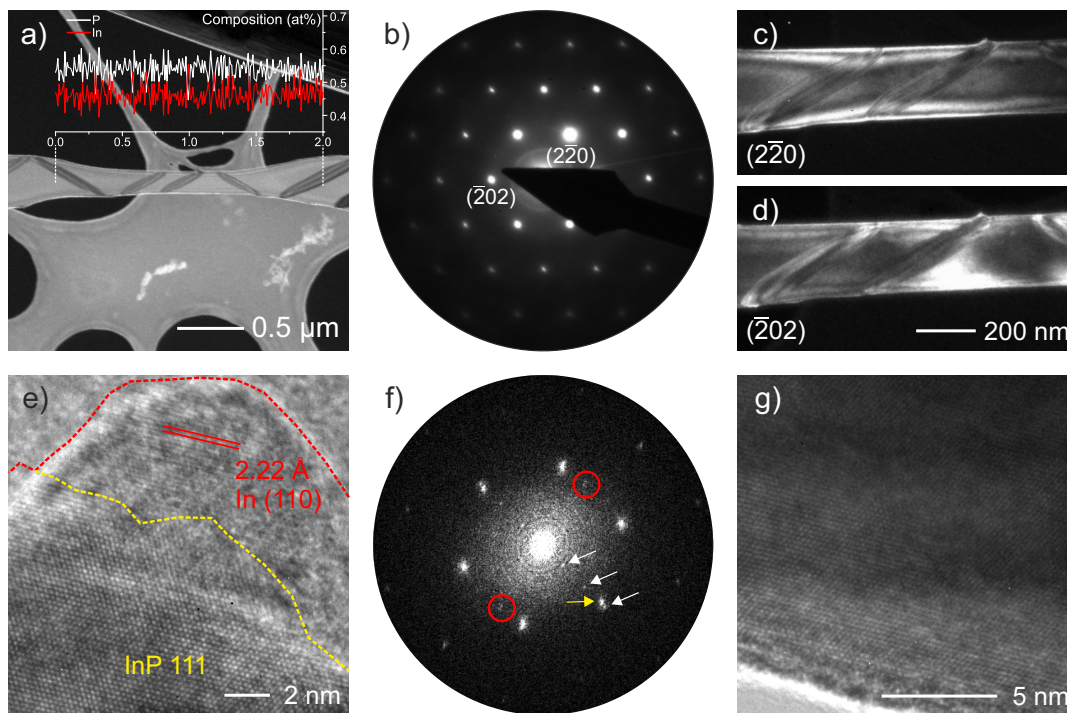


FIGURE 6.6: TEM analysis of InP microwires with lenticular defects. a) STEM-HAADF image of an InP wire with lenticular defects inside. Inset shows In and P composition determined by EDX along the wire. The defects do not seem to correlate to any change in composition. b) SAED pattern of the wire (ZA 111 of InP sg. $F\bar{4}3m$). Marked reflections masked by objective aperture to acquire dark field images in c) and d). e) HR image of the apex of one of the defects where seemingly an In nodule has formed. f) FFT of the HRTEM micrograph in e). g) HRTEM micrograph of the boundary between a lenticular defect (top two-thirds of the image) and the "matrix" (bottom third). A slight contrast variation from dark (top) to bright (bottom) is visible, but no prominent structural defect is discernible in the image.

of the lattice at the interface. The only discernible feature is the contrast variation between wire and defect.

Accordingly, as there is no chemical segregation, no observable difference in crystal structure in the observed zone axis, a buried low angle grain boundary resulting in a slight distortion in the $\bar{2}02$ lattice plane of InP seems to be the most likely candidate to cause these lenticular defects. Alas, they might also be connected to the bulges observed at the apex of the defects. As grain boundaries generally offer better diffusion, excess In could migrate along the grain boundaries towards the surface of the wire where it forms the aforementioned bulges.

In summary, these samples resulted in the highest quality InP-Aerographite hybrids in terms of phase purity and crystal quality and are also the samples on which the previously shown I-V curves (cf. Figure 6.1) were recorded. As will be discussed below, a further decoration of the Aerographite scaffold with Au nanoparticles which were meant to catalyze the formation of InP was not necessary and indeed counter-productive.

6.1.4 InP deposition of Aerographite decorated with Au nanoparticles

TEM investigations on Aerographite samples decorated with Au NPs (cf. Figure 6.7) showed that microsized rods of crystalline InP in the space group $F\bar{4}3m$ evolved during synthesis. The SAED pattern shows the coexistence of two InP domains though. As presented in the superposition of two simulated diffraction patterns of InP in the zone axis (ZA) $1\bar{1}0$ mirroring of the pattern at the (112) plane produces a pattern congruent to the experimentally observed one. The pattern is therefore caused by a (112) compound twin of InP. The twinning domains could also be imaged in TEM bright field mode, as shown in Figure 6.7 d). The individual domains are around 25 to 35 nm thick and are clearly separable by their different diffraction contrast as well as difference in slope of the microrod surface. Twinning is commonly observed in InP rods and wires as documented numerous times in literature.[82]–[84] Notably, though, the twinning documented in cubic InP wires and rods is mostly (111) type I or type II twinning. No case of (112) twins in InP was found in literature. However, aforementioned wires were synthesized either on quartz or on (111) Si. The deposition by HVPE onto Au decorated graphitic structures is therefore unprecedented and comparison to previously reported results only superficially possible. Also documented is the coexistence and periodic arrangement of wurtzite and zinc blende structure in InP wires.[85] This scenario was considered, but was ruled out as the observed diffraction patterns do not match this arrangement and the wurtzite structure of InP. The very top of the wire is covered by a cap of Au and In_2O_3 as evident from the EDX line scan presented in Figure 6.7 c). The presence of Au is reminiscent of structures grown by the vapor-liquid-solid (VLS) method.[86] The presence of such large amounts of indium oxide is surprising. It is well known that InP forms a native oxide layer on the surface[87], [88] but the oxide cap has an extent of at least 100 nm thus far exceeding the typically observed of only a few nanometers.

The origin of this oxide cap therefore is likely found during the deposition. It is hypothesized that these large InP rods have residual t-ZnO as a seed and grow out of these residues. This could explain the presence of the oxide cap, which is formed from the residual ZnO through an exchange reaction. In order to further investigate this, intermediate synthesis products could be analyzed to shed light on the growth processes of these structures.

Aside the microrods, regions of Aerographite covered with finely dispersed core-shell particles were found.(cf. Figure 6.8) These particles range in size from around 15 to 50 nm. As strongly magnified STEM-HAADF images reveal, they exhibit a heavy core with a lighter shell, as evident from Z contrast. EDX mapping reveals that the core and shell correspond to Au and indium oxide. Electron diffraction (Figure 6.9) was not entirely conclusive, as the polycrystalline pattern contains matches with a wide range of potential phases. Table 6.1 lists all diffraction maxima from the diffraction pattern in Figure 6.9. Besides matches with Au and graphite, the presence of InP or the previously encountered InPO_4 cannot be excluded. Also, no diffraction

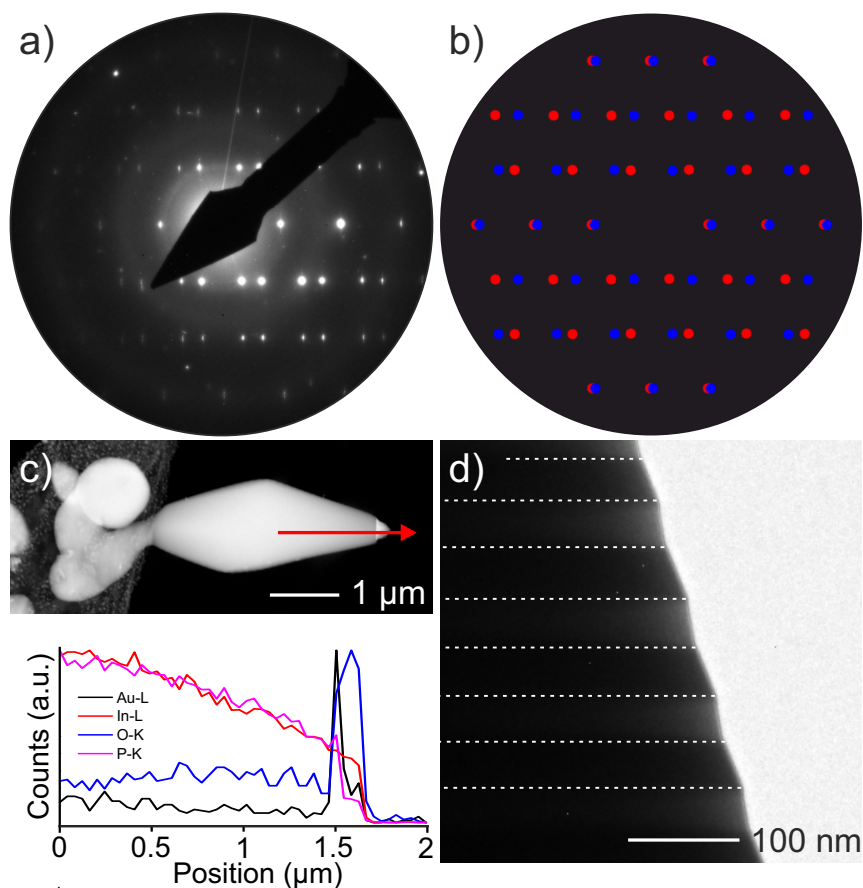


FIGURE 6.7: TEM analysis of InP microstructures. a) SAED pattern recorded near the tip of the microrod showing cubic InP in the zone axis $1\bar{1}0$. b) Superposition of two simulated diffraction patterns. c) Overview image of the InP microrod and EDX linescan recorded along the red arrow. d) Bright field image showcasing the twinning domains of the microrod. Reproduced from Reference [79].

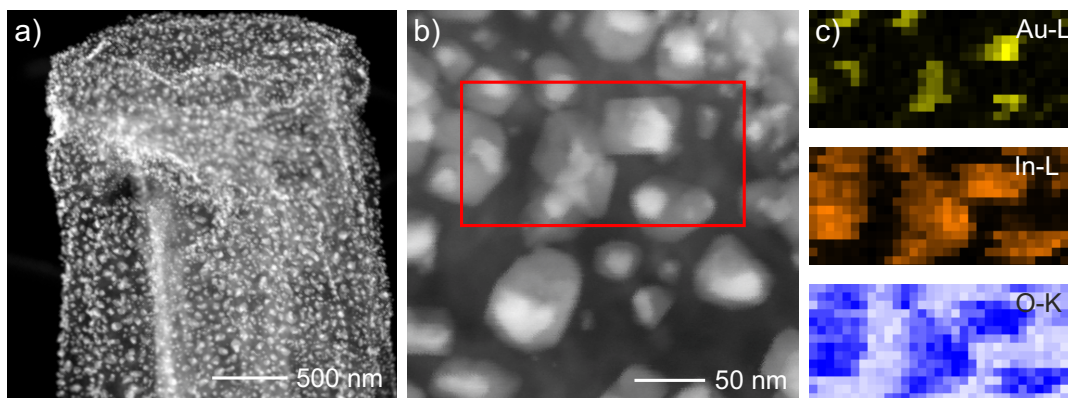


FIGURE 6.8: STEM imaging of In_2O_3 particles with Au cores on Aerographite. a) Overview STEM-HAADF image of an Aerographite tube decorated with particles. b) Close-up image revealing the core-shell character of the particles. c) STEM-EDX maps taken in the area marked by the red rectangle in b). Maps for In and O are nearly congruent, while the Au signal originates from the center of the particles.

maxima from either of the InP phase are missing. What is more, EDX lines of Au-M at 2.120 keV and $\text{P}-\text{K}_\alpha$ at 2.013 keV and $\text{P}-\text{K}_\beta$ at 2.139 keV overlap thus further complicating a clear assignment and leaving the possibility that the particles also contain phosphorous near their core.

In order to resolve issue HRTEM investigations on the particles were made. Figure 6.10 displays the high resolution micrograph alongside an FFT and a superposition of simulated diffraction patterns of Au and In_2O_3 . Simulation and FFT are essentially congruent aside from a number of additional reflections present in the FFT. These reflections are at the position of InP $\bar{3}02$ (coinciding with Au $\bar{1}10$) as well

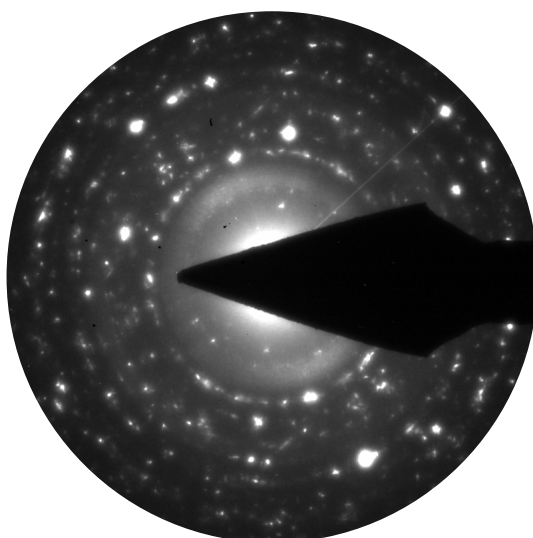


FIGURE 6.9: SAED pattern of In_2O_3 particles with Au cores on Aerographite. Due to the plethora of diffraction maxima no unambiguous assignment is possible. Diffraction maxima and potential matches are listed in Table 6.1.

TABLE 6.1: Overview table of reciprocal distances and potential matches of the InP-Aerographite-AuNP sample. At large reciprocal distances (i.e. small lattice spacings) the low symmetry phases of InPO₄ (Pnma) and In₂O₃ (Ia $\bar{3}$) inherently contain so many tabulated lattice spacings that a comparison with experimentally determined values is futile.

$d_{hkl}(\text{nm}^{-1})$	Au	InP $F\bar{4}3m$	InP $Fm\bar{3}m$	Graphite	InPO ₄ Pnma	In ₂ O ₃ Ia $\bar{3}$
2.40					101	112
3.39		002	111		211	222
3.90			002		301	004
4.17	111				002	114
4.56		022		010	112	233
5.00	002				022	224/134/314
5.52		113	022	012	222	044
6.01		222			501	006
6.46			113	013	div.	div.
7.11	022	004			div.	div.

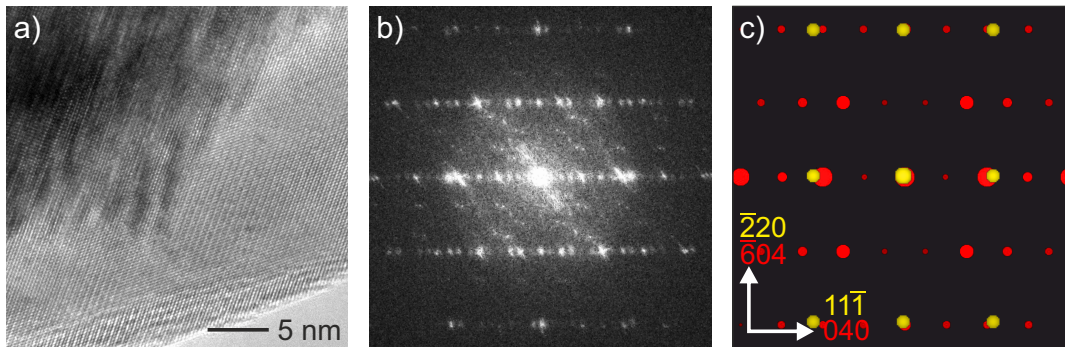


FIGURE 6.10: HRTEM investigation of an In₂O₃ particle with Au core a) HRTEM micrograph of the rim of the particle with the core in the upper left corner of the image. b) FFT from the region marked by a white square in a). c) Superposition of two simulated diffraction patterns of Au (ZA 112) and In₂O₃ (ZA203) matching with the FFT in b).

as InP 030 and 010. Inverse FFT filtering proves that these reflections originate from the region where Au core and In₂O₃ shell overlap.

The fact that Au particles apparently catalyze the formation of In₂O₃ over InP is an unwanted result at first glance. However, as shown in literature In₂O₃ itself is a promising candidate for gas sensing instead of strain sensing. As the space group of In₂O₃ (Ia $\bar{3}$) is centrosymmetric it does not show a piezoelectric effect and is thus non-viable for strain sensing applications. Notably, In₂O₃ based gas sensors are sensitive for CO[89], NO₂[90] and ethanol.[91] The viability of such semiconducting ultra-porous gas sensors will be explored in the next section.

Aside from particles the Au particle assisted synthesis process of InP also resulted in wire shaped products. Figure 6.11 shows that these wires are growing out of particles which in turn are sitting on top of the Aerographite scaffold. EDX analysis proves that these wires are made from In oxide while the particle that they are attached to have appear similar to the previously analyzed In_2O_3 -Au core-shell particles. The diffraction pattern also suggests that the same phases are present even though the morphology is considerably different. A faint high resolution contrast visible in Figure 6.11 c) also proves that not only the particles are crystalline but also the wires attached to them. The lattice spacing of 7.43 \AA could not be assigned to any In oxide or phosphate phase, though. Similar to the previously discussed SAED pattern from an area with predominantly core-shell particles, the SAED pattern cannot unambiguously be assigned to a phase such that the structure of the nanowires cannot be solved.

The growth mechanism of In_2O_3 remains largely unknown. From literature it is known that InP can rapidly oxidize [87], [88], [92] but this process generally takes place above 340°C . Furthermore, the resulting oxide is a mixture of In_2O_3 and P_2O_5 ,

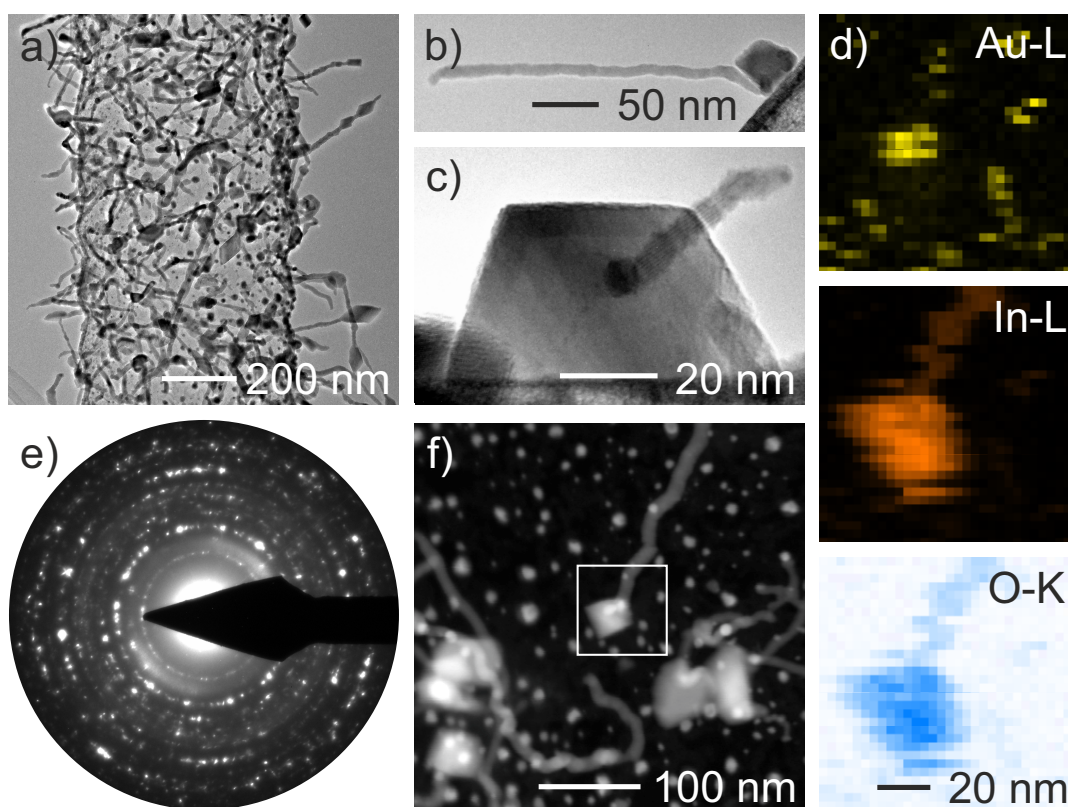


FIGURE 6.11: TEM investigation on In_2O_3 nanowires on Aerographite. a) Bright field TEM image of an Aerographite fragment covered with nanowires and -particles. b) and c) close-ups of wires and particles. d) STEM-EDX elemental maps of Au, In and O. Maps were manually stitched together post acquisition as the drift correction did not work properly. Correlation of the same particle and wire displayed in f) enables this manual drift correction. e) SAED pattern of nanowire covered Aerographite. f) STEM-HAADF image of a region where elemental maps in d) were acquired. Partially reproduced from Reference [79].

the latter of which has never been observed in these samples. In fact, no P containing product was found, such that it seems plausible that no InP was formed and that the In_2O_3 formed directly during the growth process. Potentially responsible for the oxidation of In could be a leakage in the system, thus introducing the oxygen.

While the wires and monolithic InP array are reminiscent of VLS grown structures it is highly questionable whether such a process actually takes place during deposition. The melting point of Au at standard pressure is approximately 1064°C but the substrate was only heated to 650°C . The (solid) Au particles deposited onto the Aerographite can therefore not act as liquid catalyst for VLS growth.

6.2 CdS-aerogel pressure sensor and CdS-Aerographite gas sensor

Similar to InP, CdS is a compound semiconductor. Instead of a typical III-V semiconductor, though, CdS is a II-VI compound.¹ Another similarity is the piezoelectric nature of CdS crystals. While CdS can be exploited for many different of its properties this section shall focus on a pressure sensor utilizing the piezoelectric response of CdS. The sensor was fabricated by sputtering CdS onto a graphene aerogel and afterwards contacting opposite sides of the sensor with silver paste intended to form electrical contacts. The fabrication was conducted by Irina Plesco. TEM samples were prepared by crumbling parts of the sensor onto suitable sample grids.

In a first step the graphene aerogel scaffold material of the sensor with any CdS decoration was analyzed. Unsurprisingly, the structure of the individual sheets of the aerogel matches well with pristine graphite references as depicted in Figure 6.12. There is a slight shortening of reciprocal distances by about 1.7% in the $(\bar{1}20)^*$ direction, though, translating to a slight increase of lattice parameters of the respective plane of the same magnitude in real space. The slight deformation of the basal plane of graphene is likely correlated to its aerogel nature and might be indicative of internal strain because of bending of individual graphene sheets. As the subsequent deposition of CdS is neither intended nor expected to be influenced by this slight expansion this effect is deemed negligible. The morphology of the CdS film as visible in the SEM images in Figure 6.13 is roughly reminiscent of the "cauliflower" structure reported by Vemuri *et al.*[94]. The absence of larger cracks - in between individual "cauliflower florets" - is likely caused by the considerably lower film thickness and hence lower stress in the film. Figure 6.14 depicts the results of TEM investigations of the CdS-aerogel pressure sensor. Large micro-sized flakes of the aerogel scaffold are unevenly covered by polycrystalline CdS with the space group $P6_3mc$ as shown by electron diffraction experiments. The morphology of the CdS film appears rugged and uneven probably because of an influence of the underlying aerogel. Individual CdS grains are of high crystalline quality, though, with no obvious defects of the

¹The II-VI nomenclature is helpful in that it hints towards the similarity with III-V compounds but misleading since the II actually refers to group 12 elements.

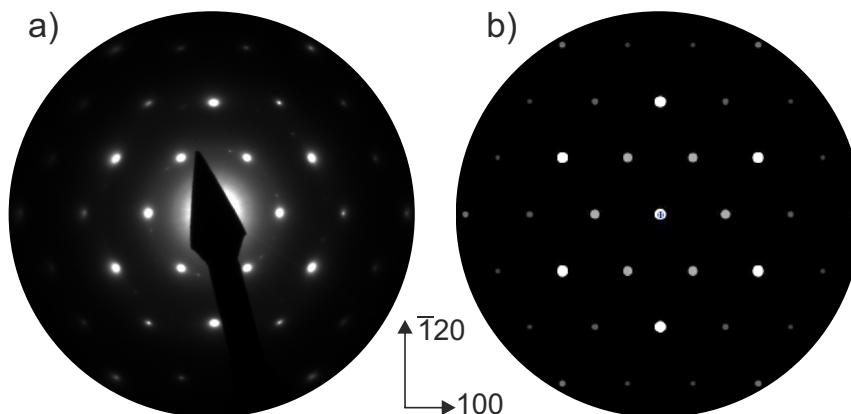


FIGURE 6.12: Diffraction pattern of the aerogel support. a) SAED pattern recorded on the aerogel support without any CdS decoration. b) simulated diffraction pattern of graphite in the zone axis 001. The two patterns match almost perfectly except for a slight distortion of the basal plane of the graphene aerogel.

crystal lattice. Interestingly, electron diffraction showed that the lattice is slightly expanded with respect to the reference data. The composition was determined to be $\text{Cd}_{54}\text{S}_{46}$ and thus slightly S depleted. As no reference sample was available to confirm the experimentally determined composition the margin of error can only be estimated. It is expected, however, that the accuracy of the EDX system and quantification is roughly on the same order of magnitude as the determined non-stoichiometry such that the determined composition is unfortunately not significant. In conjunction with observed lattice parameters the general trend towards Cd-enrichment is generally believable as Cd rich CdS generally exhibits slightly larger lattice parameters.[95]

As previously reported in literature, the stoichiometry of CdS is dependent on sputtering parameters, particularly sputtering power. Investigations on the already previously introduced "cauliflower" CdS films showed that in an intermediate range of sputtering power the films are stoichiometric, above a certain threshold the films become S deficient, though.[94] The threshold power reported in the study by Vemuri *et al.* was 105 W, however, as many different sputtering parameters might govern the resulting CdS, Table 6.2 shows a comparison of experimental parameters by Vemuri

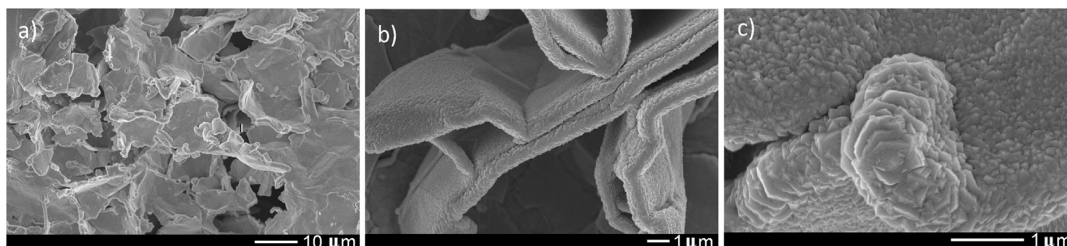


FIGURE 6.13: SEM investigations of the CdS-aerogel pressure sensor from low (a) to high (c) magnification. Reproduced from Reference [93].

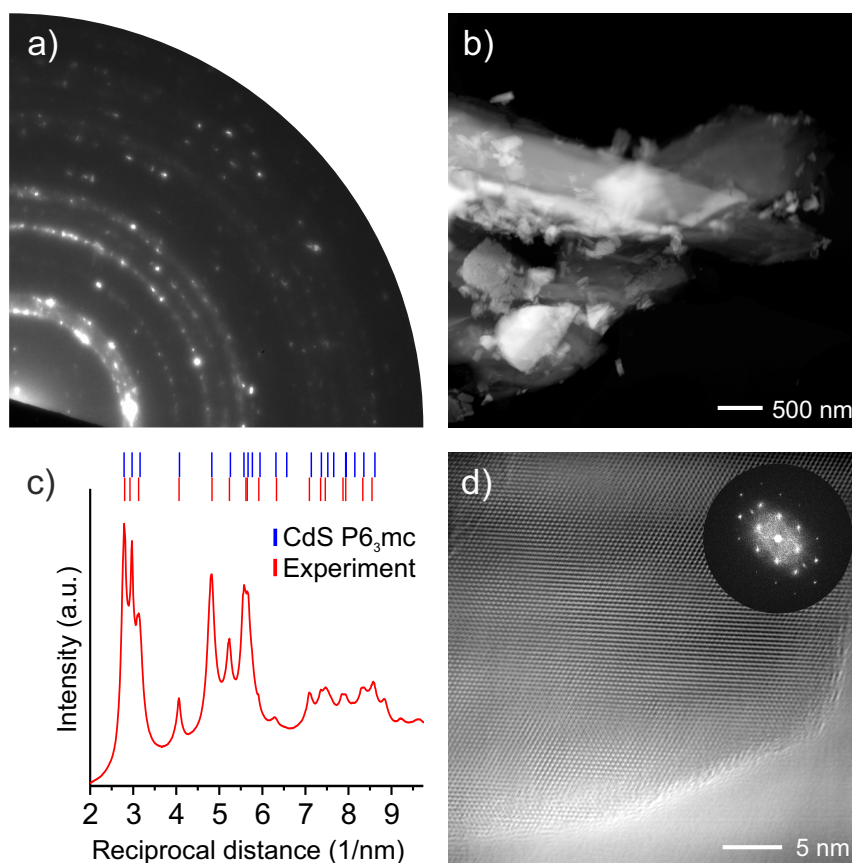


FIGURE 6.14: TEM investigations of the CdS-aerogel pressure sensor. a) SAED pattern showing the polycrystalline character of CdS. b) STEM-HAADF overview image. Several sheets covered with CdS crystals are visible. c) True-to-scale intensity distribution of the SAED pattern in a). Vertical ticks at the top indicate the position of maxima. In comparison to the hexagonal CdS reference (blue) the experimentally determined lattice parameters are slightly increased. d) HRTEM micrograph and FFT (inset) of CdS covered sheet underlining the high crystalline quality of the deposited CdS. Partially reproduced from Reference [93].

and from this study.

Aside the previously mentioned difference in film thickness - which is mainly controlled by sputtering duration which is not expected to influence the stoichiometry - the only major differences is the sputtering power. While a few factors cannot be compared as they are not known, such as the angle between target and substrate as well as the flow of Ar during deposition, the sputtering power used to deposit the CdS films presented in this study, far exceeds the reported threshold power of 105 W above which CdS films were found to be Cd enriched. Vemuri *et al.* do not present a quantitative estimate, but with the reported XPS and EDX spectra it is estimated that the deviation from the ideal stoichiometry is on the same order of magnitude as the stoichiometry of around $\text{Cd}_{54}\text{S}_{46}$ from the CdS reported here. The theory presented by Vemuri *et al.*, that a sputtering power beyond the critical threshold leads to re-evaporation of S adatoms before being chemisorbed seems plausible. The theory could be checked by sputtering onto a heated substrate which should further promote re-evaporation.

TABLE 6.2: Comparison of CdS sputtering parameters between the study by Vemuri[94] and this one. Known fabrication parameters are the type of deposition, sputtering power (P), distance from target to substrate (d_{TS}), Argon pressure during deposition (p_{Ar}), substrate temperature ($T_{substrate}$) and deposited film thickness (d_{film}).

	Vemuri <i>et al.</i>	This study
Type	RF sputtering	RF sputtering
P (W)	105	200
d_{TS} (cm)	8	8
p_{Ar} (10^{-3} mbar)	9.3	7.4
$T_{substrate}$ ($^{\circ}C$)	RT	30
d_{film} (nm)	900	250

Besides CdS deposition onto graphene aerogels, CdS was also deposited onto Aerographite to the effect of producing gas sensors, the results are shown in Figures 6.15 and 6.16. The new scaffold was chosen, because previous studies showed that Aerographite already possesses remarkable gas sensing abilities with a strong sensitivity for CO_2 , NH_3 and H_2 . [96] In order to tune the selectivity towards different gases, increase the sensitivity and improve efficiency, Aerographite scaffolds were chosen. Similar to the deposition onto aerogel, this deposition was done by sputtering stoichiometric targets. The fabrication was conducted by Lidia Ghimpu of the Technical University of Moldova. The exact deposition parameters and other processing steps are a matter of confidentiality and will not be further discussed in this study.

Figure 6.15 shows the TEM analysis of the decorated Aerographite tubes. As apparent from the overview image, the Aerographite scaffold remained intact during the

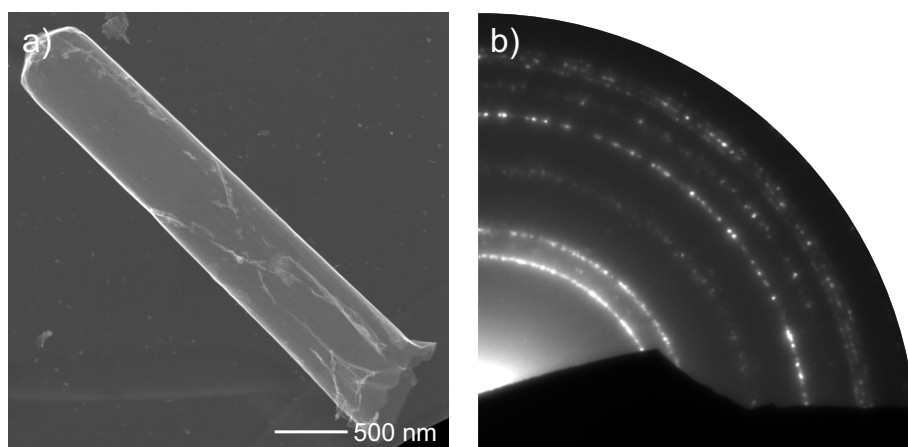


FIGURE 6.15: Overview image and SAED pattern of CdS on Aerographite. a) STEM-HAADF image of an Aerographite tetrapod fragment homogeneously covered with CdS. b) SAED pattern of the fragment in a) showing the phase purity of produced CdS.

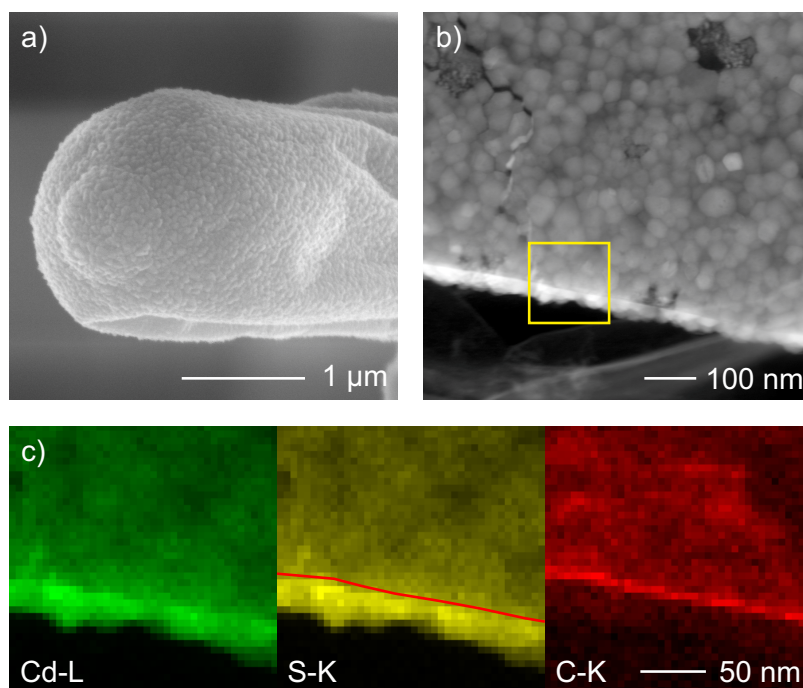


FIGURE 6.16: Edge of CdS covered Aerographite and EDX maps. a) SEM overview image of a CdS covered Aerographite arm. b) STEM-HAADF image of the edge of a CdS covered Aerographite fragment. c) STEM-EDX maps of Cd, S and C acquired at the position of the yellow square in b). CdS nucleated on the outside of Aerographite walls. Red line in the sulfur map shows the position of the carbon wall.

deposition and no anisotropy of the deposition process is apparent from the image. As determined by diffraction experiments, the deposited CdS is a pure phase and crystallized in the space group $P6_3mc$ as was the case for the CdS deposited onto aerogel. Unlike the aerogel-based samples, though, the film appears to be more uniform with a thickness between 20 and 30 nm.

The morphology of the CdS film is much smoother as apparent from SEM micrographs. The general morphology of the underlying scaffold material is well maintained and discernible through the CdS film. The grain size ranges from 20 to 100 nm and the film thickness is only around 25 nm. The STEM-EDX maps taken in proximity to the rim of the tetrapod fragment also prove that CdS is solely deposited on the outside of the Aerographite tubes and no other elements besides Cd, S and C were detectable, which does not exclude the presence of trace elements due to the widely known limitations of EDX detectors. The stoichiometry was determined and found to be around $Cd_{50}S_{50}$ with an error of around 2 at%.

The deposition of CdS therefore worked just as well on aerogels and Aerographite. The sensing properties have been explored and select results are shown in Figure 6.17. Gas sensing properties for CdS are still a matter of investigations, preliminary experiments showed that it is possible to tune the gas sensing properties of Aerographite by CdS deposition by utilizing synergistic effects potentially based on

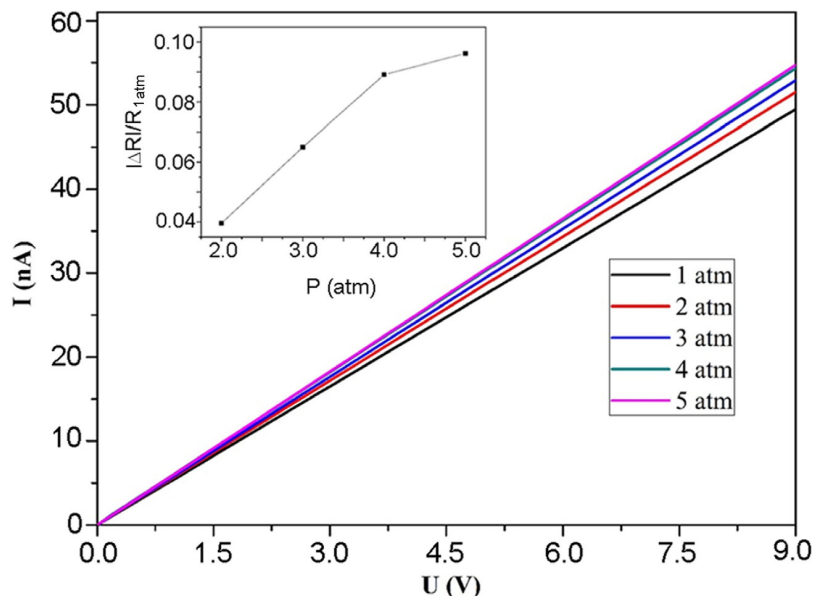


FIGURE 6.17: Sensor properties of CdS-aerogel compound. The graph shows the I-V characteristic of the sensor at different pressures. Inset shows the relative resistance change with respect to standard pressure at different external pressures. Reproduced from Reference [93].

tunable charge transfer between CdS and the Aerographite scaffold.

6.3 CdTe-Aerographite gas sensor

As different semiconducting compounds facilitate different gas responses the sensor introduced in the previous section has been produced analogously with CdTe instead of CdS. CdTe is obviously similar in many aspects to CdS, however, as one of the main parameters governing the gas response is the surface configuration CdTe might be a promising candidate. The deposition of CdTe was also accomplished by magnetron sputtering as in the CdS case.[97]

The first attempts to synthesize CdTe on Aerographite resulted in no digestible result. (cf. Figure 6.18) Depending on the sputtering time, the deposition produced either singular CdTe particles on Aerographite or rough and uneven patches of particles. SEM investigations were futile on these samples, because of the evanescent amount of CdTe. Furthermore, EDX quantification of the particles showed that they contained a large amount of Cl. The composition was determined to be around $\text{Cd}_{32}\text{Te}_{36}\text{Cl}_{31}$. Diffraction and high resolution experiments were conducted to avail, as no crystalline reflections or phase contrast was ever observed. Similar holds true for samples with longer deposition time. Figure 6.18 c) and d) show Aerographite fragments with patches of CdTe. However, even with this considerably larger amount of material, only few reflections were visible in the diffraction pattern, indicating a mostly amorphous sample. This comes as no surprise, given that

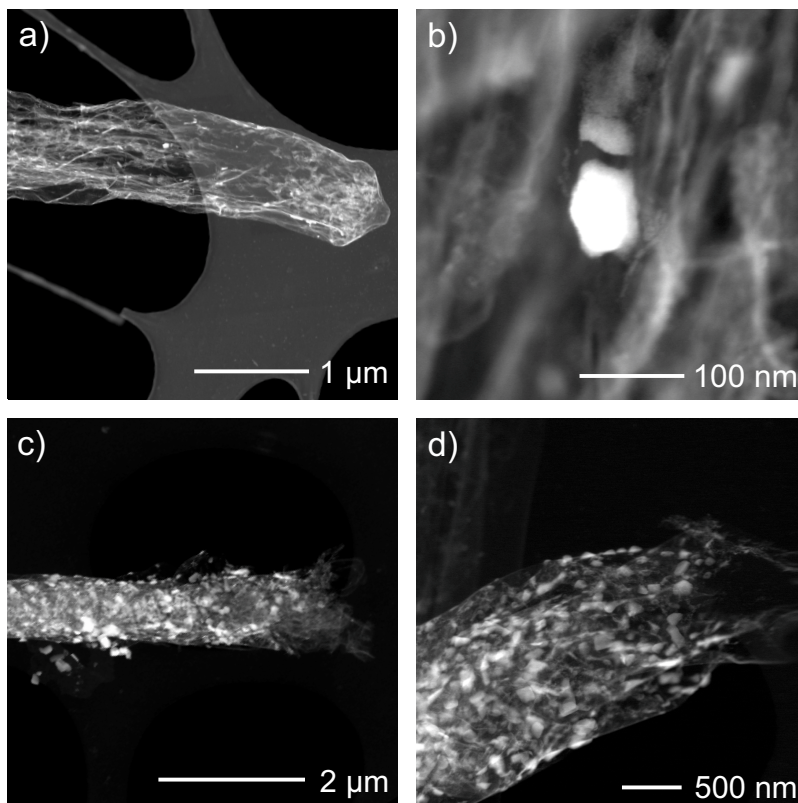


FIGURE 6.18: Initial attempts of CdTe deposition. a) Aerographite fragment with little to no discernible CdTe content. b) Singular CdTe particle. c) Aerographite with considerable CdTe(Cl) content with large non-uniformity. d) Close-up of particles found on fragment in c).

EDX investigations found that the sample also consists of around 31 at% Cl. As details of deposition and post-fabrication treatment are unfortunately confidential, no speculation on the origin of the Cl can be presented.

The next generation of CdTe-Aerographite compounds turned out much more

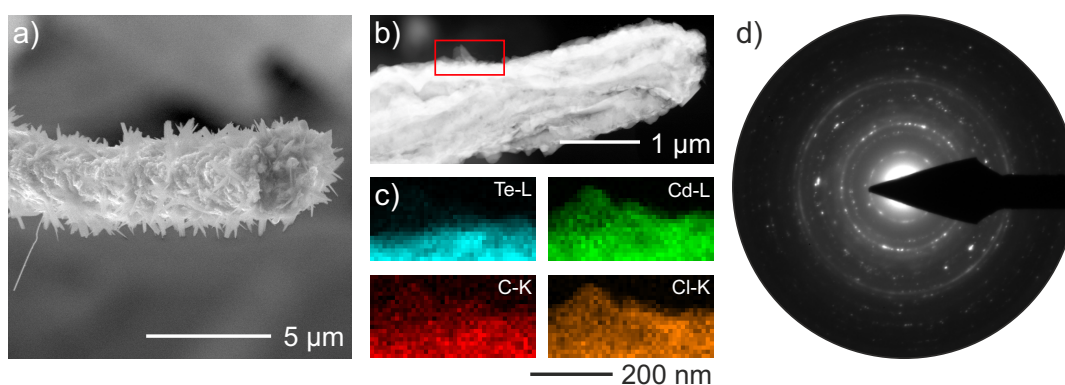


FIGURE 6.19: CdTe-Aerographite *micro-cactus*. a) SEM micrograph an Aerographite structure covered with CdTe with jagged crystals on the surface. b) STEM-HAADF micrograph of a similar fragment. c) STEM-EDX elemental maps recorded in the area marked by a red rectangle in b). d) SAED pattern of CdTe and CdCl₂.

promising. Figure 6.19 shows that the deposition resulted in what looks a micro-sized "cactus" with jagged slices sticking out of the Aerographite arm. As these slices seem to contain prominent facets they are expected to be crystalline. In order to further investigate these structures they were transferred to the TEM. During the deposition, many of the slices seem to have fallen off the substrate material, as only few Aerographite arms were found with such morphology observed in SEM. This hints towards a very loose attachment. Nonetheless, some regions similar to the morphology observed in the SEM were also found in TEM (cf. Figure 6.19 b) such that they could be analyzed in more detail. STEM-EDX mapping shows that the main body of the sample contains Te, Cd, Cl and the C scaffold material. Te, however, is missing from the previously described slices. In conjunction with the subsequent diffraction analysis, both CdTe (sg. $F\bar{4}3m$ zinc blende structure) and CdCl₂ (sg. $R\bar{3}m$) were identified. This obviously implies that CdTe was indeed successfully synthesized on Aerographite, however, the Cl contamination was not fixed in these samples and hence the CdCl₂ slices on top. Accordingly, the synthe-

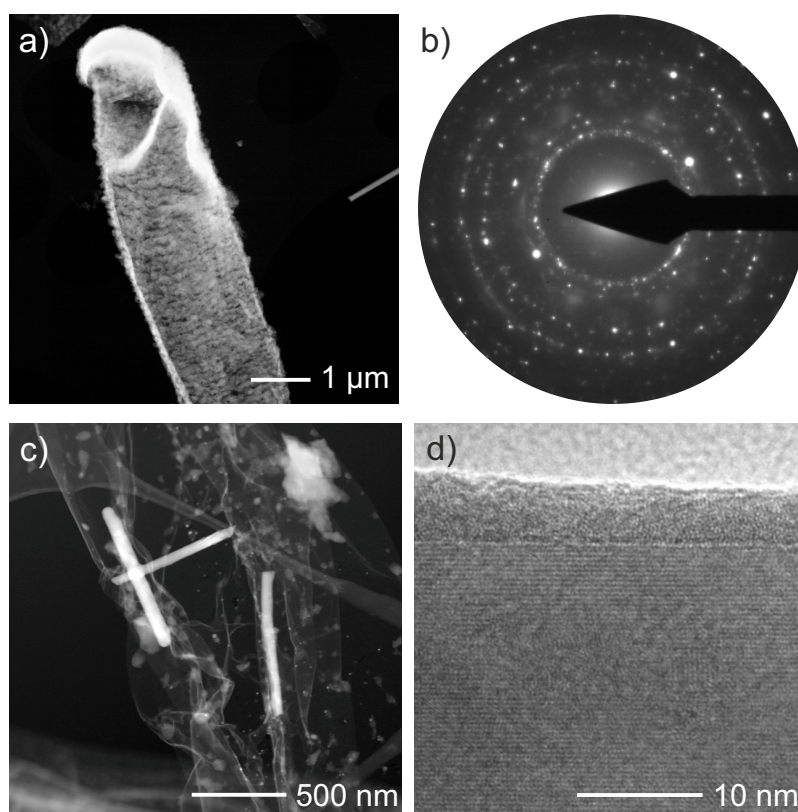


FIGURE 6.20: Various CdTe structures on Aerographite. a) STEM-HAADF micrograph of an Aerographite fragment covered with CdTe and CdCl₂. b) SAED pattern confirming the constituent phases of a), specifically CdTe (sg. $F\bar{4}3m$) and CdCl₂ (sg. $R\bar{3}m$). c) Needles produced during the same synthesis process. d) HRTEM micrograph of one of the needles in c) showing the 010 lattice spacing of Te.

sis process was adjusted again, see also Figure 6.20. While these samples did not

show prominent morphologies such as the previously shown "cactus" they unfortunately still contained a fraction of CdCl_2 as evident from diffraction experiments. Oddly, even though the deposition was done by sputtering from a stoichiometric CdTe target, apparently metallic Te wires were found. These wires seem to be scattered randomly across the Aerographite scaffold. Some of them were found to be amorphous while others were proven by HRTEM analysis to be essentially single crystalline with an amorphous shell of a few nanometers. While this might at first seem reminiscent of the previously reported phosphate wires in the InP-sensor case, these wires did neither show any sign of oxidation nor a sign of chloride formation. Instead, EDX analysis proves that these wires consist of around 90 at% Te and 10 at% Cd which is also reflected in the Te (010) lattice spacing being visible in the HRTEM micrograph.

Finally, it was possible to tune the deposition in such a way, that no Cl content was left in the samples. A cross-section of a wall, exposed through post-deposition fracture, reveals that the CdTe grain growth closely resembles *zone T* of the structure zone model proposed by Barna and Adamik[98], i.e. a higher density of grains with seemingly random orientations near the substrate and larger columnar grains

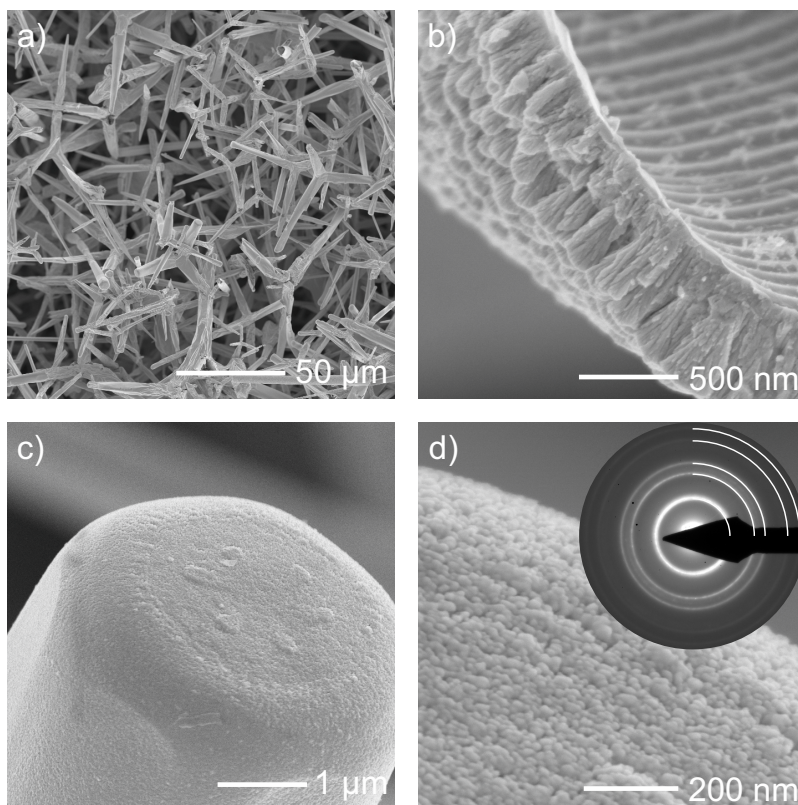


FIGURE 6.21: SEM and TEM investigations of CdTe on Aerographite. a) SEM overview image of the produced CdTe-Aerographite compound. b) Close-up of a fractured fragment showing the CdTe wall thickness of around 500 nm. c) Magnified view of a tetrapod cap highlighting the extremely smooth coverage. d) Detailed view of the grain structure revealing the lateral grain size of around 10-35 nm. Inset shows the single phase SAED pattern of CdTe. Reproduced from Reference [97].

closer to the top of the film. *Zone T* is characterized by these authors as "*competitive growth of differently oriented neighbouring crystals*" with an intermediate number of seeds for crystal growth and not enough thermal energy for grain boundary movement. Accordingly, by adjusting the substrate temperature, the morphology of these films should be tunable from the lower-temperature *Zone I* of this model - finely dispersed grains with a high nucleation density - to the higher-temperature *Zone II* with a lower nucleation density but enough thermal energy for grain boundary movement, such that large columnar grains with similar orientation evolve. As previously shown in literature, the gas sensing properties strongly depend on crystal orientation, mainly due to different surface configurations and energies, such that this opens up a pathway for future tuning of these devices.[99], [100] As also presented in the publication by the author of this thesis [97], the I-V characteristics and gas sensing properties of these CdTe-based devices have been explored. While the I-V characteristic is linear in the small-signal range up to 1 V the correlation between gas concentration, e.g. of NH₃ and response was found to be non-linear. Obviously, this does not constitute a memsensor in itself, a serial combination of this sensor with a memristor could produce a memsensor. Alas, this does present a larger effort than having it combined in one single device, however, building a memsensor in such a way possibly leaves more degrees of freedom to adjust, such that the selectivity of the sensor and the memristive characteristics could be tuned independently.

Chapter 7

Conclusion and Outlook

In the scope of this study, several material systems have been analysed by transmission electron microscopy. All samples are related to the framework of memristive switching and belong to one of three groups:

1. Double barrier memristors,
2. Nanoparticle-based memristor,
3. Memsensors.

The first topical area deals with double barrier memristive devices. The results conclusively showed that deposition of an oxide stack between two metal electrodes can lead to unwanted side effects. Specifically, the deposition of Nb oxide by reactive sputtering can cause oxidation of subjacent layers. A supposedly partially oxidized Al layer turned out to be completely oxidized and even the underlying bottom electrode showed significant oxidation reaching several nanometers into the metal layer. The oxidation state of all oxides was determined by EELS. Identification by structural analysis was not possible as all oxides were amorphous. The Schottky barrier forming Nb oxide was determined to exhibit an oxidation state between +4 and +5, thus forming an insulating layer. The involuntarily oxidized Nb bottom electrode was found to have an oxidation state of +2, thus forming a conducting layer. Thus, the oxidation of the bottom electrode does likely not impede memristive switching as also apparent from electrical characterization. The Al oxide tunnel barrier in between the two Nb oxide layers closely resembled stoichiometric Al_2O_3 . At least two different defects were found in the electronic structure of the Al oxide. A small pre-peak some 6 eV before the O-K edge and in later samples a much more intense pre-peak some 9 eV before the O-K edge. The former was associated with oxygen vacancies in Al oxide. The origin of the latter could not be clarified unequivocally. Possible explanations for the pre-peak are the presence of hydroxides or strong local reduction of the oxide due to the intense electron irradiation of the electron beam. As experiments in other subprojects of the overarching research unit showed that the Schottky barrier - i.e. the Nb oxide - is responsible for memristive switching and not the tunnel barrier - i.e. the Al oxide - the direct influence of these defects on the electrical characteristics is deemed small. Instead, the defects might influence the Schottky barrier by moving towards or away from the Al oxide/Nb

oxide interface. Furthermore, they might act as a vacancy reservoir supplying or accepting oxygen vacancies to the neighboring Nb oxide and thus enabling memristive switching through modification of the Schottky barrier. The results shed light on the inner workings of DBM devices and suggest that the tunnel barrier might play a more important role than what was suggested by electrical characterization. Future investigations could focus on spectroscopic investigations of the Schottky barrier oxide. Nano-beam electron diffraction can uncover the local pair distribution function of amorphous materials and could lead to further insight into the oxide materials. The origin of electronic defects in the devices should also be investigated. Other potential paths of investigations are valence EELS or photoluminescence investigations for band-gap determination. Both possibilities require dedicated and rarely available equipment, though.

Secondly, memristors based on metal nanoparticles embedded in a dielectric matrix were characterized. The deposition characteristics of a custom Haberland-type gas aggregation source were analyzed by TEM. The investigations showed that mono- and bimetallic particles can be produced. Their properties - size distribution, composition and number density - can be influenced by sputter parameters. The cosputtering of particles with a dielectric matrix material such as Si or Si oxide was also shown to be feasible. Tomographic analysis highlighted the successful deposition of a particle gradient embedded within a matrix. However, the formation mechanism of these particles is largely unknown as are the physical processes in the source itself. Accordingly, unintuitive results have been recorded where expected parameters - such as sputter time and resulting particle density - did not show correlation. An inherent problem is the reliability of results, as even small deviations in sample position during deposition or area of investigation in the microscope might have a huge influence on the observed results. A standardized test procedure and the analysis of a large number of samples might alleviate this problem and ensure statistical significance. Whether non-alloy particles - such as core-shell or Janus particles - are feasible or might even offer advantages over alloy particles will be analyzed by the electrical characterization of these devices. TEM investigations can support these development analogous to the results presented in this study. Furthermore, nanoparticle based memristors are predestined for *ex situ* investigations. In the scope of the master thesis by Ole Gronenberg[101] dedicated TEM grids have been developed that allow the deposition of devices with horizontal alignment. These grids enable pre- and post-operation analysis and thus allow inferring the mechanism of memristive switching. Considerable advances for *in situ* investigations have been made by Krishna Kanth Neelisetty at the Karlsruhe Institute of Technology within the scope of his dissertation and publications. However, he also pointed out the inherent and essentially inevitable flaws of e-beam based *in situ* electrical characterisation of such devices.

Finally, memsensors based on several semiconductor composite materials have been analyzed. The deposition of InP, CdS and CdTe onto various carbon scaffold materials was hindered by different unforeseen effects, as uncovered by electron microscopy investigations. InP deposition was accomplished through an HVPE process which, when using a ZnO substrate, resulted in the formation of at least two different phosphate phases. As this formation was credited to the scaffold material itself, ZnO was discarded for further HVPE deposition attempts. Instead, the aforementioned carbon scaffold substrate was used. The deposition onto carbon-nanotube-tubes remained just as unsuccessful, likely because the rugged surface of the CNTTs provided no sufficient holdfast for InP formation. Only few isolated particles were observed on the outside and a number of giant InP particles on the inside of CNTTs were found. As this thwarts all advantages that these scaffold materials inherently have - namely high specific surface and a large surface to volume ratio - this substrate, too, was discarded. Finally, InP was deposited onto Aerographite substrates. Even though this did not result in a homogeneous coverage of Aerographite tubes but rather in the pronounced growth of microsized wires with large aspect ratios, these turned out to be suitable strain sensors. Various defects were found in these wires, namely In segregation and lenticular structural defects, but they were not expected to affect function in any way. In an effort to promote the smooth coverage of Aerographite with an InP film or InP particles, the scaffold was covered in Au nanodots before InP deposition. However, this did not promote a homogeneous InP coverage, and instead mainly resulted in In_2O_3 particles with a Au core. While the exact formation mechanism remains a mystery small scale leaks in the deposition chamber might be the most probable explanation.

The deposition of CdS onto Aerographite and an aerogel on the other hand worked as intended without much fine-tuning of the deposition process. Oddly, though, the analogous deposition of CdTe onto Aerographite resulted in the formation of various unwanted products, mainly CdCl_2 . And while the deposition of CdS resulted in smooth films which are ideal for gas and pressure sensing, CdTe sputtering lead to various different morphologies before the deposition process could be tuned to produce homogeneous films. The I-V characteristics and sensing properties of these structures were explored. Indeed, InP-Aerographite hybrids show a non-linear I-V curve much like a memristor. However, while the sensing function has been well explored, the memristive aspect is still a matter of ongoing investigations. Preliminary investigations showed that some of the devices show a memristor-like I-V characteristic, though, thus paving the way for further research.

Appendix A

Publications

As first author

- [1] I. Plesco, J. Strobel, F. Schütt, C. Himcinschi, N. B. Sedrine, T. Monteiro, M. R. Correia, L. Gorceac, B. Cinic, V. Ursaki, J. Marx, B. Fiedler, Y. K. Mishra, L. Kienle, R. Adelung, and I. Tiginyanu, "Hierarchical Aerographite 3d flexible networks hybridized by InP micro/nanostructures for strain sensor applications", *Scientific Reports*, vol. 8, no. 1, p. 13 880, 2018.
- [2] J. Strobel, L. Ghimpu, V. Postica, O. Lupan, M. Zapf, S. Schönherr, R. Röder, C. Ronning, F. Schütt, Y. K. Mishra, I. Tiginyanu, R. Adelung, J. Marx, B. Fiedler, and L. Kienle, "Improving gas sensing by CdTe decoration of individual aerographite microtubes", *Nanotechnology*, 2018.
- [3] J. Strobel, M. Hansen, S. Dirkmann, K. K. Neelisetty, M. Ziegler, G. Habersfehlner, R. Popescu, G. Kothleitner, V. S. K. Chakravadhanula, C. Kübel, H. Kohlstedt, T. Mussenbrock, and L. Kienle, "In depth nano spectroscopic analysis on homogeneously switching double barrier memristive devices", *Journal of Applied Physics*, vol. 121, no. 24, p. 245 307, 2017.
- [4] T. Dankwort, J. Strobel, C. Chluba, W. Ge, V. Duppel, M. Wuttig, E. Quandt, and L. Kienle, "Martensite adaption through epitaxial nano transition layers in TiNiCu shape memory alloys", *Journal of Applied Crystallography*, vol. 49, no. 3, pp. 1009–1015, 2016.
- [5] J. Strobel, K. K. Neelisetty, V. S. K. Chakravadhanula, and L. Kienle, "Transmission Electron Microscopy on Memristive Devices: An Overview", *Applied Microscopy*, vol. 46, no. 4, pp. 206–216, 2016.

As co-author

- [1] V. Postica, A. Vahl, J. Strobel, D. Santos-Carballal, O. Lupan, A. Cadi-Essadek, N. H. d. Leeuw, F. Schütt, O. Polonskyi, T. Strunskus, M. Baum, L. Kienle, R. Adelung, and F. Faupel, "Tuning doping and surface functionalization of columnar oxide films for volatile organic compound sensing: Experiments and theory", *Journal of Materials Chemistry A*, 2018.
- [2] I. Plesco, M. Dragoman, J. Strobel, L. Ghimpu, F. Schütt, A. Dinescu, V. Ursaki, L. Kienle, R. Adelung, and I. Tiginyanu, "Flexible pressure sensor based on graphene aerogel microstructures functionalized with CdS nanocrystalline thin film", *Superlattices and Microstructures*, vol. 117, pp. 418–422, 2018.
- [3] S. Homaeigohar, T. Strunskus, J. Strobel, L. Kienle, and M. Elbahri, "A Flexible Oxygenated Carbographite Nanofilamentous Buckypaper as an Amphiphilic Membrane", *Advanced Materials Interfaces*, vol. 5, no. 8, p. 1 800 001, 2018.
- [4] A. Vahl, J. Strobel, W. Reichstein, O. Polonskyi, T. Strunskus, L. Kienle, and F. Faupel, "Single target sputter deposition of alloy nanoparticles with adjustable composition via a gas aggregation cluster source", *Nanotechnology*, vol. 28, no. 17, p. 175 703, 2017.
- [5] E. L. Silva, Y. K. Mishra, A. J. S. Fernandes, R. F. Silva, J. Strobel, L. Kienle, R. Adelung, F. J. Oliveira, and M. L. Zheludkevich, "Direct Synthesis of Electrowettable Carbon Nanowall–Diamond Hybrid Materials from Sacrificial Ceramic Templates Using HFCVD", *Advanced Materials Interfaces*, p. 1 700 019, 2017.
- [6] C. Chluba, W. Ge, R. L. d. Miranda, J. Strobel, L. Kienle, E. Quandt, and M. Wuttig, "Ultralow-fatigue shape memory alloy films", *Science*, vol. 348, no. 6238, pp. 1004–1007, 2015.
- [7] V. Hrkac, E. Lage, G. Köppel, J. Strobel, J. McCord, E. Quandt, D. Meyners, and L. Kienle, "Amorphous FeCoSiB for exchange bias coupled and decoupled magnetoelectric multilayer systems: Real-structure and magnetic properties", *Journal of Applied Physics*, vol. 116, no. 13, p. 134 302, 2014.

Bibliography

- [1] N. M. Nasrabadi, "Pattern Recognition and Machine Learning", *Journal of Electronic Imaging*, vol. 16, no. 4, p. 049 901, 2007.
- [2] W. Pedrycz, *Granular Computing: Analysis and Design of Intelligent Systems*. CRC Press, 2016.
- [3] C. M. Bishop and G. Hinton, *Neural Networks for Pattern Recognition*. Oxford: Clarendon Press, 1995.
- [4] B. D. Ripley, *Pattern Recognition and Neural Networks*. 1996.
- [5] S. Samarasinghe, *Neural Networks for Applied Sciences and Engineering: From Fundamentals to Complex Pattern Recognition*. Auerbach Publications, 2016.
- [6] Y. Pao, *Adaptive pattern recognition and neural networks*. 1989.
- [7] I. Goodfellow, Y. Bengio, and A. Courville, *Deep Learning*, ser. Adaptive Computation and Machine Learning. Boston, MA: MIT Press, 2016.
- [8] Y. LeCun, C. Cortes, and C. Burges, *MNIST handwritten digit database*, Yann LeCun, Corinna Cortes and Chris Burges.
- [9] M. M. Waldrop, "The chips are down for Moore's law", *Nature News*, vol. 530, no. 7589, p. 144, 2016.
- [10] D. Drubach, *The Brain Explained*. Pearson, 1999.
- [11] S. M. Platek, J. P. Keenan, and T. K. Shackelford, Eds., *Evolutionary Cognitive Neuroscience*. Cambridge, Massachusetts: MIT Press, 2007.
- [12] D. A. Drachman, "Do we have brain to spare?", *Neurology*, vol. 64, no. 12, pp. 2004–2005, 2005.
- [13] H. H. Goldstine, *The Computer from Pascal to von Neumann*. Princeton University Press, 2008.
- [14] J. Carballo, W. J. Chan, P. A. Gargini, A. B. Kahng, and S. Nath, "ITRS 2.0: Toward a re-framing of the Semiconductor Technology Roadmap", *2014 IEEE 32nd International Conference on Computer Design (ICCD)*, pp. 139–146, 2014.
- [15] T. Hasegawa, K. Terabe, T. Tsuruoka, and M. Aono, "Atomic Switch: Atom/Ion Movement Controlled Devices for Beyond Von-Neumann Computers", *Advanced Materials*, vol. 24, no. 2, pp. 252–267, 2012.
- [16] P. Mazumder, S. Mo Kang, and R. Waser, "Memristors: Devices, Models and Applications", *Proceedings of the IEEE*, vol. 100, no. 6, pp. 1911–1919, 2012.

- [17] L. Chua, "Memristor-The missing circuit element", *IEEE Transactions on Circuit Theory*, vol. 18, no. 5, pp. 507–519, 1971.
- [18] Y. Li, J. Chu, W. Duan, G. Cai, X. Fan, X. Wang, G. Wang, and Y. Pei, "Analog and Digital Bipolar Resistive Switching in Solution-Combustion-Processed NiO Memristor", *ACS Applied Materials & Interfaces*, 2018.
- [19] D. B. Strukov, G. S. Snider, D. R. Stewart, and R. S. Williams, "The missing memristor found", *Nature*, vol. 453, no. 7191, pp. 80–83, 2008.
- [20] Y. Aoki, C. Wiemann, V. Feyer, H.-S. Kim, C. M. Schneider, H. Ill-Yoo, and M. Martin, "Bulk mixed ion electron conduction in amorphous gallium oxide causes memristive behaviour", *Nature Communications*, vol. 5, p. 3473, 2014.
- [21] H. Föll, *Einführung in die Materialwissenschaft II*, Hyperscript.
- [22] M. Hansen, M. Ziegler, L. Kolberg, R. Soni, S. Dirkmann, T. Mussenbrock, and H. Kohlstedt, "A double barrier memristive device", *Scientific Reports*, vol. 5, p. 13753, 2015.
- [23] I. Valov, R. Waser, J. R. Jameson, and M. N. Kozicki, "Electrochemical metalization memories—fundamentals, applications, prospects", *Nanotechnology*, vol. 22, no. 25, p. 254003, 2011.
- [24] S. H. Jo, T. Chang, I. Ebong, B. B. Bhadviya, P. Mazumder, and W. Lu, "Nanoscale Memristor Device as Synapse in Neuromorphic Systems", 2010.
- [25] L. Yang, H. Lin, Z. Zhang, L. Cheng, S. Ye, and M. Shao, "Gas sensing of tellurium-modified silicon nanowires to ammonia and propylamine", *Sensors and Actuators B: Chemical*, vol. 177, pp. 260–264, 2013.
- [26] E. Llobet, "Gas sensors using carbon nanomaterials: A review", *Sensors and Actuators B: Chemical*, A Special Issue in Honour of Professor A. D'Amico, vol. 179, pp. 32–45, 2013.
- [27] H. Winterfeld, M. Ziegler, H. Hanssen, D. Friedrich, W. Benecke, and H. Kohlstedt, "Technology and electrical characterization of MemFlash cells for neuromorphic applications", *Journal of Physics D: Applied Physics*, vol. 51, no. 32, p. 324003, 2018.
- [28] N. Himmel, M. Ziegler, H. Mähne, S. Thiem, H. Winterfeld, and H. Kohlstedt, "Memristive device based on a depletion-type SONOS field effect transistor", *Semiconductor Science and Technology*, vol. 32, no. 6, 06LT01, 2017.
- [29] D. B. Williams and C. B. Carter, *Transmission Electron Microscopy: A Textbook for Materials Science*, 2nd ed. Springer US, 2009.
- [30] L. Reimer and H. Kohl, *Transmission Electron Microscopy: Physics of Image Formation*, 5th ed., ser. Springer Series in Optical Sciences. New York: Springer-Verlag, 2008.
- [31] S. J. Pennycook and P. D. Nellist, Eds., *Scanning Transmission Electron Microscopy*. New York: Springer Science & Business Media, 2011.

- [32] R. F. Egerton, *Electron Energy-Loss Spectroscopy in the Electron Microscope*. Springer Science & Business Media, 2011, Google-Books-ID: C8OZsABSk2sC.
- [33] S. M. Schwarz, B. W. Kempshall, L. A. Giannuzzi¹, and M. R. McCartney, "Avoiding the Curtaining Effect: Backside Milling by FIB INLO", *Microscopy and Microanalysis*, vol. 9, no. S02, pp. 116–117, 2003.
- [34] J. Mayer, L. A. Giannuzzi, T. Kamino, and J. Michael, "TEM Sample Preparation and FIB-Induced Damage", *MRS Bulletin*, vol. 32, no. 5, pp. 400–407, 2007.
- [35] L. A. Giannuzzi and F. A. Stevie, "A review of focused ion beam milling techniques for TEM specimen preparation", *Micron*, vol. 30, no. 3, pp. 197–204, 1999.
- [36] A. Aitkaliyeva, J. W. Madden, B. D. Miller, J. I. Cole, and J. Gan, "Sample preparation artifacts in nuclear materials and mitigation strategies", *Microscopy and Microanalysis*, vol. 21, no. S3, pp. 999–1000, 2015.
- [37] H.-J. Kang, J. H. Kim, J. W. Oh, T. S. Back, and H. J. Kim, "Ultra-thin TEM Sample Preparation with Advanced Backside FIB Milling Method", *Microscopy and Microanalysis*, vol. 16, no. S2, pp. 170–171, 2010.
- [38] J. Lammer, J. Kraxner, and W. Grogger, "Experimental Determination of the Solid Angle of EDXS Detectors", in *European Microscopy Congress 2016: Proceedings*, American Cancer Society, 2016, pp. 943–944.
- [39] J. Lammer, J. Kraxner, G. Haberfehlner, G. Kothleitner, and W. Grogger, "How sample holder geometries influence the quantification of X-ray spectra", in *Book of Abstracts*, Rovinj, Croatia: Ruđer Bošković Institute and Croatian Microscopy Society, 2017, pp. 152–153.
- [40] M. O. Krause, "Atomic radiative and radiationless yields for K and L shells", *Journal of Physical and Chemical Reference Data*, vol. 8, no. 2, pp. 307–327, 1979.
- [41] T. Malis, S. C. Cheng, and R. F. Egerton, "EELS log-ratio technique for specimen-thickness measurement in the TEM", *Journal of Electron Microscopy Technique*, vol. 8, no. 2, pp. 193–200, 1988.
- [42] D. J. Economou, "Modeling and simulation of plasma etching reactors for microelectronics", *Thin Solid Films*, vol. 365, no. 2, pp. 348–367, 2000.
- [43] D. Bach, "EELS investigations of stoichiometric niobium oxides and niobium-based capacitors", PhD thesis, Universität Karlsruhe, Karlsruhe, 2009.
- [44] J. Strobel, M. Hansen, S. Dirkmann, K. K. Neelisetty, M. Ziegler, G. Haberfehlner, R. Popescu, G. Kothleitner, V. S. K. Chakravadhanula, C. Kübel, H. Kohlstedt, T. Mussenbrock, and L. Kienle, "In depth nano spectroscopic analysis on homogeneously switching double barrier memristive devices", *Journal of Applied Physics*, vol. 121, no. 24, p. 245307, 2017.

- [45] N. Jiang and J. C. H. Spence, "Interpretation of Oxygen K pre-edge peak in complex oxides", *Ultramicroscopy*, vol. 106, no. 3, pp. 215–219, 2006.
- [46] M. Klimenkov, A. Möslang, and R. Lindau, "EELS analysis of complex precipitates in PM 2000 steel", *The European Physical Journal Applied Physics*, vol. 42, no. 3, pp. 293–303, 2008.
- [47] J. Bruley, R. Brydson, H. Müllejans, J. Mayer, G. Gutekunst, W. Mader, D. Knauss, and M. Rühle, "Investigations of the chemistry and bonding at niobium-sapphire interfaces", *Journal of Materials Research*, vol. 9, no. 10, pp. 2574–2583, 1994.
- [48] M. L. Knotek and P. J. Feibelman, "Ion Desorption by Core-Hole Auger Decay", *Physical Review Letters*, vol. 40, no. 14, pp. 964–967, 1978.
- [49] S. Nigo, M. Kubota, Y. Harada, T. Hirayama, S. Kato, H. Kitazawa, and G. Kido, "Conduction band caused by oxygen vacancies in aluminum oxide for resistance random access memory", *Journal of Applied Physics*, vol. 112, no. 3, p. 033711, 2012.
- [50] K. H. Johnson and S. V. Pepper, "Molecular-orbital model for metal-sapphire interfacial strength", *Journal of Applied Physics*, vol. 53, no. 10, pp. 6634–6637, 1982.
- [51] D. Liu and J. Robertson, "Oxygen vacancy levels and interfaces of Al₂O₃", *Microelectronic Engineering*, INFOS 2009, vol. 86, no. 7–9, pp. 1668–1671, 2009.
- [52] H. Momida, S. Nigo, G. Kido, and T. Ohno, "Effect of vacancy-type oxygen deficiency on electronic structure in amorphous alumina", *Applied Physics Letters*, vol. 98, no. 4, p. 042102, 2011.
- [53] J. A. Tossell, "The electronic structures of Mg, Al and Si in octahedral coordination with oxygen from SCF X MO calculations", *Journal of Physics and Chemistry of Solids*, vol. 36, no. 11, pp. 1273–1280, 1975.
- [54] J. H. V. Vleck, "The Puzzle of Rare-earth Spectra in Solids.", *The Journal of Physical Chemistry*, vol. 41, no. 1, pp. 67–80, 1937.
- [55] B. Fromme, *d-d Excitations in Transition-Metal Oxides: A Spin-Polarized Electron Energy-Loss Spectroscopy (SPEELS) Study*, ser. Springer Tracts in Modern Physics. Berlin Heidelberg: Springer-Verlag, 2001.
- [56] D. Bouchet and C. Colliex, "Experimental study of ELNES at grain boundaries in alumina: Intergranular radiation damage effects on Al-L23 and O-K edges", *Ultramicroscopy*, vol. 96, no. 2, pp. 139–152, 2003.
- [57] C. Scheu, G. Dehm, M. Rühle, and R. Brydson, "Electron-energy-loss spectroscopy studies of Cu–Al₂O₃ interfaces grown by molecular beam epitaxy", *Philosophical Magazine A*, vol. 78, no. 2, pp. 439–465, 1998.

- [58] C. Århammar, A. Pietzsch, N. Bock, E. Holmström, C. M. Araujo, J. Gråsjö, S. Zhao, S. Green, T. Peery, F. Hennies, S. Amerioun, A. Föhlisch, J. Schlappa, T. Schmitt, V. N. Strocov, G. A. Niklasson, D. C. Wallace, J.-E. Rubensson, B. Johansson, and R. Ahuja, "Unveiling the complex electronic structure of amorphous metal oxides", *Proceedings of the National Academy of Sciences*, 2011.
- [59] I. Levin, A. Berner, C. Scheu, H. Muellejans, and D. G. Brandon, "Electron Energy-Loss Near-Edge Structure of Alumina Polymorphs", in *Modern Developments and Applications in Microbeam Analysis*, G. Love, W. A. P. Nicholson, and A. Armigliato, Eds., ser. Mikrochimica Acta Supplement, Springer Vienna, 1998, pp. 93–96.
- [60] B. Winkler, M. Avalos-Borja, V. Milman, A. Perlov, C. J. Pickard, and J. R. Yates, "Oxygen K-edge electron energy loss spectra of hydrous and anhydrous compounds", *Journal of Physics: Condensed Matter*, vol. 25, no. 48, p. 485401, 2013.
- [61] Y. Huttel, *GasPhase Synthesis of Nanoparticles*. Weinheim: John Wiley & Sons, Ltd, 2017.
- [62] H. Haberland, M. Karrais, M. Mall, and Y. Thurner, "Thin films from energetic cluster impact: A feasibility study", *Journal of Vacuum Science & Technology A*, vol. 10, no. 5, pp. 3266–3271, 1992.
- [63] A. Vahl, J. Strobel, W. Reichstein, O. Polonskyi, T. Strunskus, L. Kienle, and F. Faupel, "Single target sputter deposition of alloy nanoparticles with adjustable composition via a gas aggregation cluster source", *Nanotechnology*, vol. 28, no. 17, p. 175703, 2017.
- [64] H. Hofmeister, "Fivefold Twinned Nanoparticles", in *Encyclopedia of Nanoscience and Nanotechnology*, H. S. Nalwa, Ed., vol. X, 2003, pp. 1–22.
- [65] B. Haberl, "Structural Characterization of Amorphous Silicon", PhD thesis, Australian National University, 2010.
- [66] R. Ghosh Chaudhuri and S. Paria, "Core/Shell Nanoparticles: Classes, Properties, Synthesis Mechanisms, Characterization, and Applications", *Chemical Reviews*, vol. 112, no. 4, pp. 2373–2433, 2012.
- [67] L. M. Liz-Marzán, M. Giersig, and P. Mulvaney, "Synthesis of Nanosized Gold-Silica Core-Shell Particles", *Langmuir*, vol. 12, no. 18, pp. 4329–4335, 1996.
- [68] P. Solař, O. Polonskyi, A. Olbricht, A. Hinz, A. Shelemin, O. Kylián, A. Choukourov, F. Faupel, and H. Biederman, "Single-step generation of metal-plasma polymer multicore@shell nanoparticles from the gas phase", *Scientific Reports*, vol. 7, no. 1, p. 8514, 2017.
- [69] S. Jiang, Q. Chen, M. Tripathy, E. Luijten, K. S. Schweizer, and S. Granick, "Janus Particle Synthesis and Assembly", *Advanced Materials*, vol. 22, no. 10, pp. 1060–1071, 2010.

- [70] A. Walther and A. H. E. Müller, "Janus particles", *Soft Matter*, vol. 4, no. 4, pp. 663–668, 2008.
- [71] S. Link, Z. L. Wang, and M. A. El-Sayed, "Alloy Formation of Gold-Silver Nanoparticles and the Dependence of the Plasmon Absorption on Their Composition", *The Journal of Physical Chemistry B*, vol. 103, no. 18, pp. 3529–3533, 1999.
- [72] R. Ferrando, J. Jellinek, and R. L. Johnston, "Nanoalloys: From Theory to Applications of Alloy Clusters and Nanoparticles", *Chemical Reviews*, vol. 108, no. 3, pp. 845–910, 2008.
- [73] P.-C. Chen, X. Liu, J. L. Hedrick, Z. Xie, S. Wang, Q.-Y. Lin, M. C. Hersam, V. P. Dravid, and C. A. Mirkin, "Polyelemental nanoparticle libraries", *Science*, vol. 352, no. 6293, pp. 1565–1569, 2016.
- [74] G. Guisbiers, R. Mendoza-Cruz, L. Bazán-Díaz, J. J. Velázquez-Salazar, R. Mendoza-Perez, J. A. Robledo-Torres, J.-L. Rodríguez-Lopez, J. M. Montejano-Carrizales, R. L. Whetten, and M. José-Yacamán, "Electrum, the Gold-Silver Alloy, from the Bulk Scale to the Nanoscale: Synthesis, Properties, and Segregation Rules", *ACS Nano*, vol. 10, no. 1, pp. 188–198, 2016.
- [75] P. A. Dowben, A. H. Miller, and R. W. Vook, "Surface segregation from gold alloys", *Gold Bulletin*, vol. 20, no. 3, pp. 54–65, 1987.
- [76] W. O. Saxton, W. Baumeister, and M. Hahn, "Three-dimensional reconstruction of imperfect two-dimensional crystals", *Ultramicroscopy*, vol. 13, no. 1, pp. 57–70, 1984.
- [77] J. V. Diloranzo, "Vapor growth of epitaxial GaAs: A summary of parameters which influence the purity and morphology of epitaxial layers", *Journal of Crystal Growth*, vol. 17, pp. 189–206, 1972.
- [78] M. Mecklenburg, A. Schuchardt, Y. K. Mishra, S. Kaps, R. Adelung, A. Lotnyk, L. Kienle, and K. Schulte, "Aerographite: Ultra Lightweight, Flexible Nanowall, Carbon Microtube Material with Outstanding Mechanical Performance", *Advanced Materials*, vol. 24, no. 26, pp. 3486–3490, 2012.
- [79] I. Plesco, J. Strobel, F. Schütt, C. Himcinschi, N. B. Sedrine, T. Monteiro, M. R. Correia, L. Gorceac, B. Cinic, V. Ursaki, J. Marx, B. Fiedler, Y. K. Mishra, L. Kienle, R. Adelung, and I. Tiginyanu, "Hierarchical Aerographite 3d flexible networks hybridized by InP micro/nanostructures for strain sensor applications", *Scientific Reports*, vol. 8, no. 1, p. 13 880, 2018.
- [80] M. Mattila, T. Hakkarainen, M. Mulot, and H. Lipsanen, "Crystal-structure-dependent photoluminescence from InP nanowires", *Nanotechnology*, vol. 17, no. 6, p. 1580, 2006.
- [81] R. E. Algra, M. A. Verheijen, M. T. Borgström, L.-F. Feiner, G. Immink, W. J. P. van Enckevort, E. Vlieg, and E. P. A. M. Bakkers, "Twinning superlattices in indium phosphide nanowires", *Nature*, vol. 456, no. 7220, pp. 369–372, 2008.

- [82] A. Krost, F. Heinrichsdorff, D. Bimberg, and H. Cerva, "InP on Si(111): Accommodation of lattice mismatch and structural properties", *Applied Physics Letters*, vol. 64, no. 6, p. 769, 1998.
- [83] R. L. Woo, R. Xiao, Y. Kobayashi, L. Gao, N. Goel, M. K. Hudait, T. E. Mallouk, and R. F. Hicks, "Effect of Twinning on the Photoluminescence and Photoelectrochemical Properties of Indium Phosphide Nanowires Grown on Silicon (111)", *Nano Letters*, vol. 8, no. 12, pp. 4664–4669, 2008.
- [84] G. Shen, Y. Bando, B. Liu, C. Tang, and D. Golberg, "Unconventional Zigzag Indium Phosphide Single-Crystalline and Twinned Nanowires", *The Journal of Physical Chemistry B*, vol. 110, no. 41, pp. 20 129–20 132, 2006.
- [85] K. Ikejiri, Y. Kitauchi, K. Tomioka, J. Motohisa, and T. Fukui, "Zinc Blende and Wurtzite Crystal Phase Mixing and Transition in Indium Phosphide Nanowires", *Nano Letters*, vol. 11, no. 10, pp. 4314–4318, 2011.
- [86] R. S. Wagner and W. C. Ellis, "Vapor-Liquid-Solid Mechanism of Single Crystal Growth", *Applied Physics Letters*, vol. 4, no. 5, p. 89, 1964.
- [87] C. M. Almeida, R. Prioli, and F. Ponce, "Effect of native oxide mechanical deformation on InP nanoindentation", *Journal of Applied Physics*, vol. 104, no. 11, p. 113 509, 2008.
- [88] G. Chen, S. B. Visbeck, D. C. Law, and R. F. Hicks, "Structure-sensitive oxidation of the indium phosphide (001) surface", *Journal of Applied Physics*, vol. 91, no. 11, p. 9362, 2002.
- [89] E. Comini, A. Cristalli, G. Faglia, and G. Sberveglieri, "Light enhanced gas sensing properties of indium oxide and tin dioxide sensors", *Sensors and Actuators B: Chemical*, vol. 65, no. 1, pp. 260–263, 2000.
- [90] D. Selvakumar, P. Rajeshkumar, N. Dharmaraj, and N. S. Kumar, "NO₂ Gas sensing properties of hydrothermally prepared platinum doped indium oxide nanoparticles", *Materials Today: Proceedings, Recent Advances In Nano Science And Technology 2015*, vol. 3, no. 6, pp. 1725–1729, 2016.
- [91] C. Xiangfeng, W. Caihong, J. Dongli, and Z. Chenmou, "Ethanol sensor based on indium oxide nanowires prepared by carbothermal reduction reaction", *Chemical Physics Letters*, vol. 399, no. 4, pp. 461–464, 2004.
- [92] J. F. Wager and C. W. Wilmsen, "Thermal oxidation of InP", *Journal of Applied Physics*, vol. 51, no. 1, pp. 812–814, 1980.
- [93] I. Plesco, M. Dragoman, J. Strobel, L. Ghimpu, F. Schütt, A. Dinescu, V. Ursaki, L. Kienle, R. Adelung, and I. Tiginyanu, "Flexible pressure sensor based on graphene aerogel microstructures functionalized with CdS nanocrystalline thin film", *Superlattices and Microstructures*, vol. 117, pp. 418–422, 2018.

- [94] R. S. Vemuri, S. K. Gullapalli, D. Zubia, J. C. McClure, and C. V. Ramana, "Structural and chemical properties of highly oriented cadmium sulfide (CdS) cauliflower films", *Chemical Physics Letters*, vol. 495, no. 4, pp. 232–235, 2010.
- [95] H. Khallaf, I. O. Oladeji, G. Chai, and L. Chow, "Characterization of CdS thin films grown by chemical bath deposition using four different cadmium sources", *Thin Solid Films*, vol. 516, no. 21, pp. 7306–7312, 2008.
- [96] O. Lupan, V. Postica, M. Mecklenburg, K. Schulte, Y. K. Mishra, B. Fiedler, and R. Adelung, "Low powered, tunable and ultra-light aerographite sensor for climate relevant gas monitoring", *Journal of Materials Chemistry A*, vol. 4, no. 42, pp. 16 723–16 730, 2016.
- [97] J. Strobel, L. Ghimpu, V. Postica, O. Lupan, M. Zapf, S. Schönherr, R. Röder, C. Ronning, F. Schütt, Y. K. Mishra, I. Tiginyanu, R. Adelung, J. Marx, B. Fiedler, and L. Kienle, "Improving gas sensing by CdTe decoration of individual aerographite microtubes", *Nanotechnology*, 2018.
- [98] P. B. Barna and M. Adamik, "Fundamental structure forming phenomena of polycrystalline films and the structure zone models", *Thin Solid Films*, vol. 317, no. 1, pp. 27–33, 1998.
- [99] G. Korotcenkov, "The role of morphology and crystallographic structure of metal oxides in response of conductometric-type gas sensors", *Materials Science and Engineering: R: Reports*, vol. 61, no. 1, pp. 1–39, 2008.
- [100] W.-T. Moon, K.-S. Lee, Y.-K. Jun, H.-S. Kim, and S.-H. Hong, "Orientation dependence of gas sensing properties of TiO₂ films", *Sensors and Actuators B: Chemical*, vol. 115, no. 1, pp. 123–127, 2006.
- [101] O. Gronenberg, "Fabrication and Application of Dedicated TEM Compatible Sample Grids Suitable for Ex Situ Electrical Probing", Master's thesis, University of Kiel, Kiel, 2018.

Declaration of Authorship

Ich erkläre hiermit, dass die Abhandlung, abgesehen von der Beratung durch die Betreuerin oder den Betreuer, nach Inhalt und Form meine eigene Arbeit ist.

Die Arbeit wurde weder ganz noch in Teilen an anderer Stelle im Rahmen eines Prüfungsverfahrens vorgelegt, veröffentlicht oder zur Veröffentlichung eingereicht.

Die Arbeit ist unter Einhaltung der Regeln guter wissenschaftlicher Praxis der Deutschen Forschungsgemeinschaft entstanden.

Mir wurde kein akademischer Grad entzogen.

Ort, Datum

Unterschrift: Julian STROBEL